AD-A033 033 AERONAUTICAL RESEARCH ASSOCIATES OF PRINCETON INC N J F/G 20/11
THE SENSITIVITY OF IMPACT RESPONSE TO THE MECHANICAL BEHAVIOR O--ETC(U)
JAN 76 T B MCDONOUGH, R M CONTILIANO F44620-74-C-0045

UNCLASSIFIED ARAP-266 AFOSR-TR-76-1083 NL

| OF |
AD
A033033

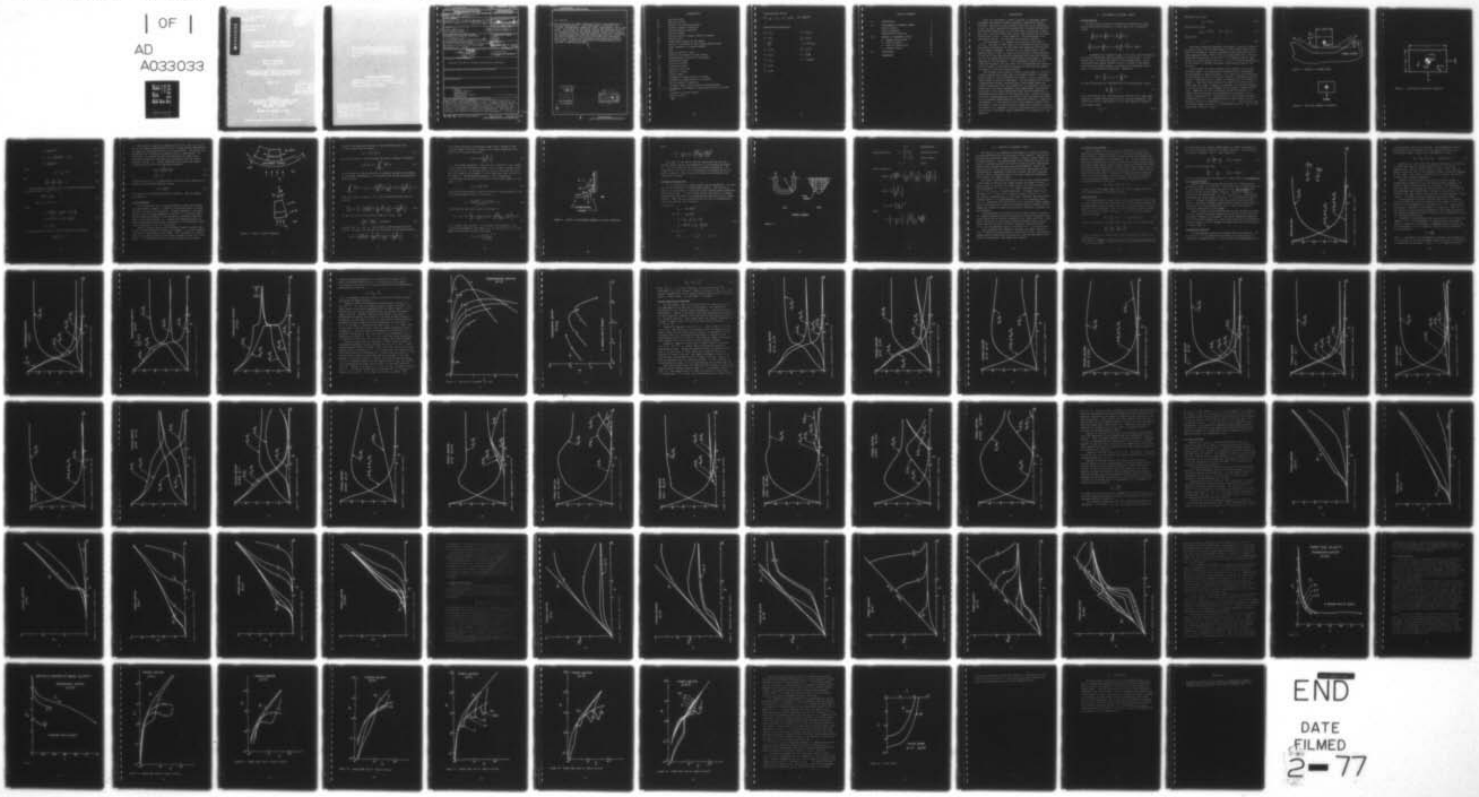

END
DATE FILMED
2-77

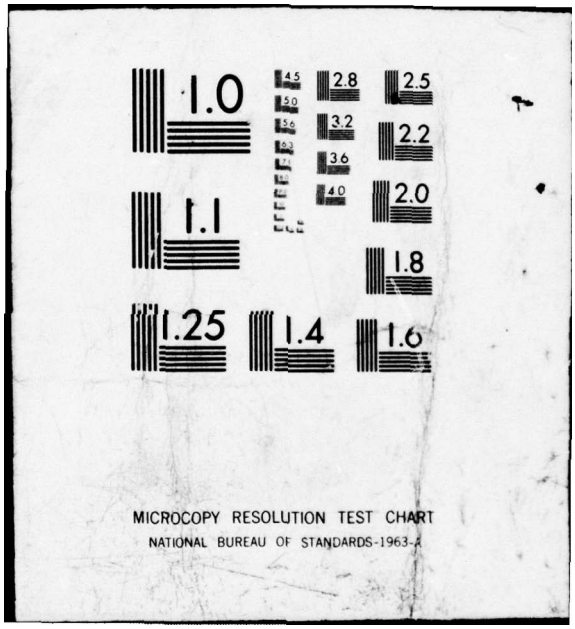
1.0
1.1
1.25
1.4
1.6
1.8
2.0
2.2
2.5
2.8
3.2
3.6
4.0
4.5
5.0
5.6
MICROCOPY RESOLUTION TEST CHART
NATIONAL BUREAU OF STANDARDS-1963-A

[illegible]

A.R.A.P. REPORT NO. [illegible]

[illegible] REPORT

THE SENSITIVITY OF IMPACT RESPONSE TO THE MECHANICAL BEHAVIOR OF THE PENETRATOR

THOMAS B. McDONOUGH
[illegible]

AERONAUTICAL RESEARCH ASSOCIATES OF PRINCETON, INC.
50 WASHINGTON ROAD, PRINCETON, NEW JERSEY 08540

JANUARY 1976

PREPARED FOR
AIR FORCE OFFICE OF SCIENTIFIC RESEARCH (AFSC)
BUILDING 410, BOLLING AIR FORCE BASE
WASHINGTON, DC 20332

CONTRACT NO. F44620-74-C-0046

UNCLASSIFIED

SECURITY CLASSIFICATION OF THIS PAGE (When Data Entered)

(14) ARAP-266

REPORT DOCUMENTATION PAGE	READ INSTRUCTIONS BEFORE COMPLETING FORM
(18) 1. REPORT NUMBER (19) AFOSR - TR - 76 - 1083	2. GOVT ACCESSION NO. / 3. RECIPIENT'S CATALOG NUMBER
(6) 4. TITLE (and Subtitle) THE SENSITIVITY OF IMPACT RESPONSE TO THE MECHANICAL BEHAVIOR OF THE PENETRATOR	(9) 5. TYPE OF REPORT & PERIOD COVERED Interim rept. 1 Jul 74 – 31 Dec 75, / 6. PERFORMING ORG. REPORT NUMBER A.R.A.P. Report No. 266
(10) 7. AUTHOR(s) Thomas B. McDonough, Ross M. Contiliano	(15) 8. CONTRACT OR GRANT NUMBER(s) F44620-74-C-0045
9. PERFORMING ORGANIZATION NAME AND ADDRESS Aeronautical Research Associates of Princeton, Inc. 50 Washington Road, Princeton, NJ 08540	10. PROGRAM ELEMENT, PROJECT, TASK AREA & WORK UNIT NUMBERS 681307 9782-05 61102F
11. CONTROLLING OFFICE NAME AND ADDRESS Air Force Office of Scientific Research/NA Building 410, Bolling Air Force Base Washington, DC 20332	(11) 12. REPORT DATE JAN 76 / 13. NUMBER OF PAGES 76 (12) 80p.
14. MONITORING AGENCY NAME & ADDRESS (if different from Controlling Office) (16) 9782 (17) 05	15. SECURITY CLASS. (of this report) Unclassified / 15a. DECLASSIFICATION/DOWNGRADING SCHEDULE

16. DISTRIBUTION STATEMENT (of this Report)

Approved for public release; distribution unlimited

17. DISTRIBUTION STATEMENT (of the abstract entered in Block 20, if different from Report)

18. SUPPLEMENTARY NOTES

19. KEY WORDS (Continue on reverse side if necessary and identify by block number)

Impact
Integral Theory
Hydrodynamic
Rigid-Plastic Solid
Penetration

* is under development.

20. ABSTRACT (Continue on reverse side if necessary and identify by block number)

An integral theory of impact is under development at A.R.A.P. It is a simple theory, which makes it easy to focus attention on the various physical phenomena which occur, and it is simple enough so that the performance of parametric studies is economical. The theory has progressed in steps, starting from the simplest model possible and gradually adding more complexities. This report presents the results of one step in the development: a study of → next page

DD FORM 1 JAN 73 1473 EDITION OF 1 NOV 65 IS OBSOLETE

UNCLASSIFIED 008 400

SECURITY CLASSIFICATION OF THIS PAGE (When Data Entered)

20. (cont'd)

the sensitivity of impact characteristics to the properties of the impacting particle. Four ideal models of behavior are treated: hydrodynamic, Newtonian fluid, rigid-plastic solid, and rigid. The effects on the impact process are presented in terms of the partitioning of the energy between particle and target, the deformation of the impacting particle, depth into the target the particle penetrates, and the target mass lost as a result of the cavity formation. The predicted trends with increasing impact velocity show some interesting and unforeseen results; for example, penetration depth does not increase always with increase of particle strength.

NOMENCLATURE

b	particle width
C_D	drag coefficient
$\dot{e}_{ij}$	deviator of stretching tensor
E	internal energy of particle
K	kinetic energy of particle
ℓ	particle height
ℓ_o	initial particle height, width, or length
m_p	particle mass
m_t	target mass removed by the impact
R	radius of curvature of the flowing shocked layer
s	axial component of stress deviator
t	time
$V_\perp$	speed of particle front
V_{cm}	speed of the particle's mass center
V^*	characteristic velocity of the target
y	penetration depth
$\dot{z}_i$	particle velocity
$\dot{\varepsilon}_{ij}$	stretching tensor
ρ_p	density of particle
ρ_t	density of target
σ_{ij}	stress tensor
σ_1	strength of target normal to surface
σ_2	strength of target parallel to surface
σ_y	yield strength of particle
ϕ	incidence angle along surface of shocked layer
ξ, η, ζ	rectangular coordinates originating at particle's mass center
μ	viscosity of liquid droplet
γ	surface tension
$(\dot{})$	$= \frac{d}{dt}(\ )$

Characteristic Values

$$V^* \ , \ \rho_p \ , \ \ell_o \ , \ \sigma_1 = \rho_t V^{*2} \ , \ K^* = \frac{m_p}{2} V^{*2}$$

Dimensionless Parameters

$$\bar{b} \equiv b/\ell_o \qquad \bar{s} \equiv s_{yy}/\sigma_1$$

$$\bar{\ell} \equiv \ell/\ell_o \qquad \bar{\sigma}_y \equiv \sigma_y/\sigma_1$$

$$\tau \equiv \frac{V^*}{\ell_o} t \qquad \bar{\mu} \equiv (V^*/\ell_o\sigma_1)\mu$$

$$\bar{\rho} \equiv \rho_t/\rho_p \qquad \bar{V}_\perp \equiv V_\perp/V^*$$

$$\bar{\sigma} \equiv \sigma_2/\sigma_1 \qquad \bar{\xi} \equiv \frac{1}{2} \frac{\dot{\ell}}{V^*}$$

$$\bar{y} \equiv y/\ell_o \qquad \bar{\gamma} \equiv (\ell_o^2/K^*)\gamma$$

$$\bar{E} \equiv E/K^*$$

$$\bar{K} \equiv K/K^*$$

TABLE OF CONTENTS

I. INTRODUCTION

There is considerable current interest in high-speed impact phenomena, and numerous studies presently underway are being reported. Generally, these studies follow one of two approaches: on the one hand, experimental programs are conducted and data are extrapolated empirically; on the other hand, theoretical studies have led to the development and use of very detailed multi-element computational codes. A third approach - the development of an approximate theory - has received only minimal attention.

The development of a simple theory has been initiated at A.R.A.P. The goal of this theory is to identify the way in which the physical properties of the target and penetrator are related to the impact phenomena. Because it is a simple theory, this approach makes it easy to focus one's attention on the importance of any one of the many physical phenomena that enter the problem, such as the energy partition between particle and target. Numerical computations are economical. Thus, parametric studies can be conducted reasonably and are useful for interpreting test observations in terms of the physical processes at work and for guiding the design of effective armor systems.

The integral theory bears a similar relationship to the multi-element computational codes that the integral theory of boundary layers bears to finite difference solutions. It is a simplified theory based on heuristic procedure. The development has followed a step-by-step process, starting from a very simple form, and further complexities have been added only as required to bring the predictions into better agreement with experimental observations. One aspect of the impact phenomenon which has been addressed is characterizing the state of the impacting body. Previous studies have shown surprisingly good correlation with available test data[1] for two extreme representations of penetrator behavior - rigid and hydrodynamic. In the present study, other models of behavior are introduced which include material strength and viscosity. Finally, the results of a parametric study are presented which illustrate the sensitivity of pertinent impact parameters to the behavior of the impactor.

II. DEVELOPMENT OF INTEGRAL THEORY

Particle Motion

We start with the global conservation equations for linear momentum and kinetic energy of a fixed body, i.e., a material volume

$$\int_S \sigma_{ij} n_j \, da + \int_V \rho f_i \, dv = \frac{d}{dt} \int_V \rho \dot{z}_i \, dv \tag{1}$$

$$\int_S \dot{z}_i \sigma_{ij} n_j \, da + \int_V \rho \dot{z}_i f_i \, dv = \frac{d}{dt} \int_V \rho \, \frac{\dot{z}_i \dot{z}_i}{2} \, dv + \frac{d}{dt} E \tag{2}$$

E represents the internal energy of the body, and its prescription limits the energy transfer permitted in the theory. In the present case, we assume the impact occurs adiabatically, and we characterize the energy transfer totally in terms of the stress power and free surface energy. The latter is represented only in terms of the equilibrium properties. Therefore,

$$\frac{d}{dt} E = \int_V \sigma_{ij} \dot{z}_{i,j} \, dv + \int_{\mathcal{S}} \gamma \dot{\overline{da}} \tag{3}$$

The above equations are complemented by the conservation of mass

$$\frac{d}{dt} \int_V \rho \, dv = 0 \tag{4}$$

and a constitutive law. Because elastic strains are so very small compared to strain associated with flow, they are neglected. The constitutive law is represented by four ideal models of behavior:

Hydrodynamic model

$$s_{ij} = 0 \tag{5a}$$

Newtonian fluid model

$$s_{ij} = 2\mu \dot{e}_{ij} \tag{5b}$$

Rigid plastic model

$$s_{ij}s_{ij} = \frac{4}{3}\sigma_y^2 \qquad \text{for} \quad \dot{e}_{ij} \neq 0 \tag{5c}$$

Rigid model

$$\dot{\varepsilon}_{ij} = 0 \tag{5d}$$

The above equations represent the physics of particle behavior in general form. Further development of the present theory introduces no new physics. Rather, assumptions are introduced into the above equations which reduce them to an approximate set of ordinary differential equations, in the spirit of integral boundary layer theory and finite element analysis. In all of these approximations, we are careful to satisfy the global conservations laws for the particle.

Now consider the normal impact of the particle onto a semi-infinite target. We characterize the particle as a rectangular parallelepiped of square planform. For simplicity, the deformation is constrained so that the particle remains a rectangular parallelepiped. Penetration into a target is schematically illustrated by Figure 1. The only force acting on the particle is the contact force with the target. Figure 2 illustrates a "free body" diagram of the particle with the resistive force acting to impede penetration. Regarding the flow of material within the particle, we assume that the velocity varies linearly with position, and we neglect compressibility. The situation is illustrated by Figure 3. Coordinates ξ , η , ζ are measured from the mass center, and the material velocity is denoted by V_x , V_y , V_z . The velocity field is written simply in terms of the front face velocity ($V_\perp$) and the mass center velocity (V_{cm}):

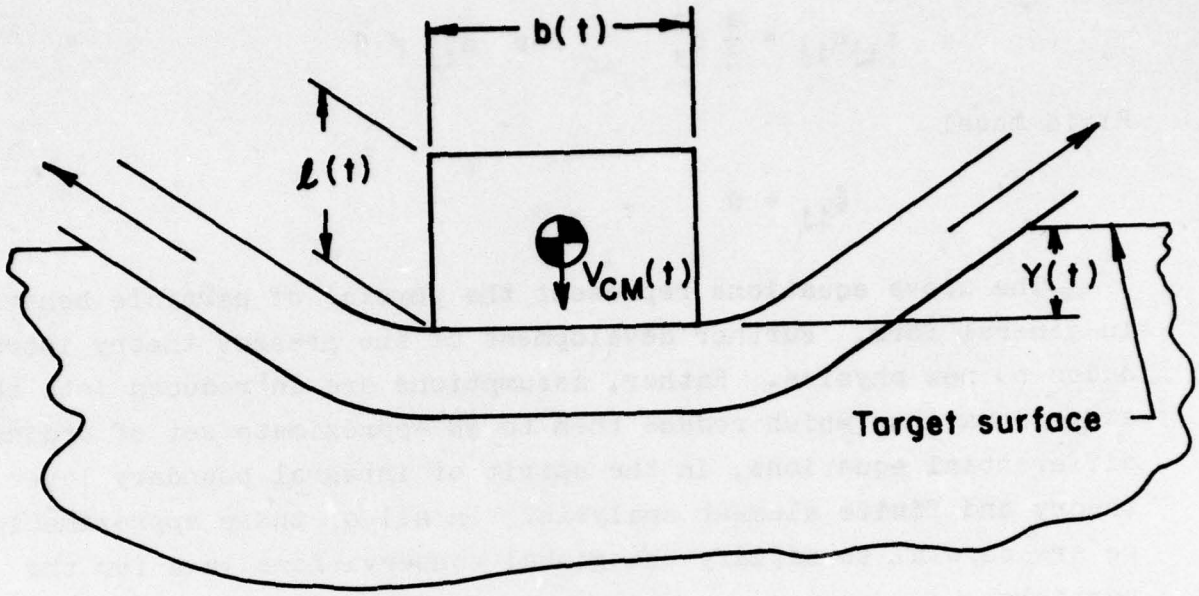

Figure 1. Schematic of impact model

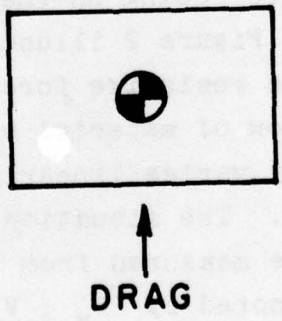

Figure 2. Free body diagram of particle

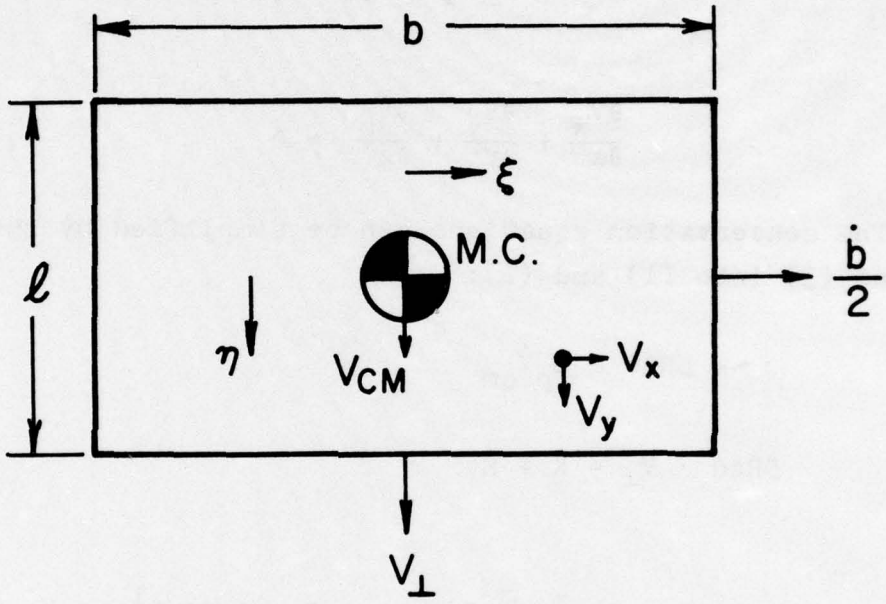

Figure 3. Description of particle kinematics

$$V_x = \left(\frac{\xi}{b/2}\right)\frac{1}{2}\,\dot{b} \tag{6a}$$

$$V_y = V_{cm} + \left(\frac{\eta}{\ell/2}\right)\left(V_\perp - V_{cm}\right) \tag{6b}$$

$$V_z = \left(\frac{\zeta}{b/2}\right)\frac{1}{2}\,\dot{b} \tag{6c}$$

where

$$V_\perp - V_{cm} = \frac{1}{2}\,\dot{\ell} \tag{7}$$

and

$$\frac{\partial V_x}{\partial x} + \frac{\partial V_y}{\partial y} + \frac{\partial V_z}{\partial z} = 0 \tag{8}$$

The conservation equations can be simplified by substituting (6) and (3) into (1) and (2):

$$\begin{aligned} -\,\mathrm{DRAG} &= m_p \dot{V}_{cm} \\ \mathrm{DRAG}\cdot V_\perp &= \dot{K} + \dot{E} \end{aligned} \tag{9}$$

where

$$K = \frac{m_p}{2}\left[V_{cm}^2 + \frac{1}{6}\left(\dot{b}^2 + \frac{1}{2}\,\dot{\ell}^2\right)\right]$$

$$\dot{E} = \frac{3}{2}\,b^2 s\dot{\ell} + 2\gamma\left(1 - \frac{b}{\ell}\right)b\dot{\ell} \tag{10}$$

$$m_p \equiv \rho_p b^2 \ell$$

and substituting (6) and (7) into (8) gives the following:

$$2\,\frac{\dot{b}}{b} + \frac{\dot{\ell}}{\ell} = 0 \tag{11}$$

The system of equations composed of (7), (9), (10), (11), and one of the models represented by (5) is a closed system representing the equations governing the motion of the particle. The drag force represents the resistance the target offers to penetration. As previously, we assume the particle penetrates as long as the Newtonian pressure at the front face is greater than the target strength (called σ_1). While penetration continues, the drag is assumed proportional to the Newtonian pressure:

$$\text{DRAG} = \left(\frac{C_D}{2}\right) \rho_t V_\perp^2 b^2 \tag{12}$$

if

$$\rho_t V_\perp^2 > \sigma_1 \tag{13}$$

Consistent with (13), a characteristic velocity can be defined for a target, below which penetration ceases.

$$V^* \equiv \sqrt{\sigma_1/\rho_t} \tag{14}$$

The equations for penetration are now complete. Next we address mass removal.

Cavity Formation

We visualize the flow of target material around the particle as illustrated by Figure 4. There is a disturbed layer of target material in front of the particle. Fixing ourselves to the front face, we see the target approach at velocity $V_\perp$ (see the figure), and we assume the material flows laterally, leaving the particle edge at the same velocity $V_\perp$. Neglecting compressibility, the mass flowing into balances that flowing out of the disturbed region if the thickness is $b/4$ as illustrated.

The two layers (particle and disturbed target) possess significant lateral momentum in their flow outward. It is this momentum that cuts a wide cavity in the target. The flow does not continue flat; it is turned upward by the target pressure acting on it from below. At a particular section, we can estimate the curvature.

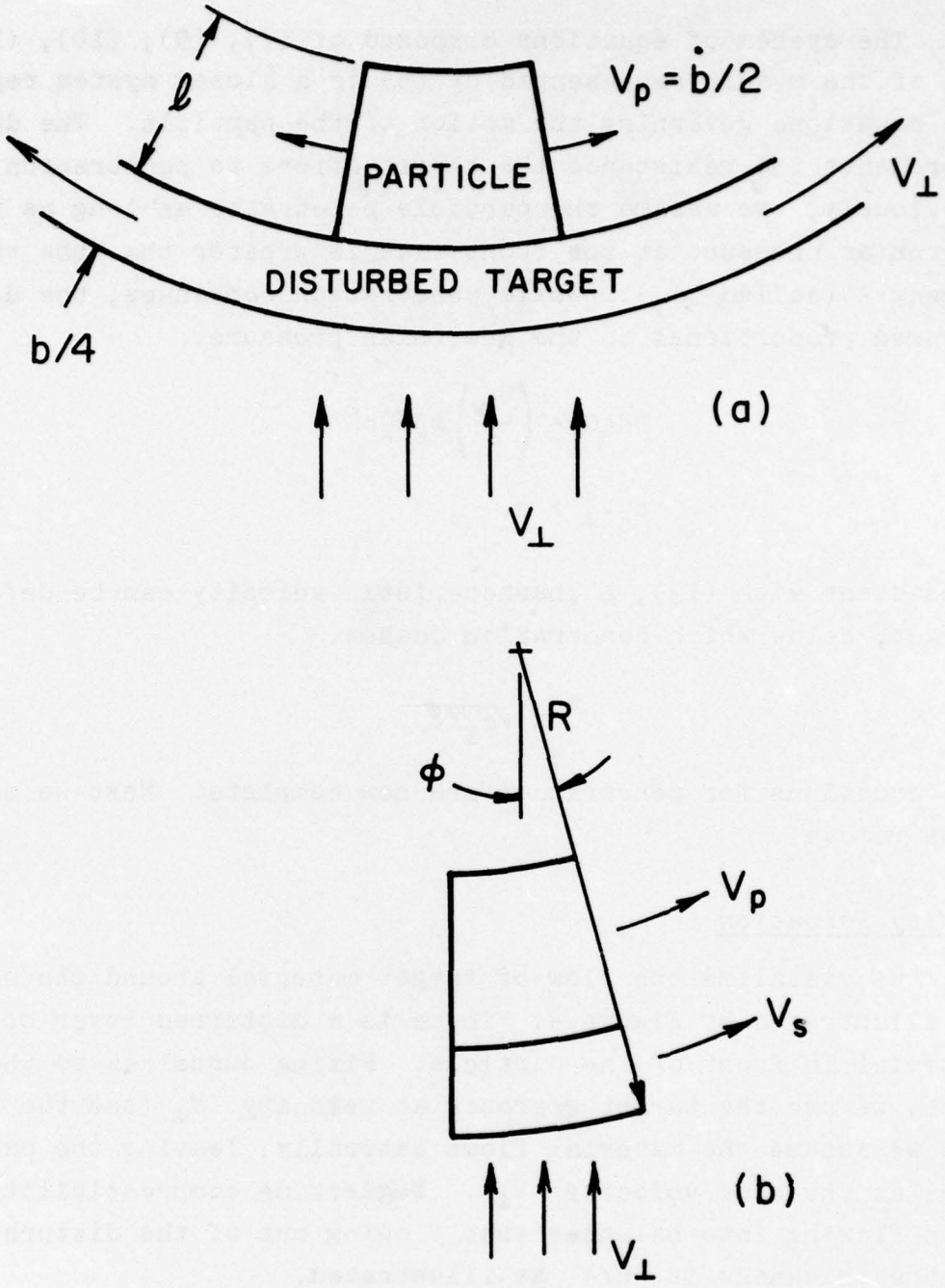

Figure 4. Model of cavity formation

Consider the momentum delivered to the disturbed layer; the pressure equals the net moment.

$$\Delta p = \rho_t V_\perp^2 \cos^2 \phi \tag{15}$$

But this pressure is what produces the rate of change of momentum:

$$\rho_t V_\perp^2 \cos^2 \phi = \int_{R-\frac{b}{4}-\ell}^{R} \frac{\rho V^2}{z}\, dz \tag{16}$$

If we assume the lateral velocity is constant through the thickness of each layer independently, the integral has the following approximate solution:

$$\int_{R-\frac{b}{4}-\ell}^{R} \frac{\rho V^2}{z}\, dz = \rho_p (V_p)^2 \ell n \left(\frac{\frac{4R}{b} - 1}{\frac{4R}{b} - 1 - \frac{4\ell}{b}} \right) + \rho_t V_t^2 \ell n \left(\frac{\frac{4R}{b}}{\frac{4R}{b} - 1} \right) \tag{17}$$

When this result is used in (16), the following solution can be derived:

$$\left[\frac{V_\perp}{V_t} \cos \phi \right]^2 = \left(\frac{\rho_p}{\rho_t} \right) \left(\frac{V_p}{V_t} \right)^2 \ell n \left(\frac{\frac{4R}{b} - 1}{\frac{4R}{b} - 1 - \frac{4\ell}{b}} \right) + \ell n \left(\frac{\frac{4R}{b}}{\frac{4R}{b} - 1} \right) \tag{18}$$

We use the value at the particle edge for $V_\perp/V_t$, and

$$\left(\frac{V_p}{V_t} \right)^2 = \left(\frac{\dot{b}/2}{V_\perp} \right) \quad \text{everywhere} \tag{19}$$

because both V_p and V_t vary linearly with distance from the center. Finally, the equation for the radius of curvature becomes

$$\cos^2 \phi = \left(\frac{\rho_p}{\rho_t} \right) \left(\frac{\dot{b}/2}{V_\perp} \right) \ell n \left(\frac{\frac{4R}{b} - 1}{\frac{4R}{b} - 1 - \frac{4\ell}{b}} \right) + \ell n \left(\frac{\frac{4R}{b}}{\frac{4R}{b} - 1} \right) \tag{20}$$

To consider the flow of disturbed target layer outside of the particle edge, one needs to neglect the lateral momentum of the particle in the above equations.

$$\cos^2\phi = \ell n \left(\frac{\frac{4R}{b}}{\frac{4R}{b} - 1} \right) \tag{21}$$

The lateral momentum of the flow will continue to cut a wider cavity until the transverse strength of the target is great enough to stop the flow. To analyze this situation, we assume the flow will be turned up at an angle θ by a rigid wall and illustrate it by Figure 5. The Newtonian pressure in the flowing layer (produced by the momentum flux from the undisturbed region) at the angle θ is

$$P_o = \rho_t V_\perp^2 \cos^2\theta \tag{22}$$

To turn the flow vertical requires a pressure increase equal to the horizontal momentum flux of both layers:

$$\Delta P = \frac{\ell \rho_p (\dot{b}/2)^2 + (b/4)\rho_t V_\perp^2}{(\ell + b/4)} \cos^2\theta \tag{23}$$

Therefore, the wall must sustain a pressure of

$$P_1 = P_o + \Delta P = \left[\left(1 + \frac{1}{\frac{4\ell}{b} + 1} \right) \rho_t V_\perp^2 + \frac{\left(\frac{4\ell}{b}\right)}{\left(1 + \frac{4\ell}{b}\right)} \rho_p \left(\frac{\dot{b}}{2}\right)^2 \right] \cos^2\theta \tag{24}$$

or it cannot turn the flow. If we equate this pressure to the transverse strength of the target (σ_2), we can solve for θ_1, the angle at which the flow will be turned

$$\theta_1 = \cos^{-1} \left[\frac{\sigma_2}{f \rho_t V_\perp^2} \right]^{1/2} \tag{25}$$

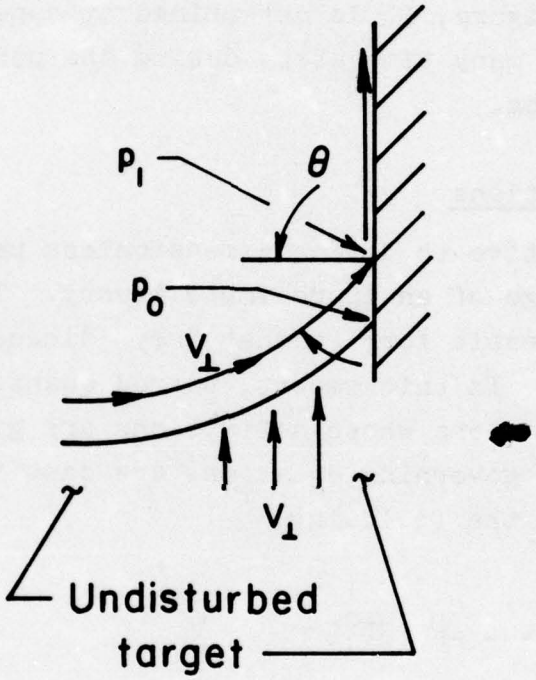

Figure 5. Effect of transverse strength on cavity formation

where

$$f = \left(1 + \frac{1}{\frac{4\ell}{b} + 1}\right) + \frac{\left(\frac{4\ell}{b}\right)}{\left(1 + \frac{4\ell}{b}\right)} \frac{\rho_p\left(\frac{1}{2}\dot{b}\right)^2}{\rho_t V_\perp^2}$$

The shape of the cavity that is created by the flow at a typical instant during the penetration is illustrated by Figure 6a. The final shape of the cavity is shown by Figure 6b. As suggested by the figure, it is determined by superposing all the shapes computed at many time steps during the penetration and using their envelope.

Dimensionless Equations

It is informative to define dimensionless parameters. In fact, that is an advantage of an approximate theory. The problem is reduced to a manageable form so that "key" dimensionless parameters can be identified. In this report, barred quantities will denote dimensionless parameters whose definitions are given in the nomenclature. When the governing equations are cast in dimensionless terms, they become the following:

Penetration

$$\begin{aligned}
&\bar{V}'_{cm} = -\frac{C_D}{2}\,\bar{\rho}\bar{V}_\perp^2\bar{b}^2 \\
&\bar{K}' + \bar{E}' = -C_D\bar{\rho}\,\bar{V}_\perp^3\bar{b}^2 \\
&\bar{K} = \bar{V}_{cm}^2 + \frac{1}{6}\left(\bar{\eta}^2 + 2\bar{\xi}^2\right) \\
&\bar{E}' = 6\bar{\rho}\bar{b}^2\bar{s}\bar{\xi} + 4\left(1 - \frac{\bar{b}}{\bar{\ell}}\right)\bar{b}\bar{\gamma}\bar{\xi} \\
&\bar{V}_\perp - \bar{V}_{cm} = \bar{\xi} \\
&\bar{b}^2\bar{\ell} = 1 \quad ; \quad \bar{\xi} \equiv \frac{1}{2}\bar{\ell}' \quad ; \quad \bar{\eta} \equiv \bar{b}'
\end{aligned} \tag{26}$$

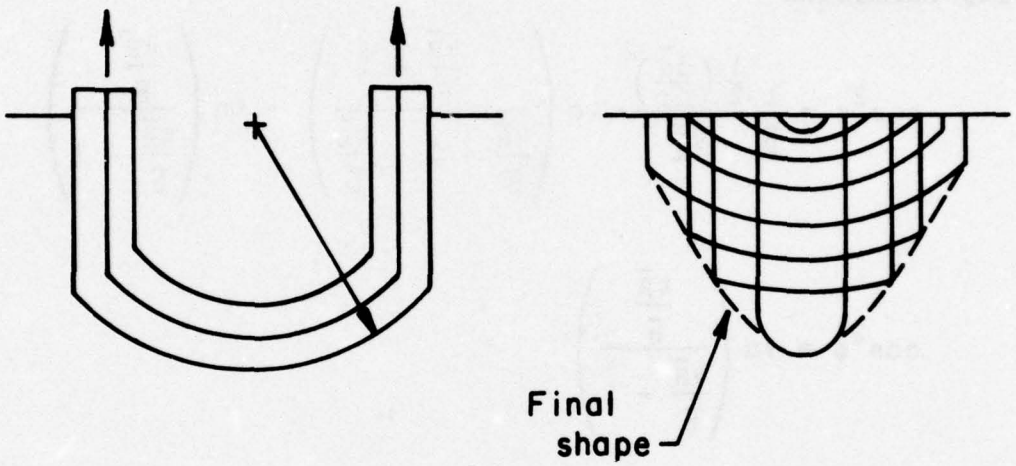

Figure 6.

Constitutive Law

$$\bar{s} = \begin{cases} 0 & \text{Hydrodynamic} \\ 4\bar{\mu}\,\dfrac{\bar{\xi}}{\bar{\ell}} & \text{Newtonian Fluid} \\ -\dfrac{2}{3}\,\bar{\sigma}_y & \text{Rigid Plastic} \end{cases}$$

$$\bar{\xi} = 0 \qquad \text{Rigid}$$

Cavity Formation

$$\cos^2\phi = \frac{1}{\bar{\rho}}\,\frac{\frac{1}{2}\left(\frac{d\bar{b}}{d\tau}\right)^2}{V_\perp^2}\,\ell n\left(\frac{\frac{4\bar{R}}{\bar{b}} - 1}{\frac{4\bar{R}}{\bar{b}} - 1 - \frac{4\bar{\ell}}{\bar{b}}}\right) + \ell n\left(\frac{\frac{4\bar{R}}{\bar{b}}}{\frac{4\bar{R}}{\bar{b}} - 1}\right)$$

$$\cos^2\phi = \ell n\left(\frac{\frac{4\bar{R}}{\bar{b}}}{\frac{4\bar{R}}{\bar{b}} - 1}\right) \tag{27}$$

$$\theta_1 = \cos^{-1}\left[\frac{\bar{\sigma}}{f\bar{V}_\perp^2}\right]^{1/2}$$

where

$$f = \left(1 + \frac{1}{\frac{4\bar{\ell}}{\bar{b}} + 1}\right) + \frac{\left(\frac{4\bar{\ell}}{\bar{b}}\right)}{\left(1 + \frac{4\bar{\ell}}{\bar{b}}\right)}\,\frac{\left(\frac{1}{2}\,\frac{d\bar{b}}{d\tau}\right)^2}{\bar{\rho}\bar{V}_\perp^2}$$

III. RESULTS OF PARAMETRIC STUDY

The results of a parametric investigation of impact cratering by high-speed particles are presented in this chapter. The results describe one particular class of impacts, namely, normal impact of a single particle. An understanding of the impact process for this class is a prime requisite for the more usual but more complicated classes which include multiple and oblique impacts. Hence, the results which follow, aside from their obvious usefulness for data interpretation, parameter sensitivity studies, and test planning, will be used to illustrate many of the basic physical mechanisms which control the impact process.

The impact conditions which were used for this study encompass a wide range of particle and target density and impact velocity. Three values of the ratio of target density to particle density ($\bar{\rho}$) were considered: $\bar{\rho} = 0.1$ (i.e., a "heavy" particle), $\bar{\rho} = 1.0$, and $\bar{\rho} = 10.0$ (i.e., a "light" particle). For each value of $\bar{\rho}$, the value of $\bar{V}$ (the ratio of particle impact velocity to V^*, the velocity characteristic of the target strength) was varied from slightly above 1.0 to approximately 50. In the integral theory, $\bar{V} = 1.0$ represents the velocity ratio for incipient target damage; impact velocities below this value produce elastic response in the target but produce no penetration and are, therefore, excluded from this analysis.

Two mechanisms are included in the integral theory to account for energy dissipation within the particle, viscous dissipation for liquid particles and plastic dissipation for solid particles. Parametric variation of the internal energy dissipation was achieved using particle viscosity (or yield strength) values from zero (i.e., the hydrodynamic limit) to infinity (i.e., the rigid limit).

Many parameters are needed to describe the impact process; four of these are given detailed consideration below. They include energy partitioning within the particle, particle deformation and depth of penetration, and target mass removal.

A. Energy Partitioning

Prior to impact, the total energy contained in the system comprising the particle and target is the kinetic energy of the particle* ($\bar{K}_o$). During an impact, work is done on the target and energy is transferred at the expense of $\bar{K}$. In this study, four modes are accounted for: kinetic energy of the particle associated with mass center motion ($\bar{K}_{cg}$), kinetic energy of the particle associated with motion relative to the mass center ($\bar{K}_R$), energy that is dissipated by the resistance of the particle to flow ($\bar{E}$), and work done on the target ($\bar{E}_D$). Although the energy may be transferred from one mode to another, it must remain in the system somewhere. Its conservation requires that the energy components obey the following equation at any time:

$$\bar{K}_o = \bar{K}_{cg} + \bar{K}_R + \bar{E}_D + \bar{E} \tag{28}$$

A study of how the energy partitions for various impact cases is very enlightening for the impact process.

Rigid Particle

The rigid particle idealization is also approached in the limit by very strong solid particles and very viscous liquid particles for an appreciable range of impact velocity. By definition, the rigid particle does not deform. Hence it has no relative kinetic energy and dissipates no energy internally. For this case, the energy equation becomes

$$\bar{K}_o = \bar{K}_{cg} + \bar{E}_D \qquad \text{(rigid particle)} \tag{29}$$

Since the velocity is uniform within the particle, it follows that

$$\frac{\bar{K}}{\bar{K}_o} = \frac{\bar{K}_{cg}}{\bar{K}_o} = \frac{\bar{V}_{cg}^2}{\bar{V}_o^2} = \frac{\bar{V}_\perp^2}{\bar{V}_o^2} \tag{30}$$

i.e., the fraction of the initial kinetic energy which remains in

*The internal energy of both the particle and target is taken to be zero prior to impact. Internal energies are then measured relative to this ground state.

the particle at any instant during impact is simply the square of the ratio of particle velocity to impact velocity. In particular, at the end of impact, $\bar{V}_\perp = 1$ and, therefore,

$$\frac{\bar{K}}{K_o} = \frac{\bar{K}_{cg}}{\bar{K}_o} = \frac{1}{\bar{V}_o^2} \qquad \text{(end of impact)} \qquad (31)$$

Equation (28) requires that

$$\frac{\bar{E}_D}{\bar{K}_o} = 1 - \frac{1}{\bar{V}_o^2} \qquad \text{(end of impact)} \qquad (32)$$

Note that the energy partitioning for a rigid particle is independent of the density ratio.

Figure 7 shows the energy partitioning for a rigid particle according to Eqs. (31) and (32). This figure and all subsequent ones of this type show the energy partition at the end of impact as a function of the initial impact velocity. The end of impact is defined as the instant when $V_\perp = V^*$ (i.e., $\bar{V}_\perp = 1$). A method for estimating the characteristic velocity V^* is described in Reference 1. Although the particle still has axial velocity at this instant, the kinetic energy associated with further deceleration of the particle is stored elastically in the target and causes no additional penetration of the target.

Figure 7 shows a very rapid increase in the transfer of energy from that stored in elastic response to work done on the target as the impact velocity is increased. The latter component dominates for velocity ratios above 1.5. Note that nearly all of the particle kinetic energy is used to damage the target when the velocity ratio is larger than 10.

Hydrodynamic Particle

The hydrodynamic particle is another useful idealization. By definition, it is a particle which deforms but which offers no resistance to shearing flow. It is a fairly good approximation for

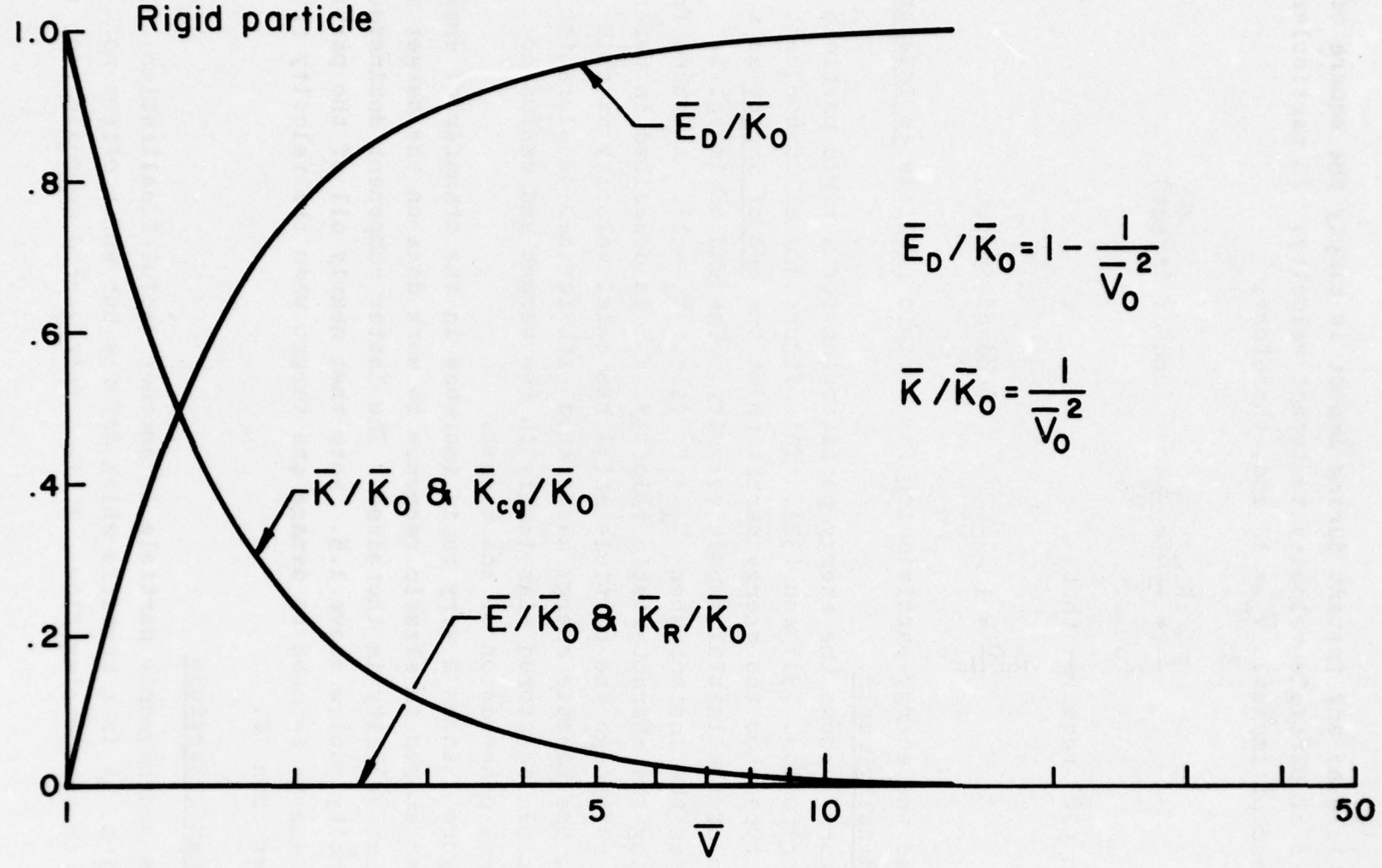

Figure 7. Energy partition vs. impact velocity

a low viscosity liquid such as water. The hydrodynamic particle introduces a third component into the energy partition, i.e., the relative kinetic energy due to deformation. Thus,

$$\bar{K}_o = \bar{K}_{cg} + \bar{K}_R + \bar{E}_D \qquad \text{(hydrodynamic)} \tag{33}$$

Figures 8, 9, and 10 show the energy components as a function of impact velocity for density ratios of 0.1, 1.0, and 10, respectively. Several trends should be noted. First, for low impact velocities, most of the energy is stored as elastic response of the target. The lighter the particle, the larger the velocity at which this component dominates.

Second, for very large velocities, the elastic energy is insignificant compared to both the lateral kinetic energy of the particle and the work performed on the target. For the heavy particle, 90% of the energy represents work done on the target and 10% represents the lateral kinetic energy in the particle. In contrast, the light particle deforms more and does less work on the target. As a result, the two components are nearly equal.

Third, another difference between high and low $\bar{\rho}$ impacts should be noted for velocity ratios above 10. When $\bar{\rho} < 1$, the particle is fully embedded in the target ($\bar{y}/\bar{\ell} > 1$). Hence, all of the energy is expended on the target. In contrast, when $\bar{\rho} > 1$, the particle is only partially embedded in the target, and much of the energy accompanies the particle ejecta and is dissipated by the air surrounding the target.

Transfer of energy between the various modes in the transition regime ($2 < \bar{V} < 10$) is apparently a complicated process which a study of Figures 8-10 indicates. A parameter which is useful for an understanding of this coupling is the deformation parameter $\bar{\xi}$. It is defined as

$$\bar{\xi} = \frac{1}{2}\frac{d\bar{\ell}}{d\tau} \tag{34}$$

where $\bar{\ell}$ represents the nondimensional thickness of the particle. In the absence of any strong elastic restoring forces, the particle is compressed during impact. Hence, $\bar{\xi}$ is a negative quantity.

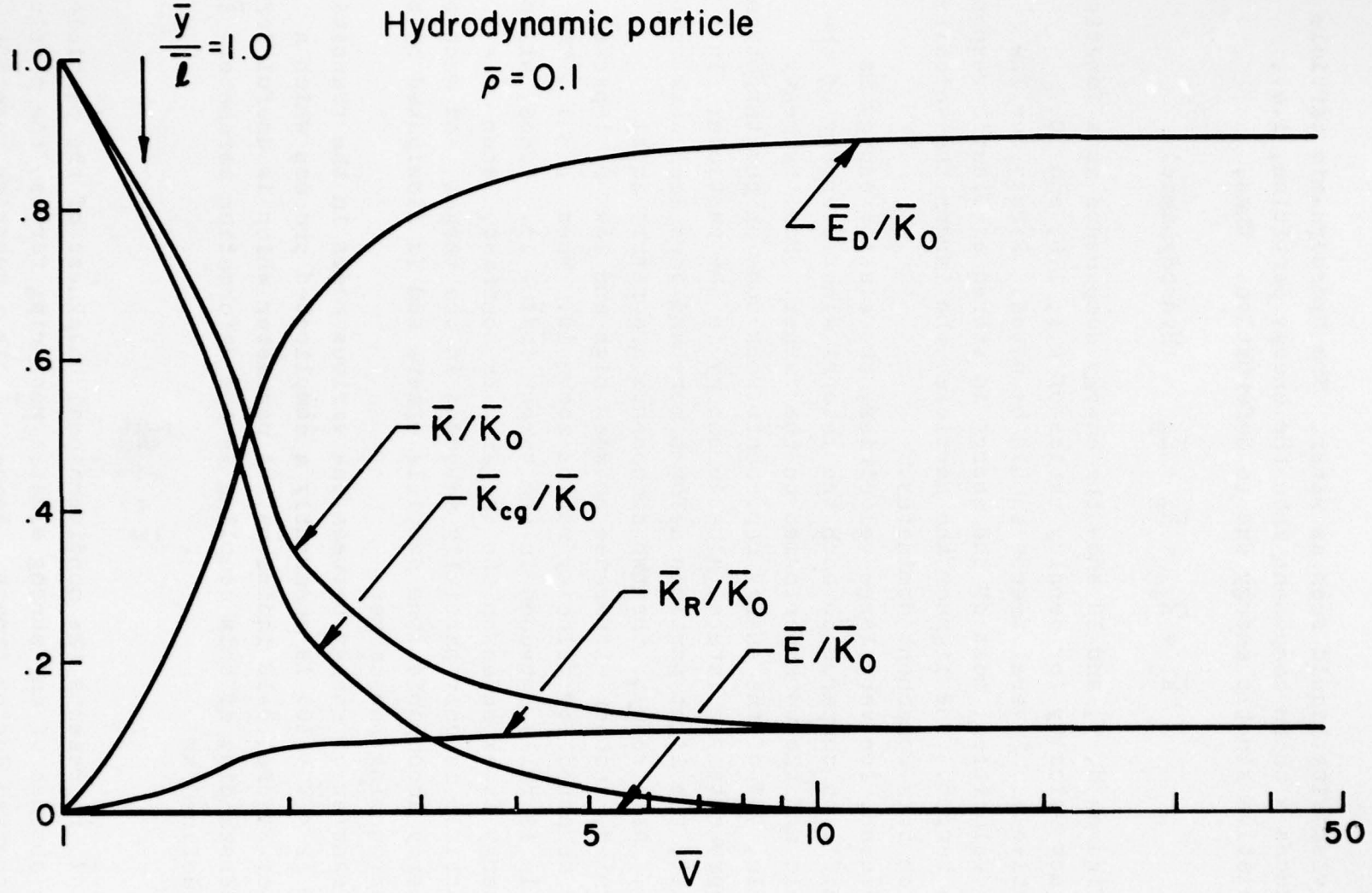

Figure 8. Energy partition vs. impact velocity

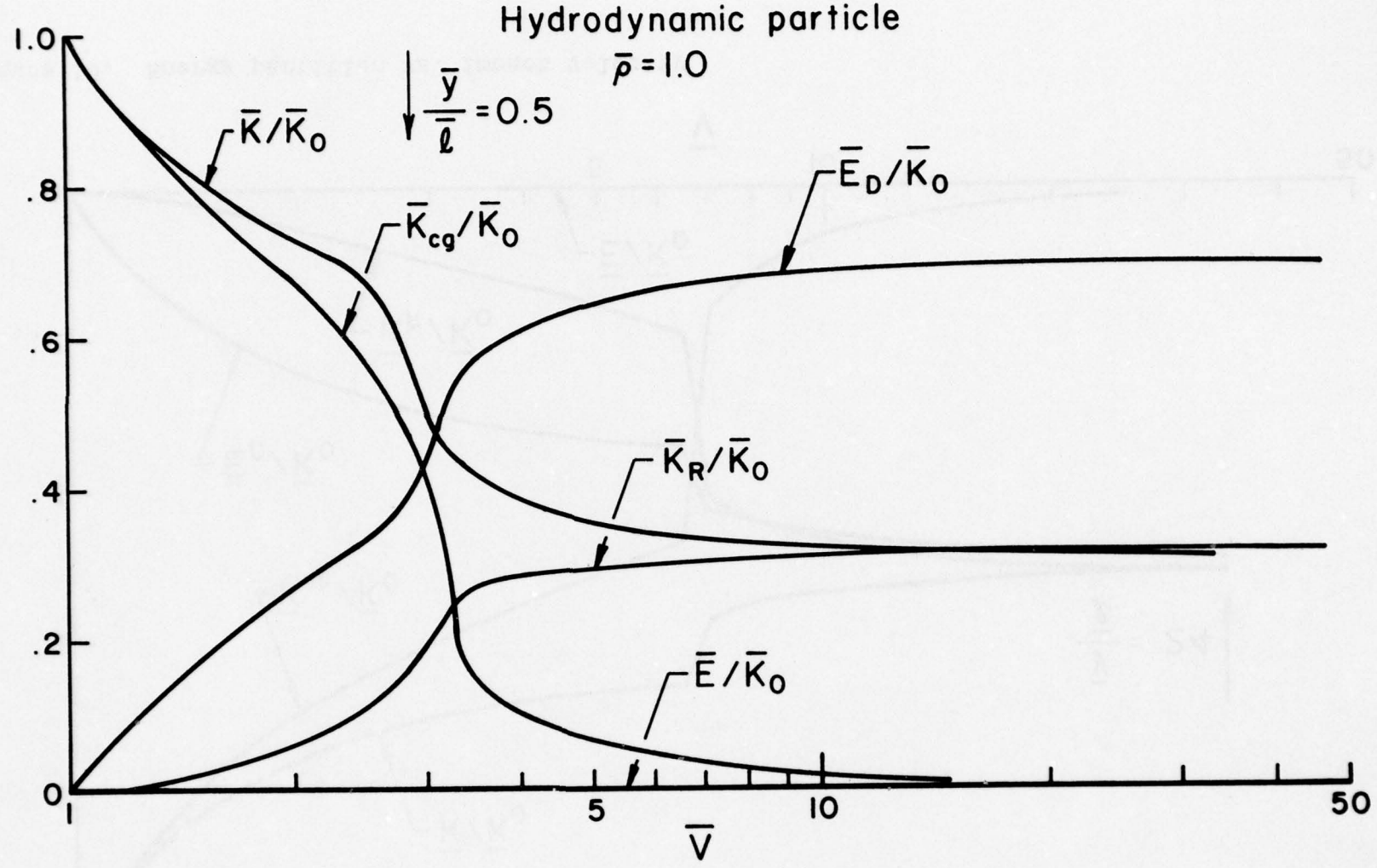

Figure 9. Energy partition vs. impact velocity

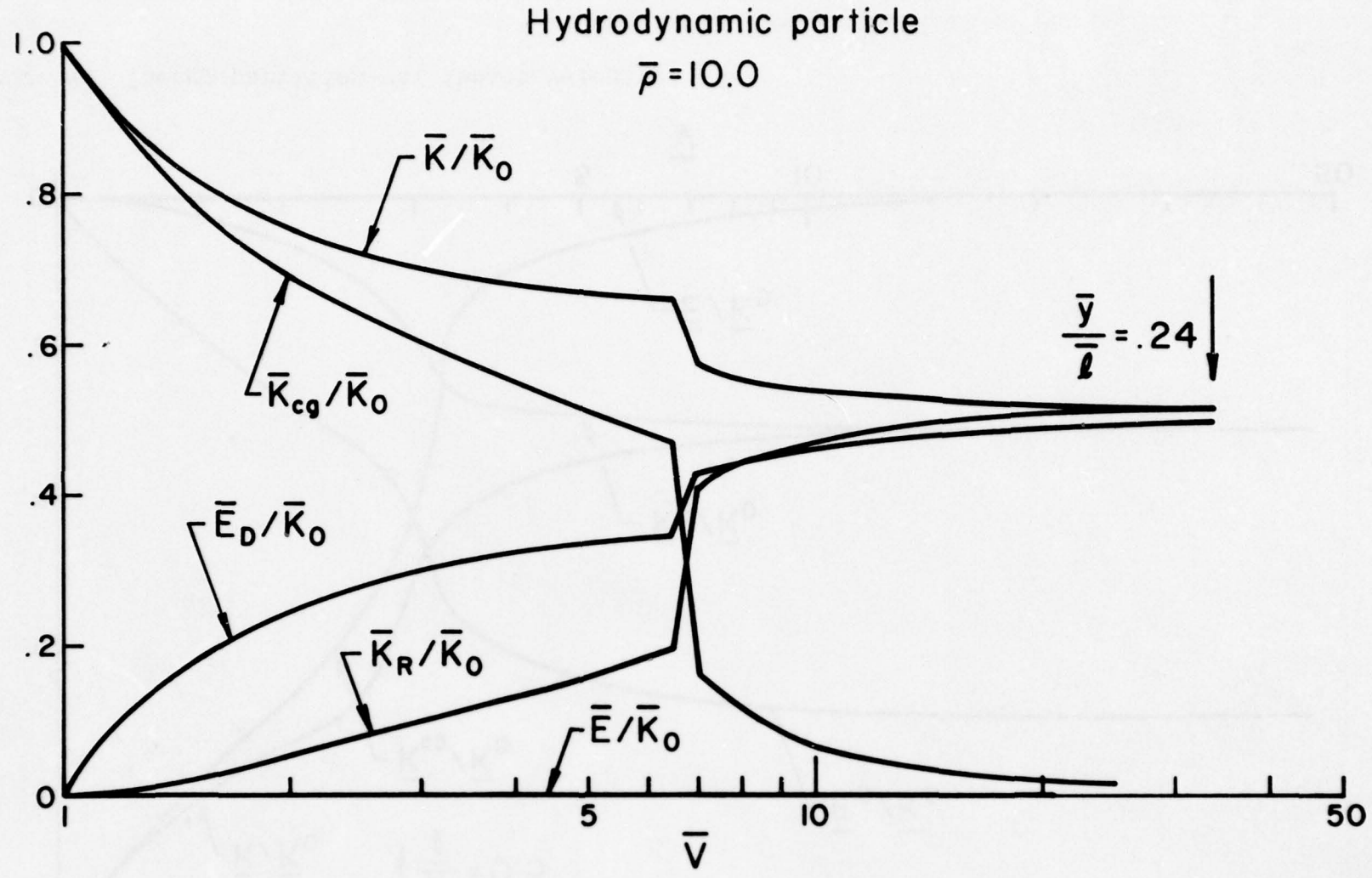

Figure 10. Energy partition vs. impact velocity

In the following discussion, it is convenient to recast $\bar{\xi}$ in terms of particle velocity and to work with positive numbers. It is easy to show that for a linear velocity field the deformation parameter may be written

$$-\bar{\xi} = \bar{V}_{cg} - \bar{V}_{\perp} \tag{35}$$

i.e., it represents the rate at which the particle center of mass approaches the impact surface.

Figure 11 shows the deformation parameter as a function of time for $\bar{\rho} = 1.0$ and for several values of impact velocity. The final point on each curve coincides with the end of impact. It is evident that the initial deformation rate is greater for greater impact velocity. However, during a given impact, the rate of deformation decreases; the particle, in effect, becomes "stiffer." Eventually, if the impact velocity is high enough, the deformation parameter reaches a peak value and then decays. For the case $\bar{\rho} = 1.0$, the peak is reached during impact for $\bar{V} > 3$. This value is the same as the velocity at which the sudden transition occurs in Figure 9. A similar study of deformation histories for $\bar{\rho} = 10$ indicates flattening at $\bar{V}_{\perp} = 6.5$, which also corresponds to the transition on Figure 10. For $\bar{\rho} = 0.1$, the study shows the deformation history occurs even for the lowest impact velocities treated.

Further illustration is contained in Figure 12 which shows the deformation parameter for each density ratio at $\bar{V} = 3.32$. Three characteristics should be noted. First, the time scale of the impact process varies inversely as $\bar{\rho}$, i.e., the heavier the particle, the more time required to decelerate it. Second, the peak value for $(-\bar{\xi})$ has not been reached for the light particle, whereas it has been passed for the heavy particle. Hence, the relative kinetic energy is still increasing rapidly for the light particle (Fig. 10) whereas it is approaching the high velocity limit for the heavy particle (Fig. 8). Finally, the value of $(-\bar{\xi})$ at the end of impact increases with $\bar{\rho}$. The latter effect helps to explain the $\bar{K}_{cg}$ curves in Figures 8, 9, and 10. It is easy to show that, using Eq. (35),

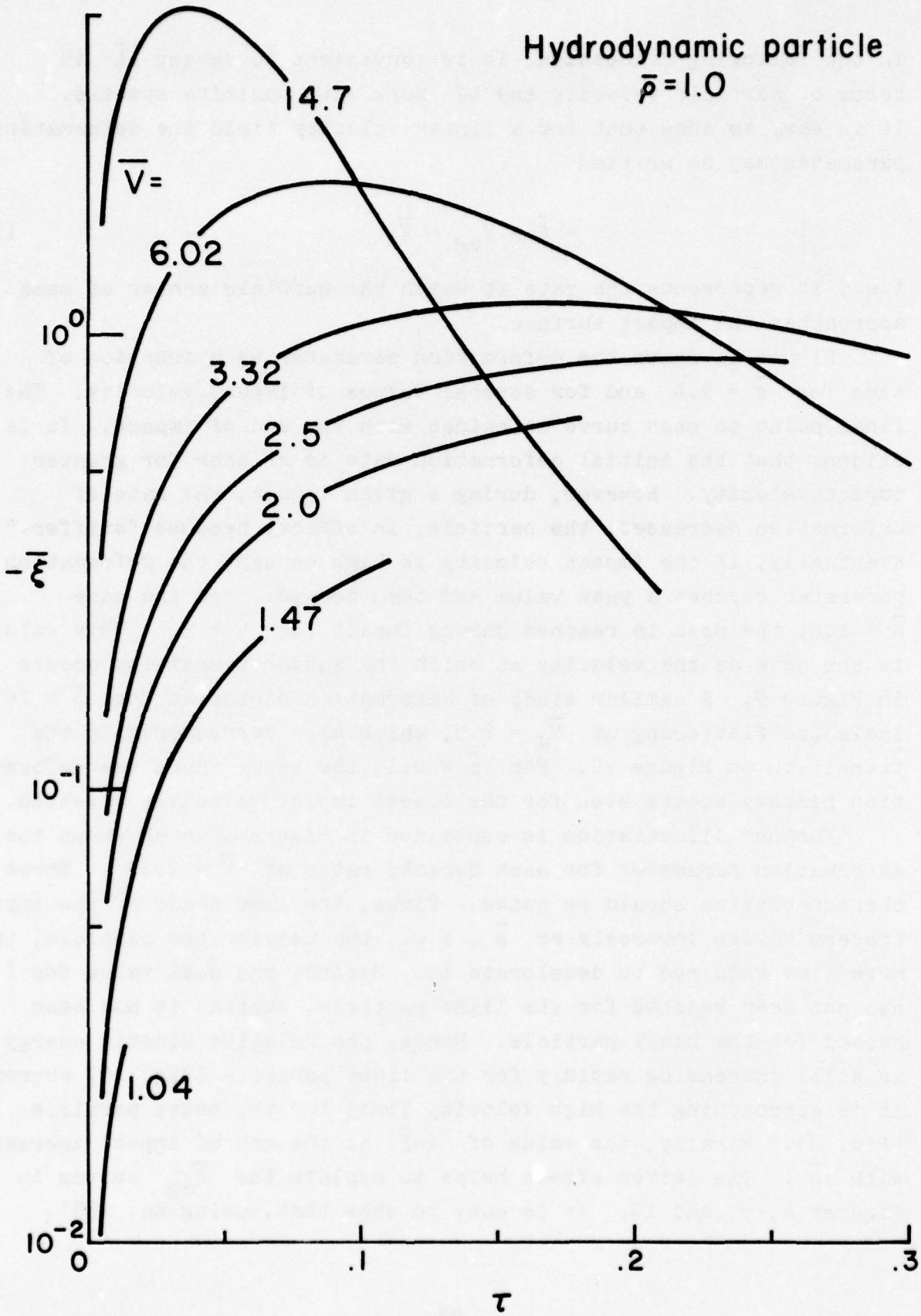

Figure 11. Deformation parameter vs. time

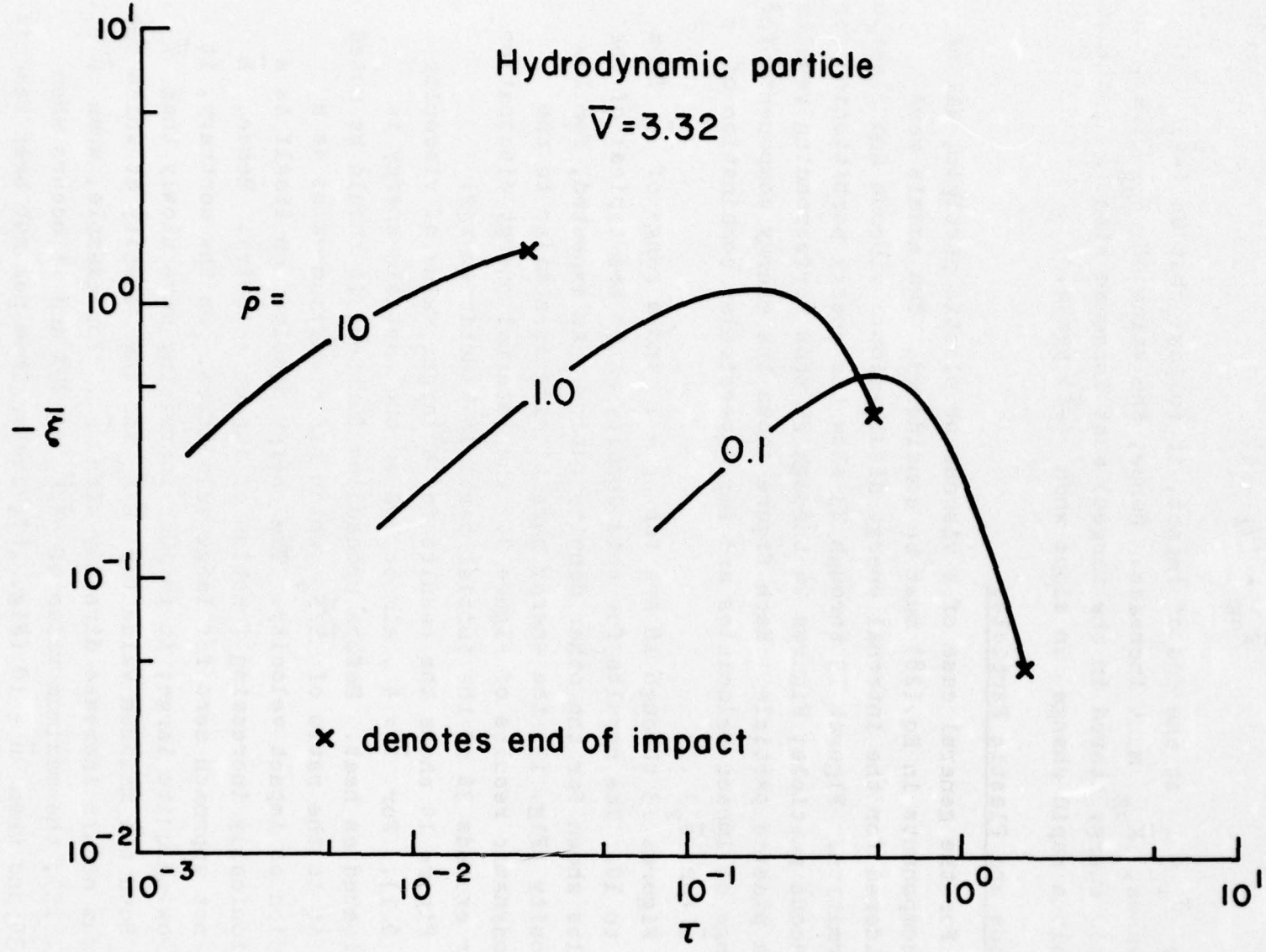

Figure 12. Deformation parameter vs. time

$$\bar{K}_{cg} = (\bar{V}_{\perp} - \bar{\xi})^2 \tag{36}$$

Since $\bar{V}_{\perp} = 1$ at the end of impact, it follows that as $(-\bar{\xi})$ increases, $\bar{K}_{cg}$ must increase. Hence, the value of $\bar{K}_{cg}$ (i.e., the elastic energy stored in the target) must increase with $\bar{\rho}$ and must exhibit a rapid change in slope when $(-\bar{\xi})$ peaks.

Viscous and Plastic Particles

For the general case of a viscous or plastic particle, all of the components in Eq.(28) must be considered. Two models were considered for the internal energy dissipation: viscous and plastic deformation. Figures 13 through 23 show the energy partitioning for a viscous particle; Figures 24 through 29 show corresponding results for a plastic particle. Each figure shows the energy components for a range of impact velocities and for a particular combination of $\bar{\rho}$ and $\bar{\mu}$ (or $\bar{\sigma}_y$) .

Figures 13 through 16 are for $\bar{\rho} = 1$ and a range of $\bar{\mu}$ from 0.01 to 10. The results for this density ratio are typical of the results shown for the other density ratios. As expected, for low viscosity (Fig. 13) the energy partitioning is similar to the hydrodynamic results of Figure 9. The internal energy dissipation never exceeds 3% of the initial particle kinetic energy.

Figure 14 shows the results for a larger value of viscosity ($\bar{\mu} = 0.1$). For $\bar{V} \simeq 4$, almost 20% of the particle energy is dissipated as heat. Before proceeding further, it should be noted that it is the ratio of $\bar{E}/\bar{K}_o$ which has a maximum value as a function of impact velocity. The energy dissipation itself is a monotonically increasing function of impact velocity. Hence, $\bar{E}$ does not approach zero for large velocities. On the contrary, it is growing quite large; it is just increasing more slowly than $\bar{K}_o$.

Both the maximum value for $\bar{E}/\bar{K}_o$ and the velocity at which the maximum occurs increase directly with $\bar{\mu}$. For example, when $\bar{\mu} = 1$ (Fig. 15), the maximum value of $\bar{E}/\bar{K}_o$ is 25% and it occurs when $\bar{V} = 35$;and when $\bar{\mu} = 10$ (Fig. 16), the maximum has not been reached

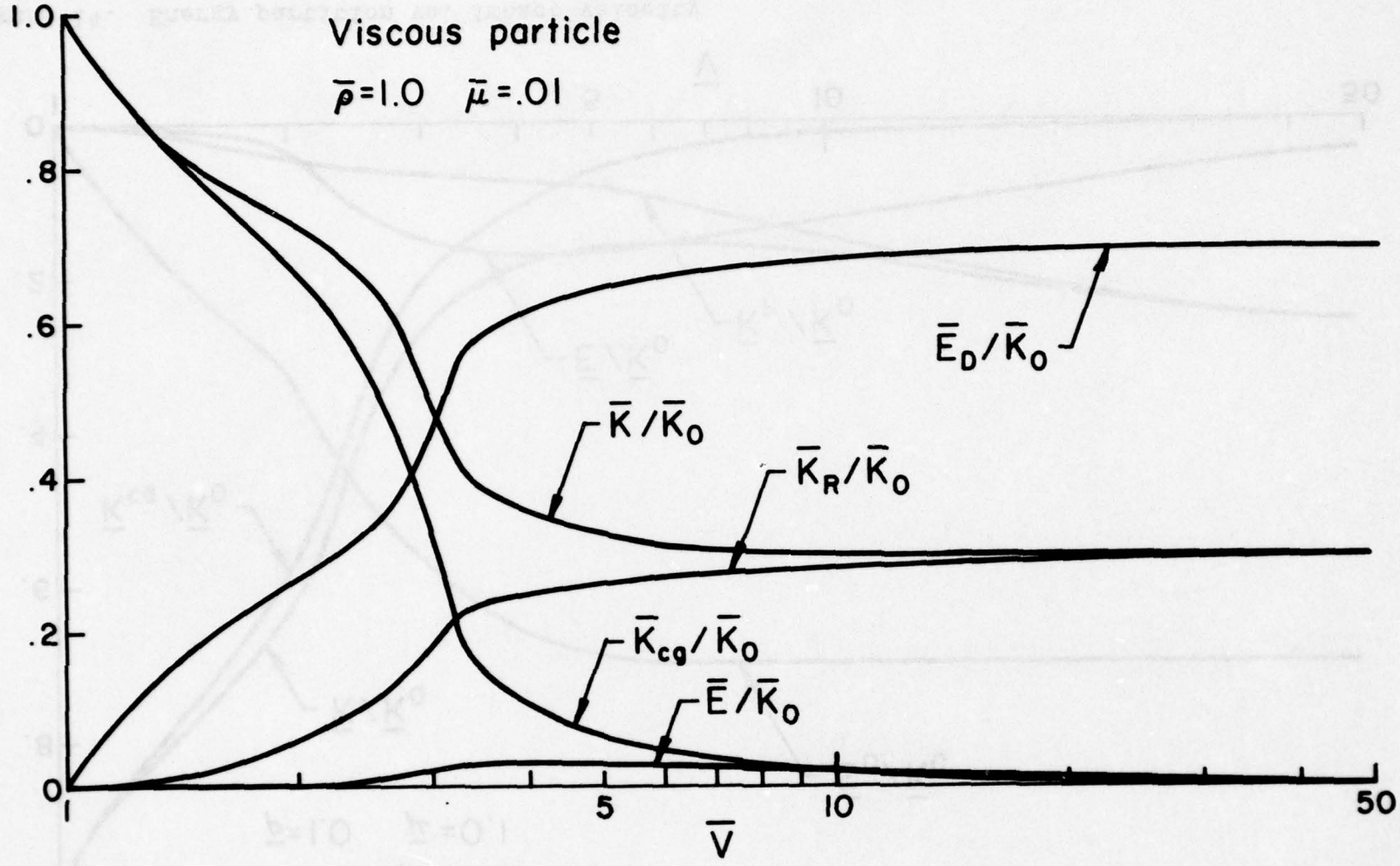

Figure 13. Energy partition vs. impact velocity

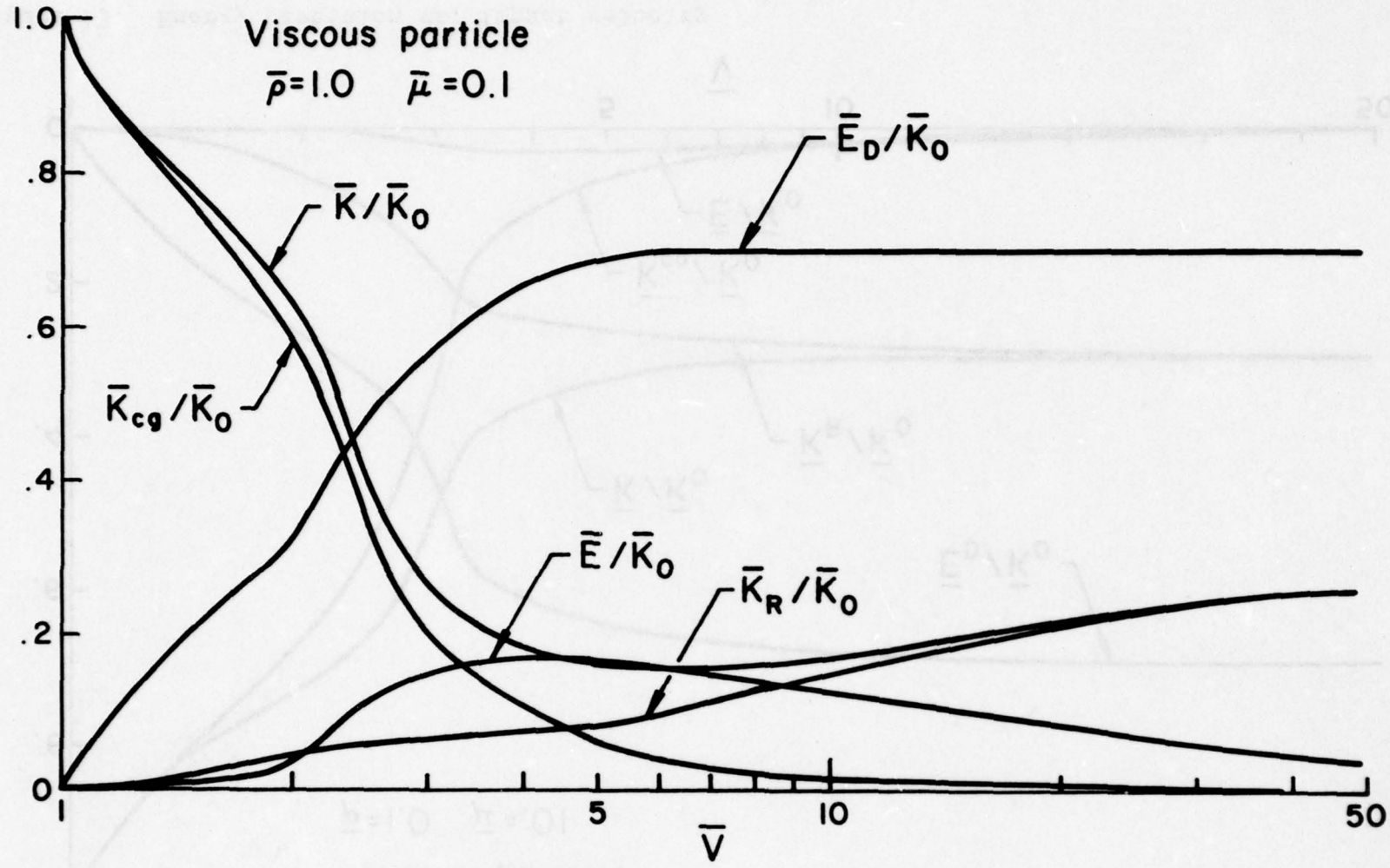

Figure 14. Energy partition vs. impact velocity

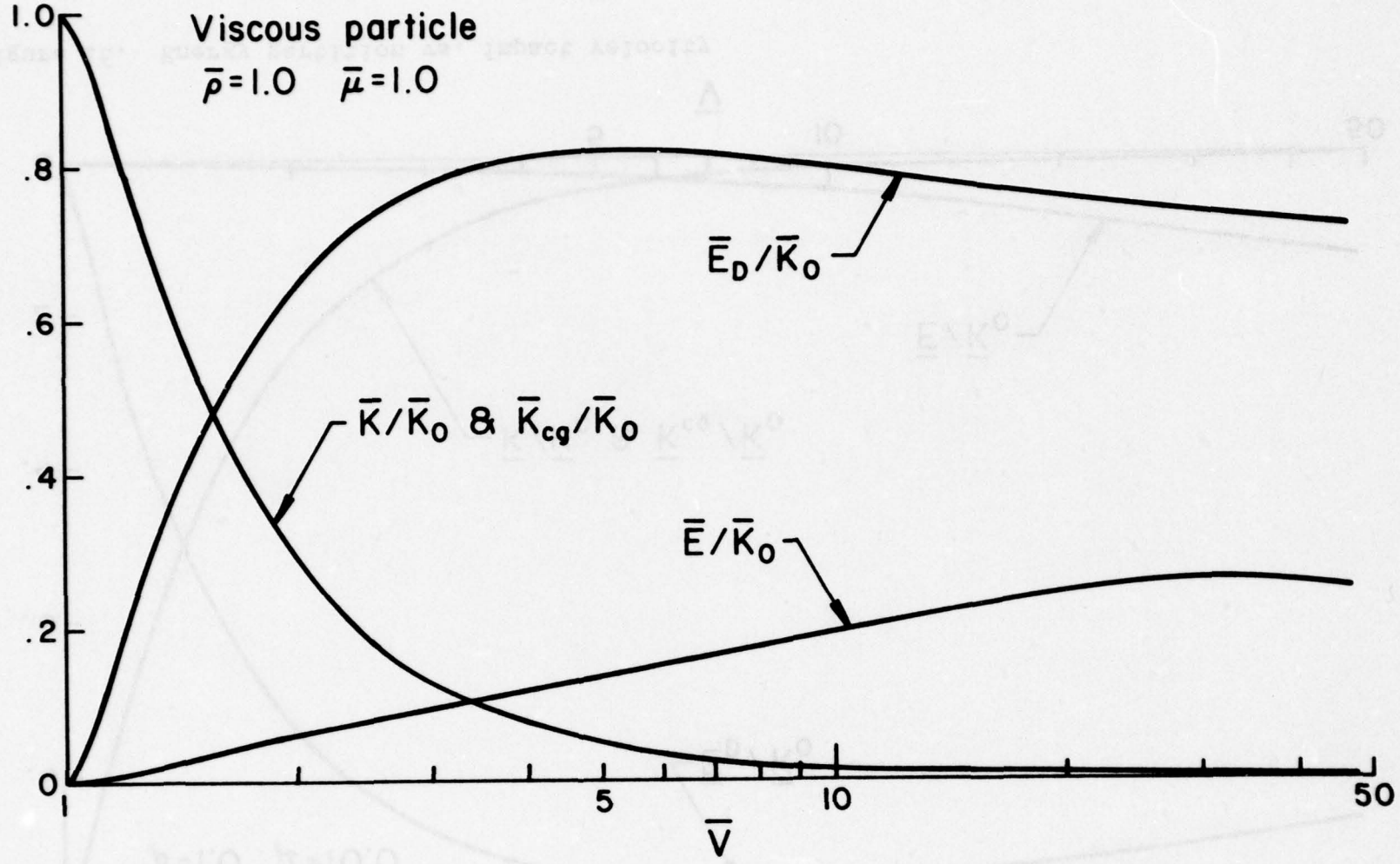

Figure 15. Energy partition vs. impact velocity

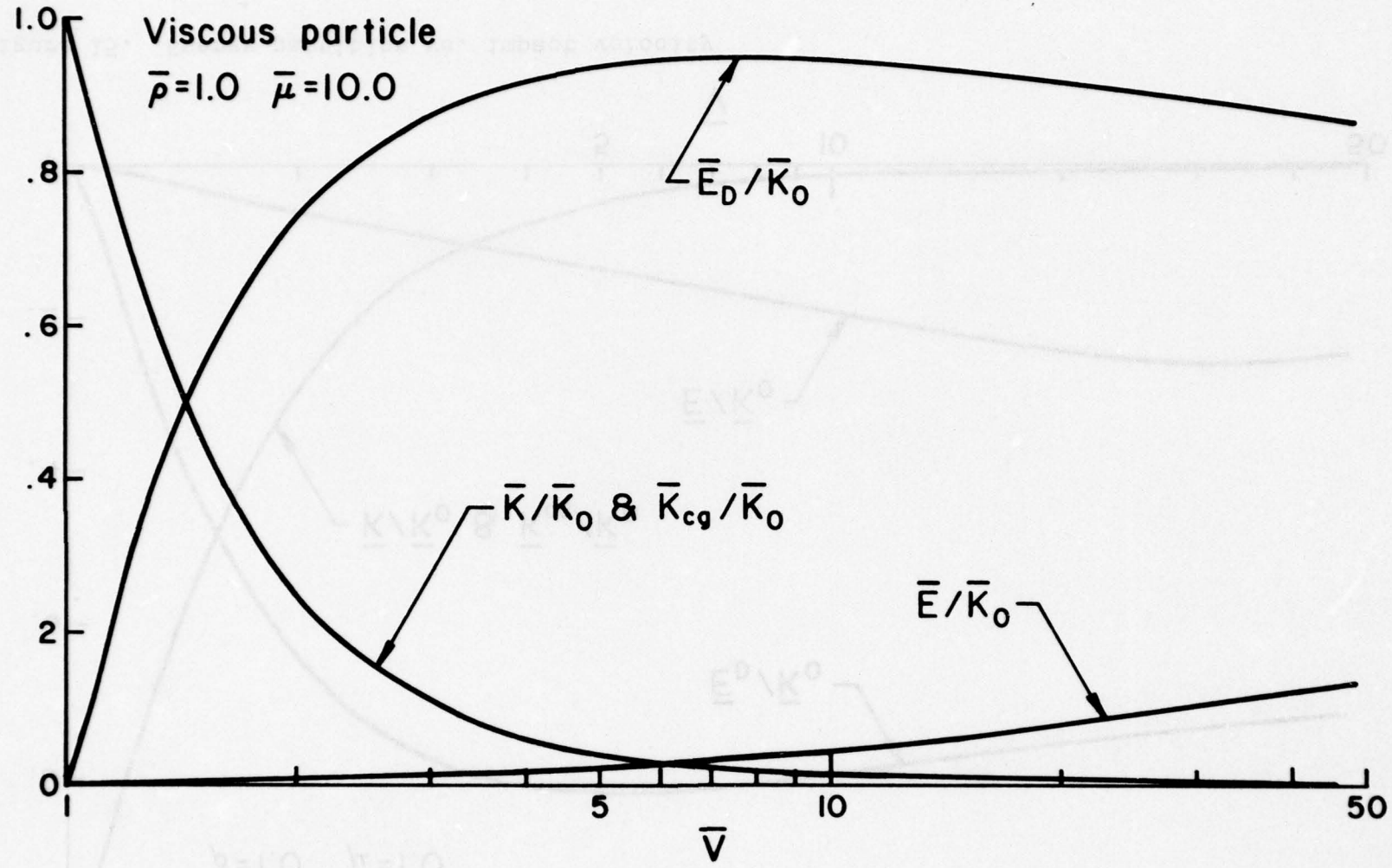

Figure 16. Energy partition vs. impact velocity

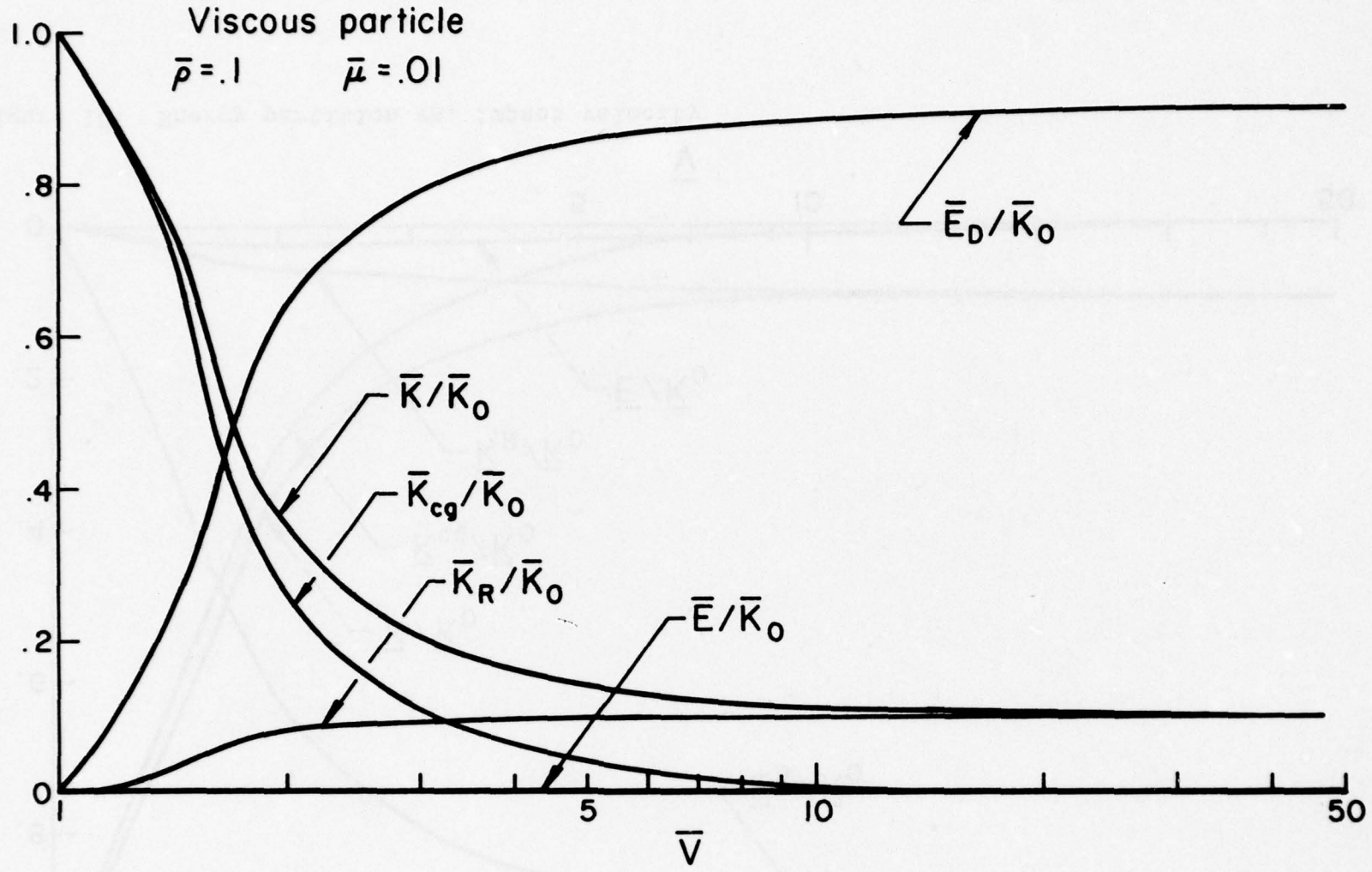

Figure 17. Energy partition vs. impact velocity

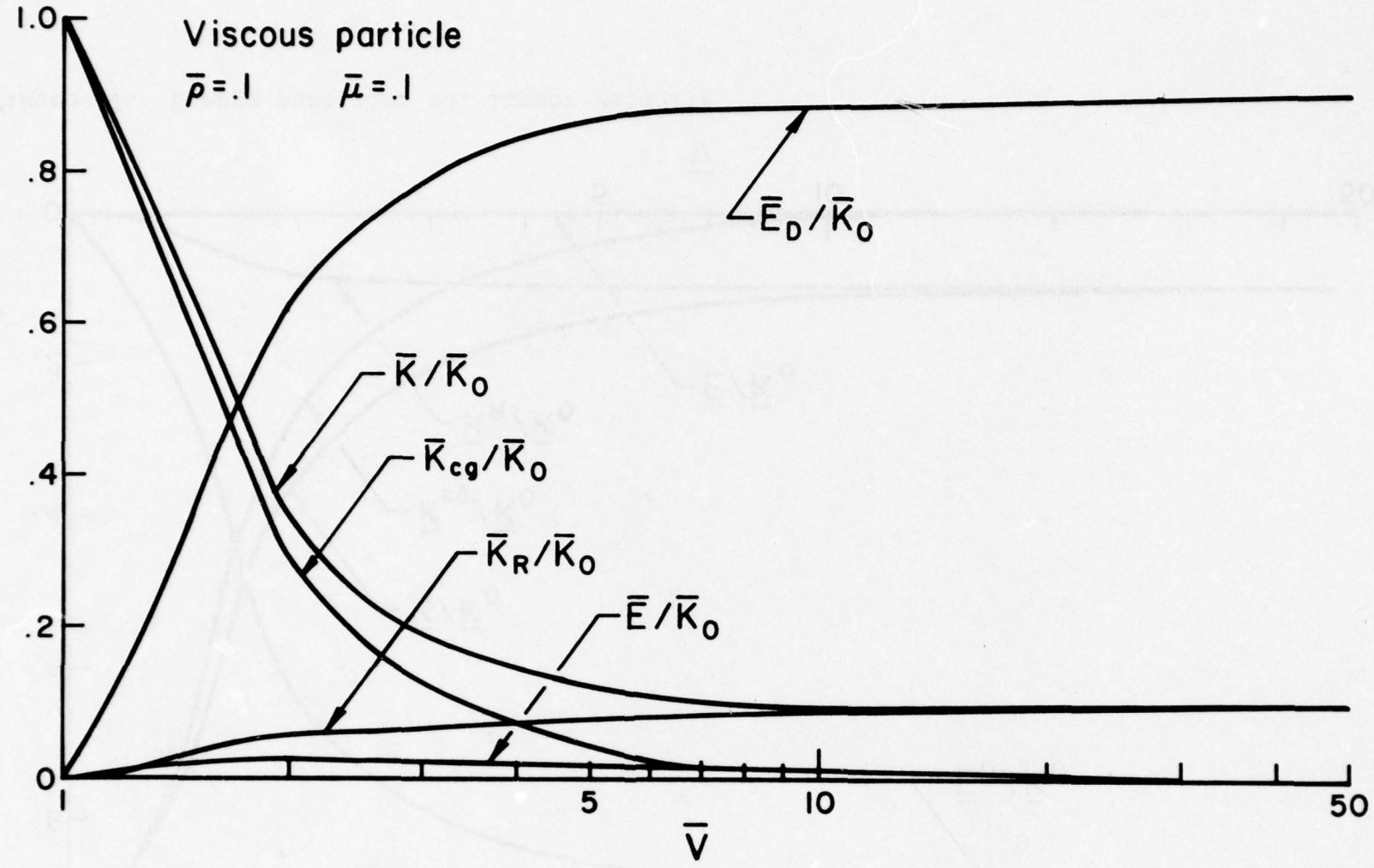

Figure 18. Energy partition vs. impact velocity

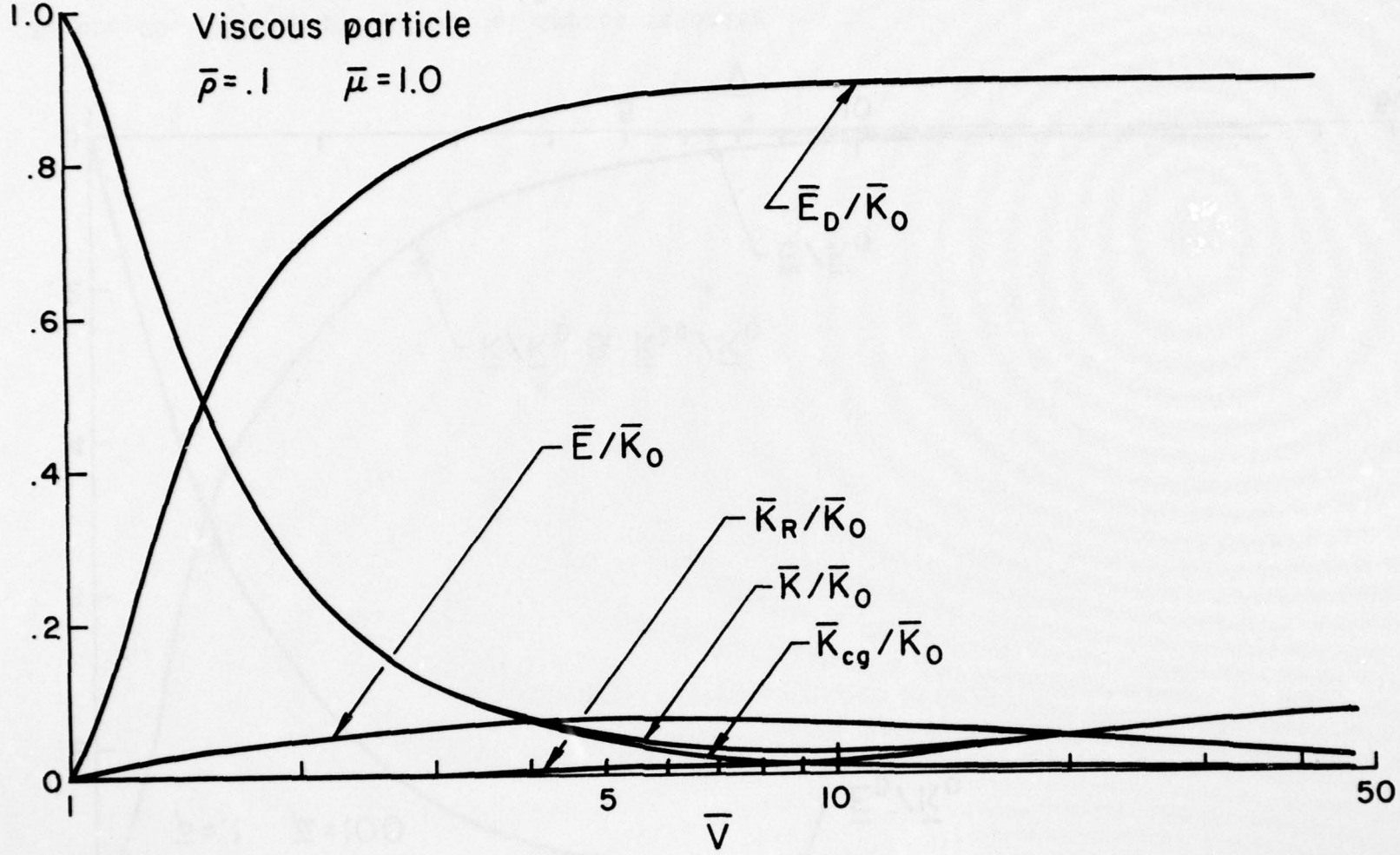

Figure 19. Energy partition vs. impact velocity

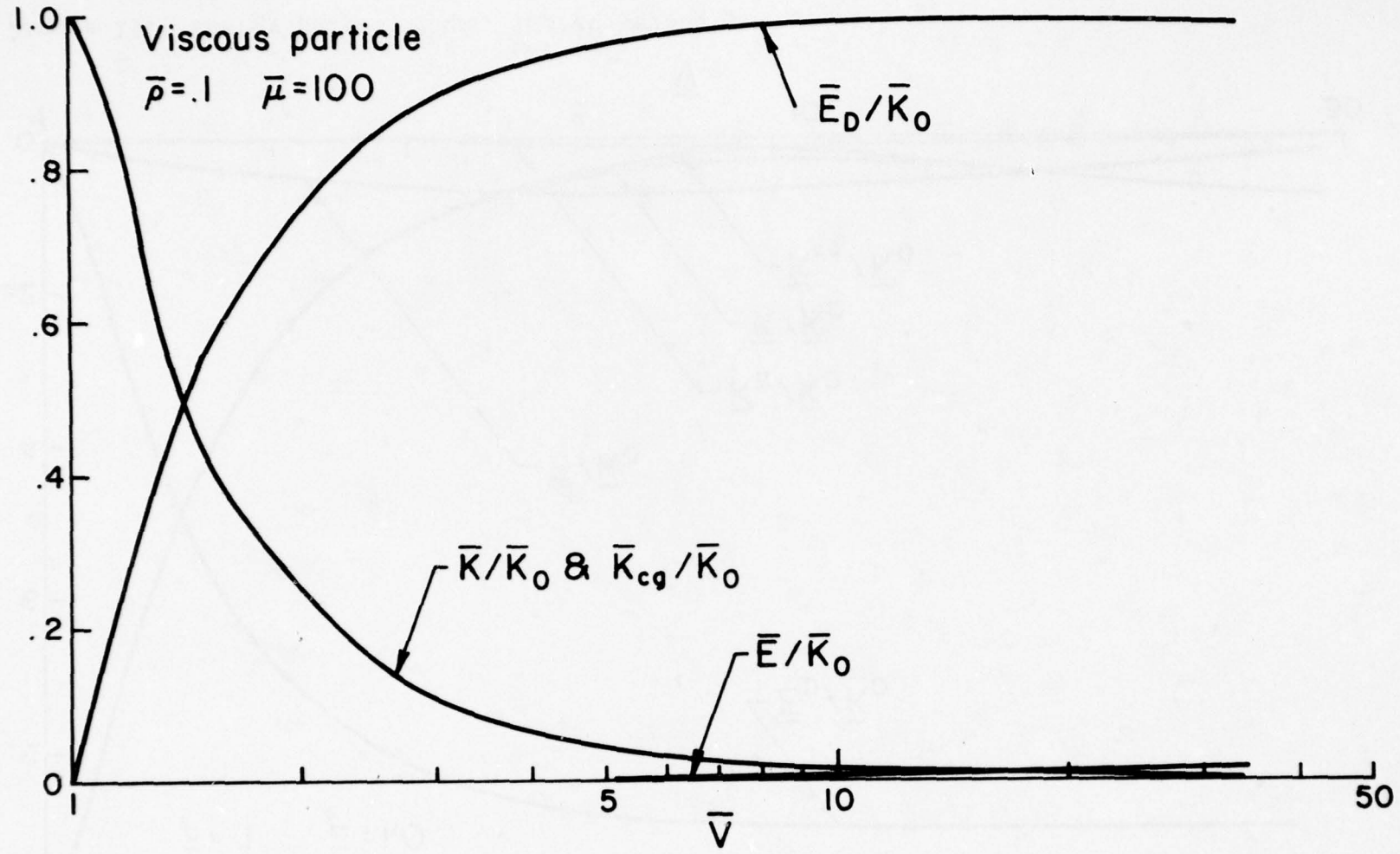

Figure 20. Energy partition vs. impact velocity

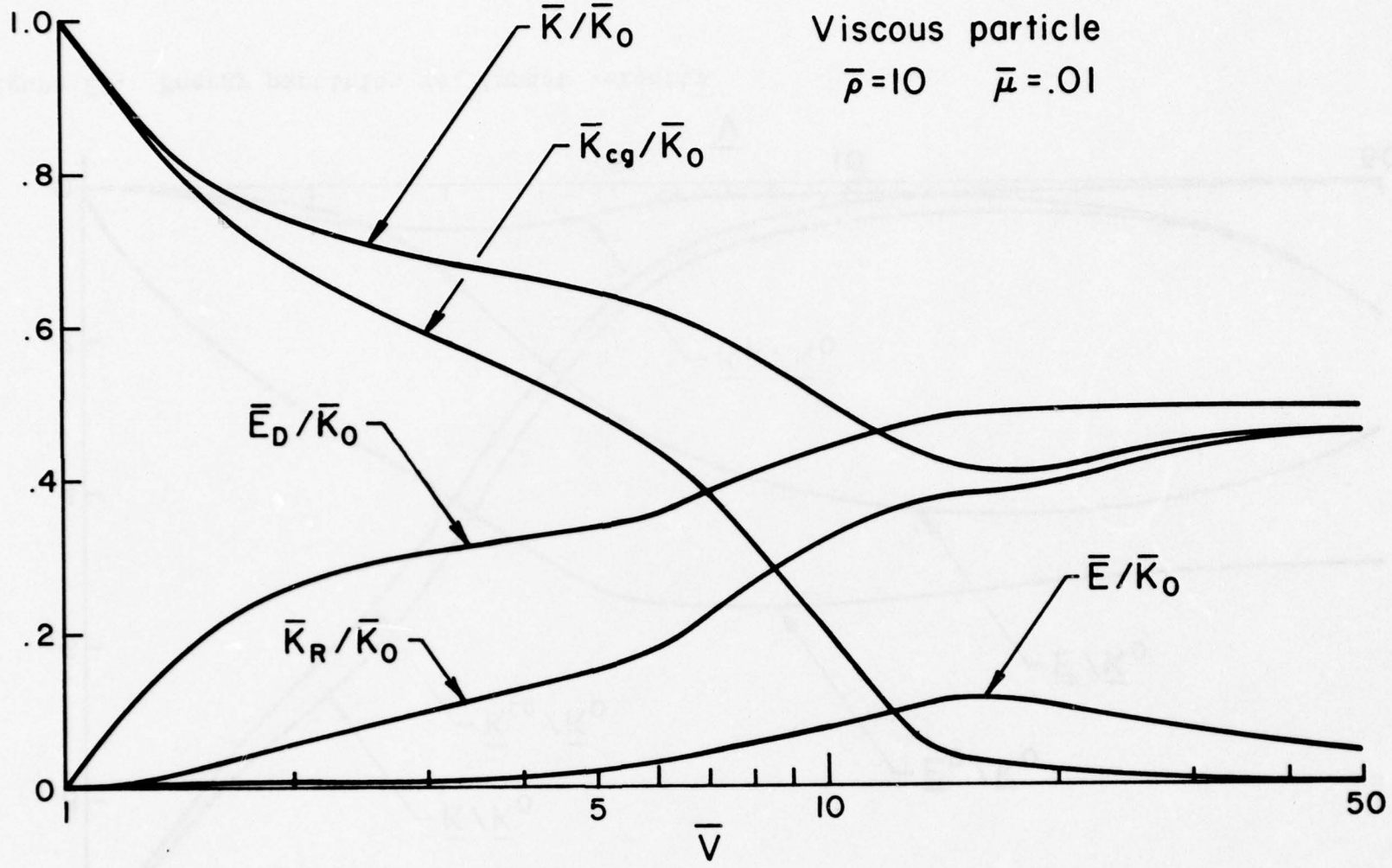

Figure 21. Energy partition vs. impact velocity

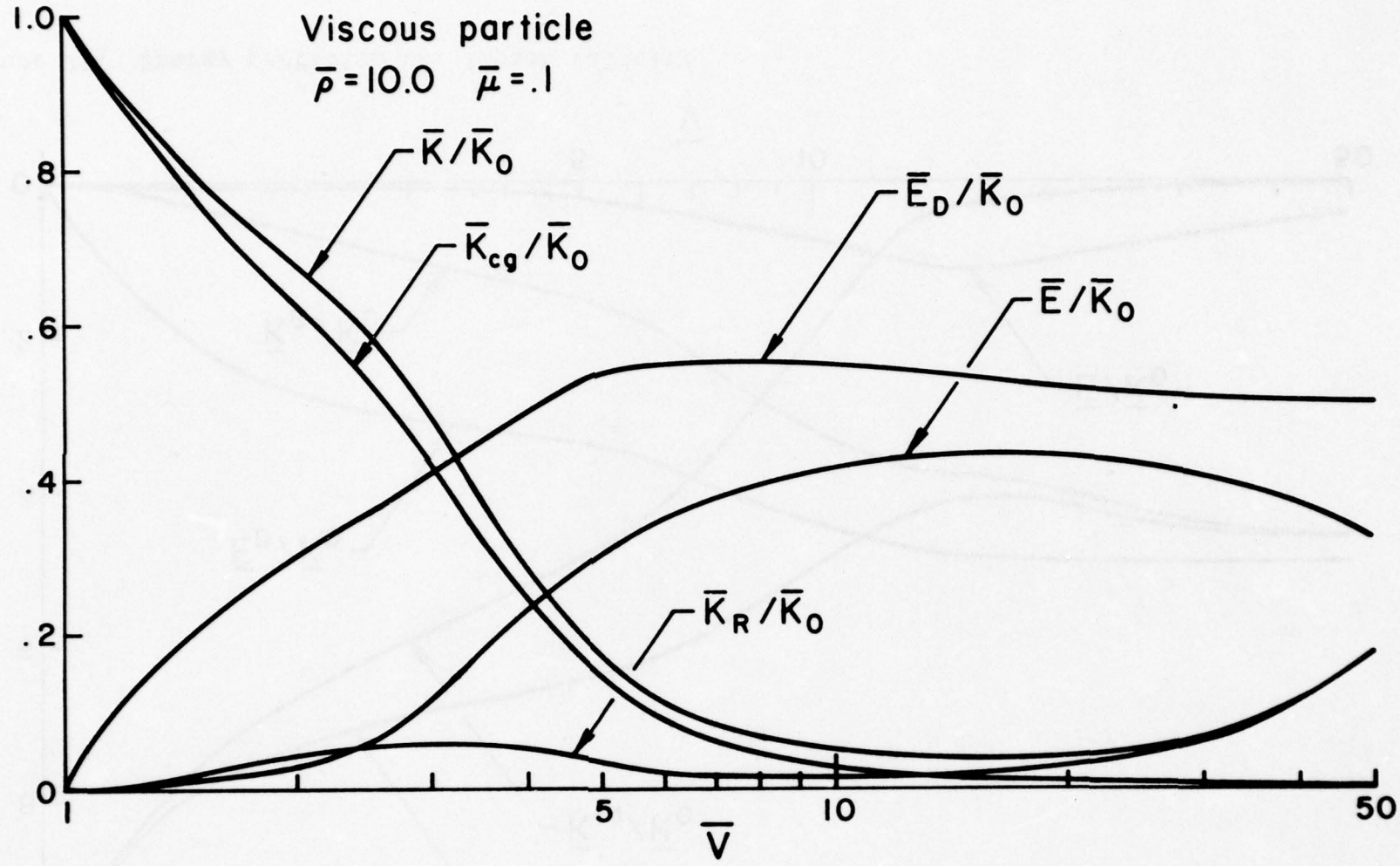

Figure 22. Energy partition vs. impact velocity

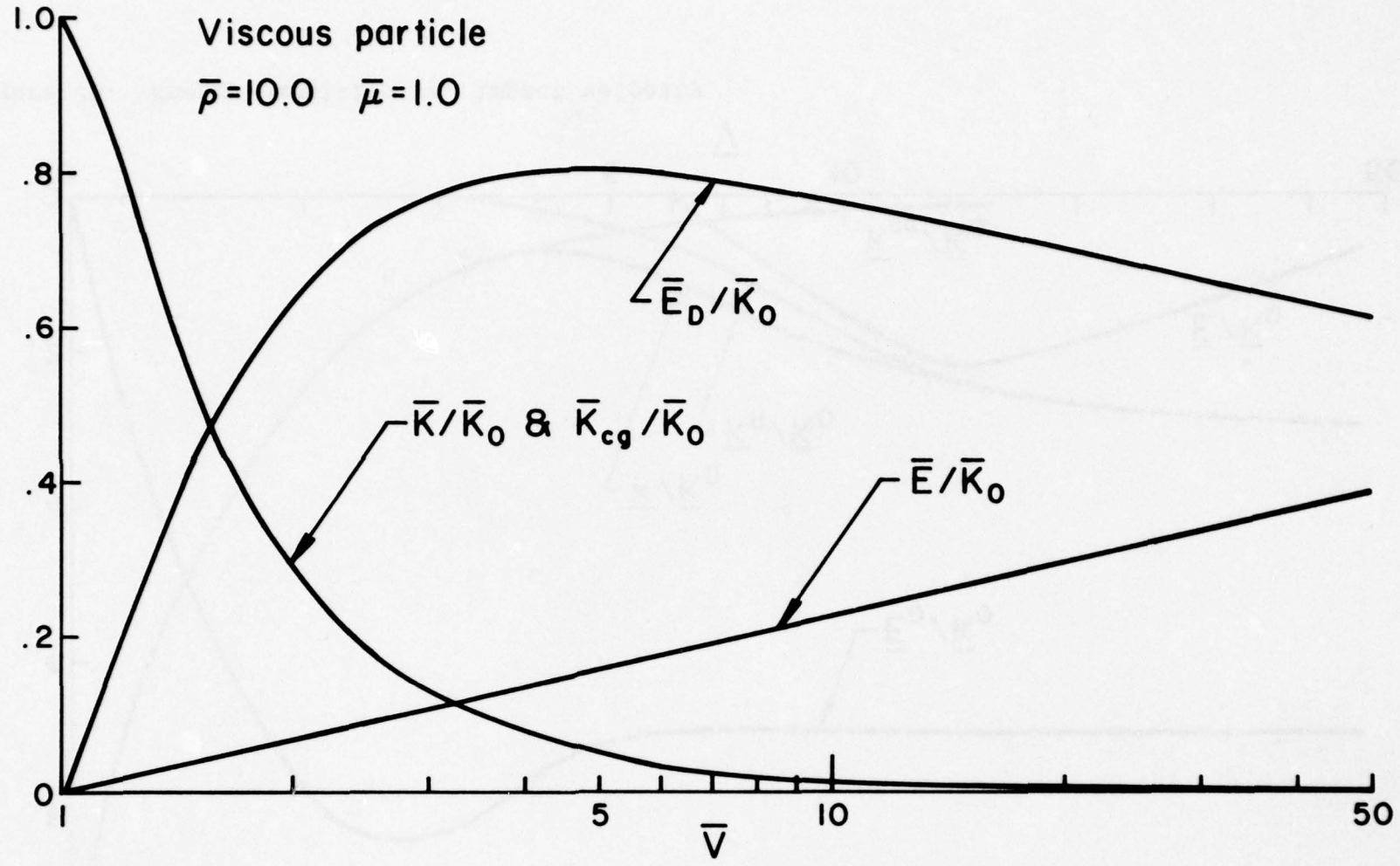

Figure 23. Energy partition vs. impact velocity

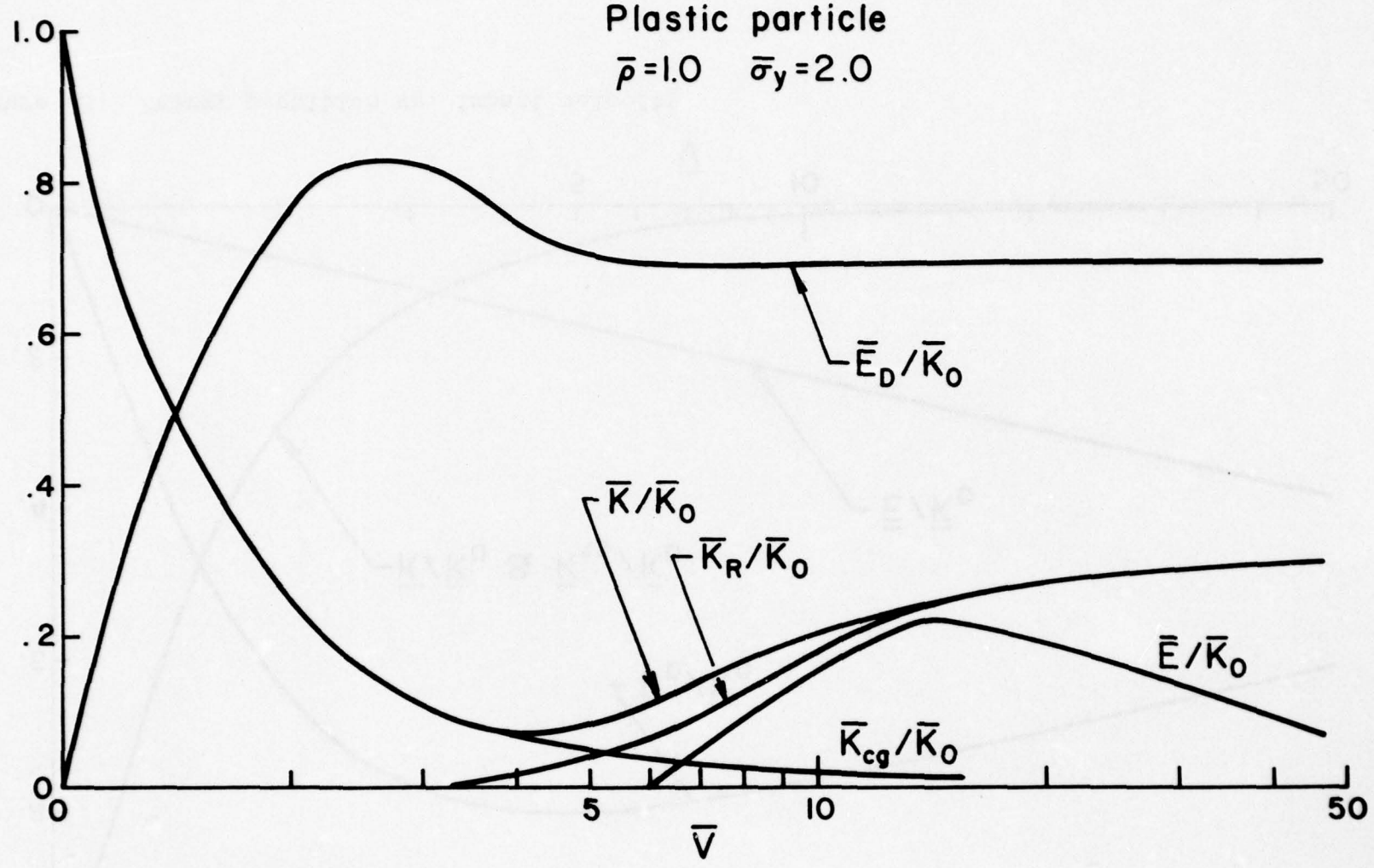

Figure 24. Energy partition vs. impact velocity

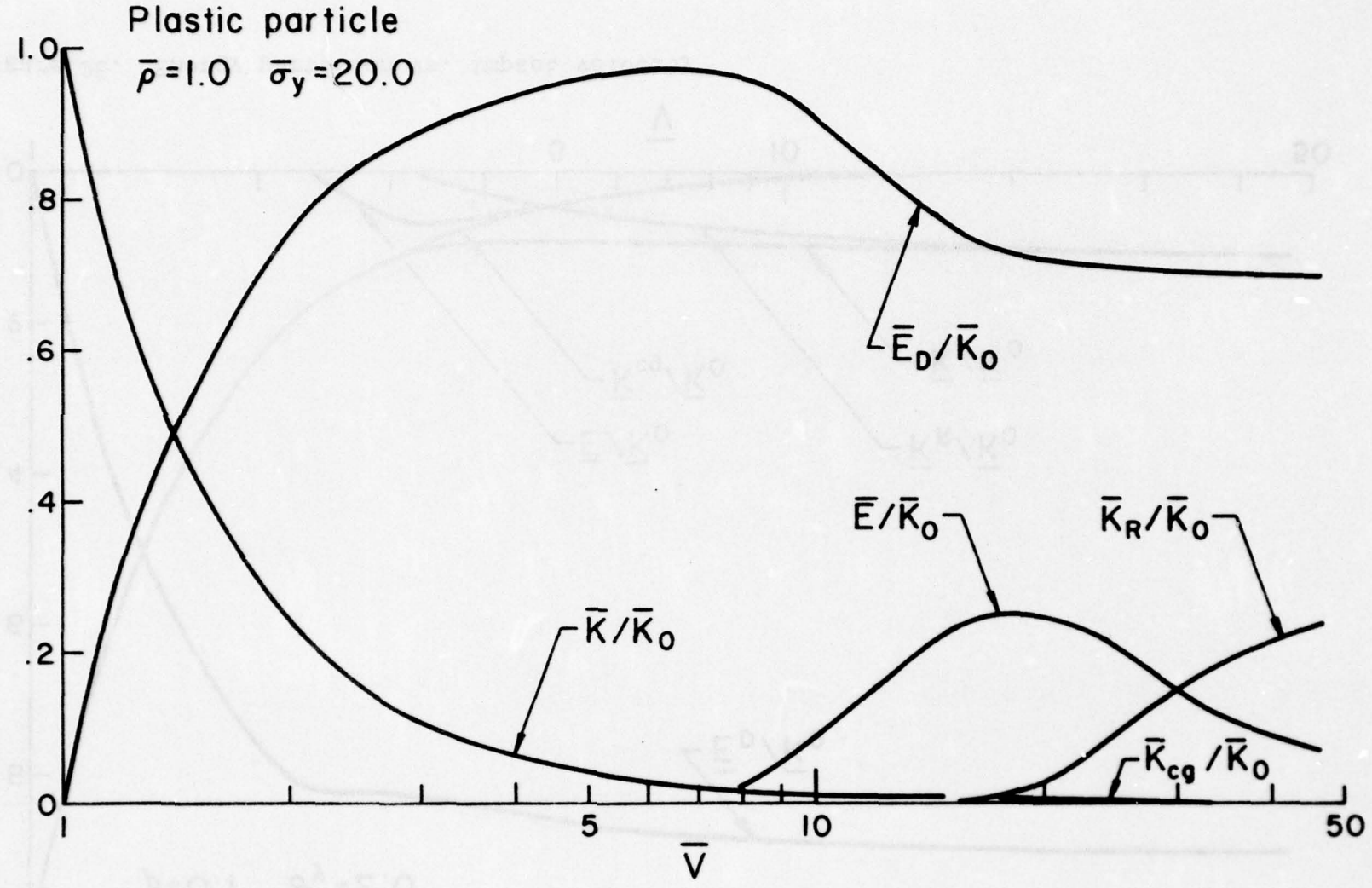

Figure 25. Energy partition vs. impact velocity

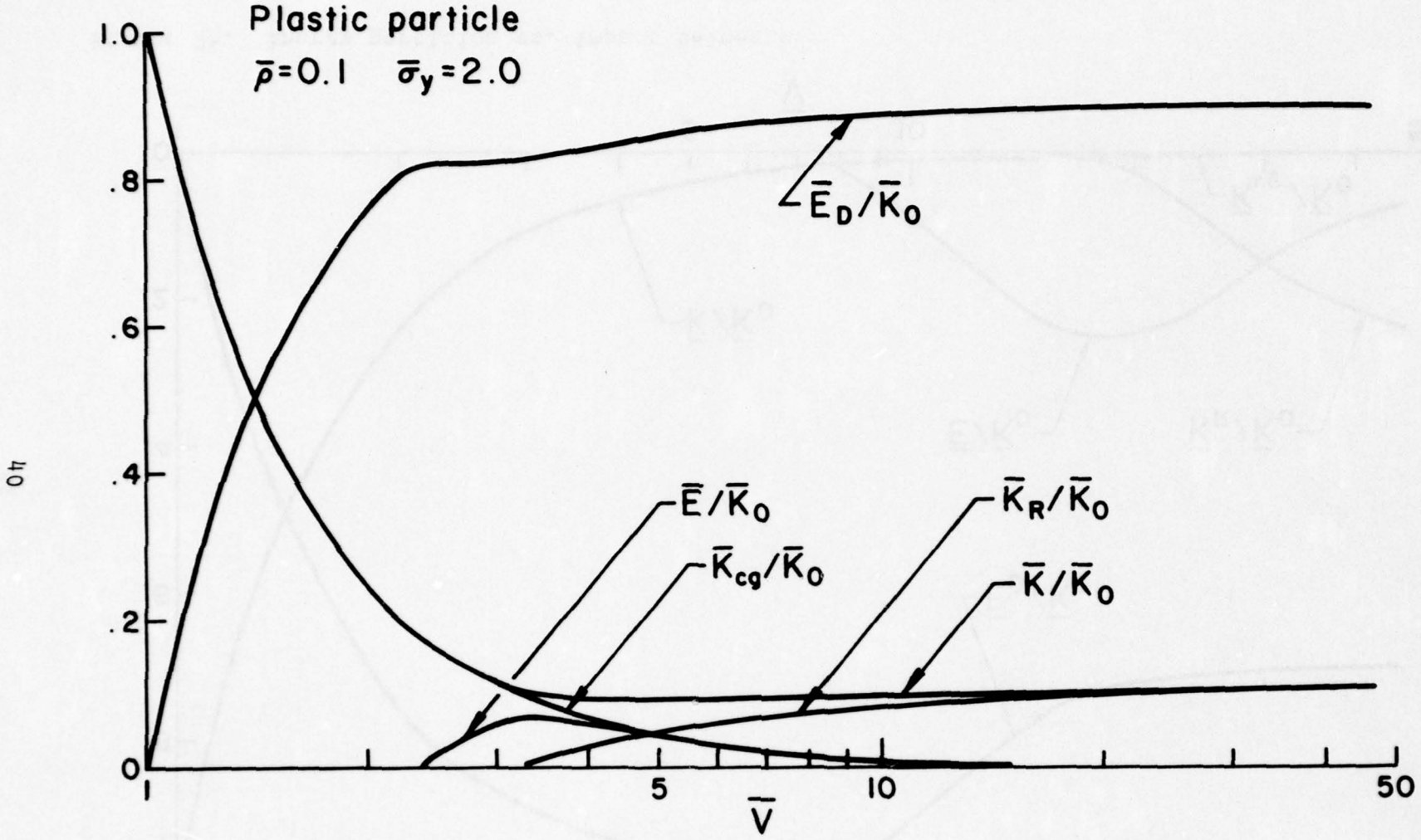

Figure 26. Energy partition vs. impact velocity

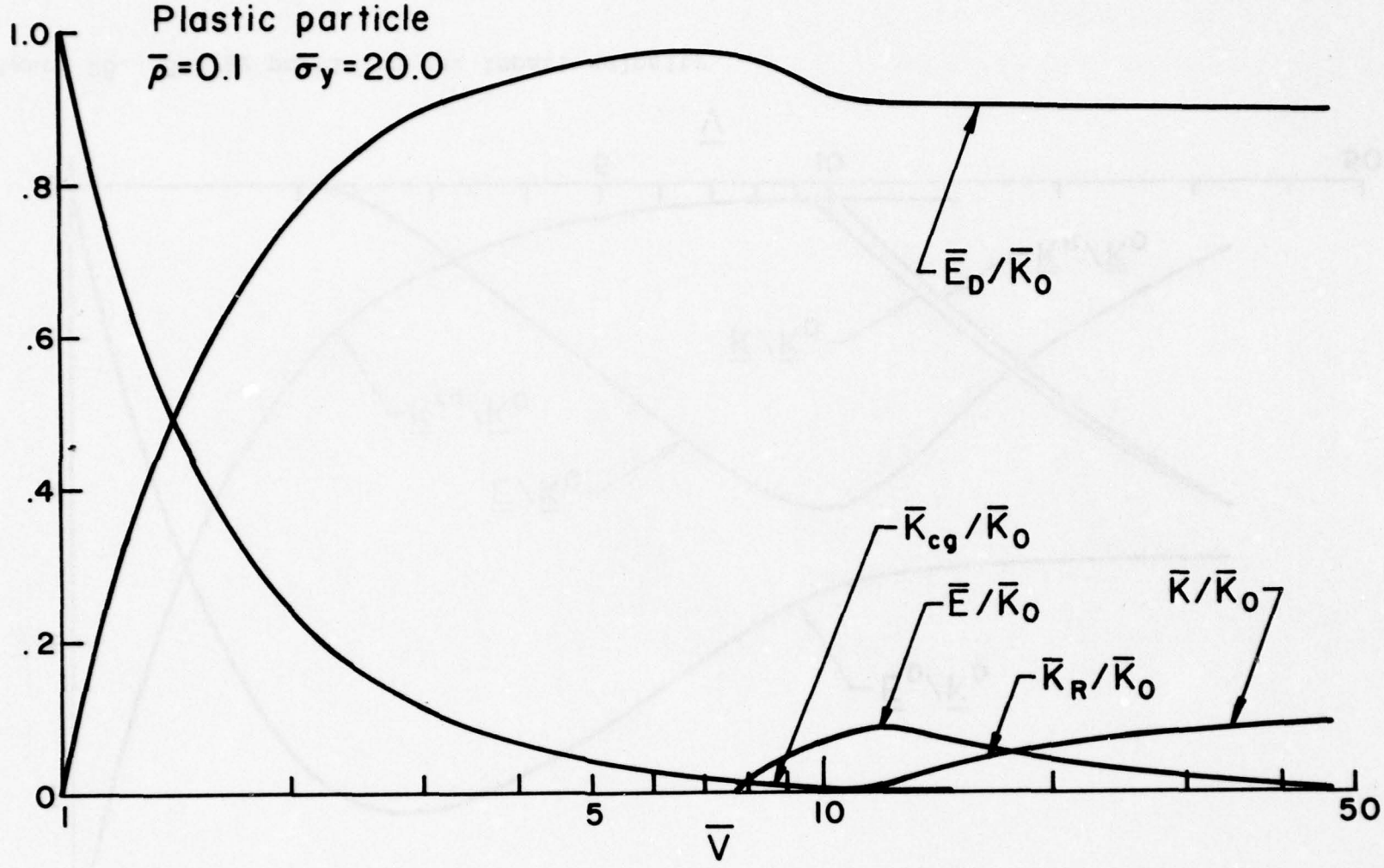

Figure 27. Energy partition vs. impact velocity

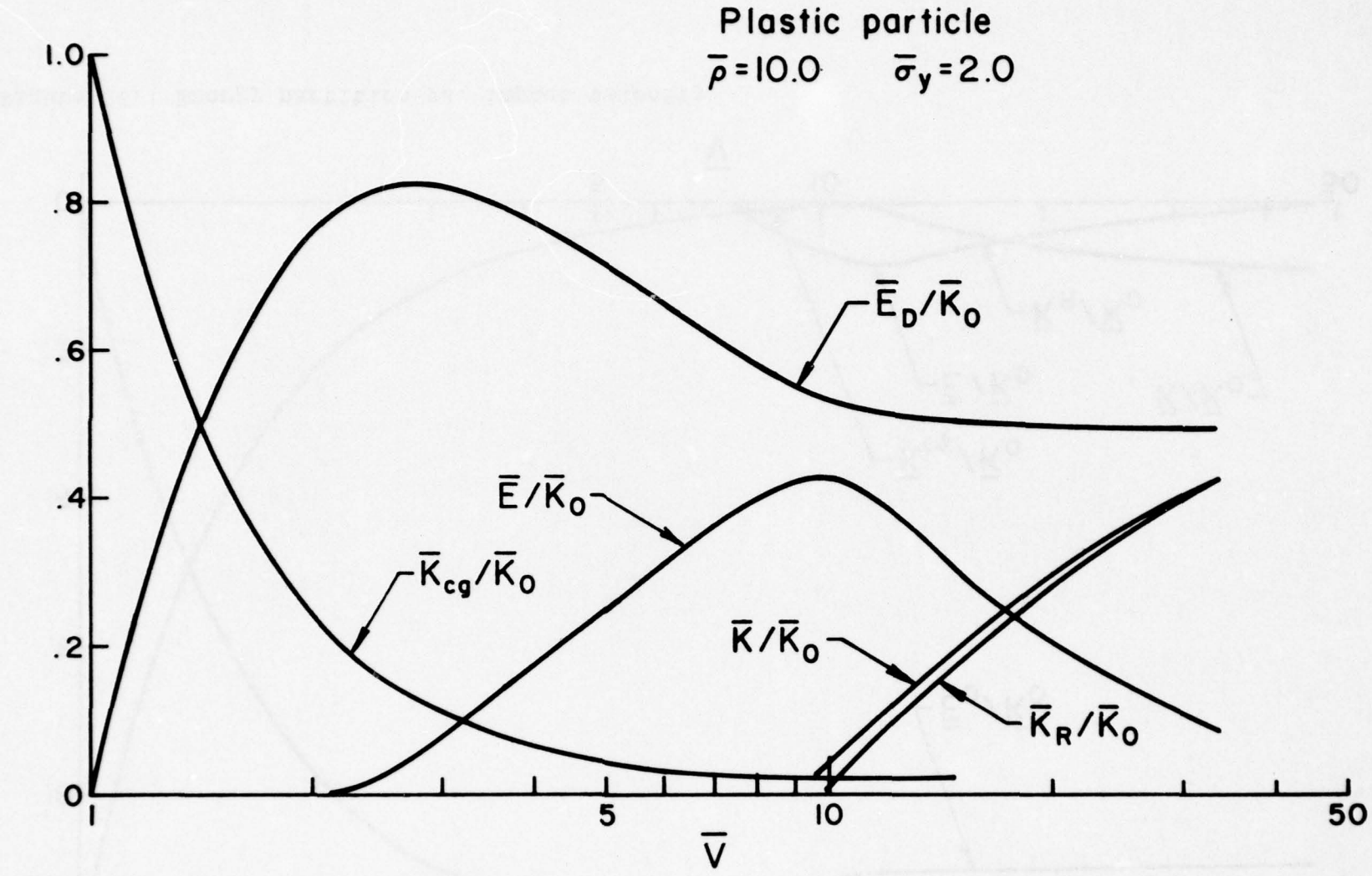

Figure 28. Energy partition vs. impact velocity

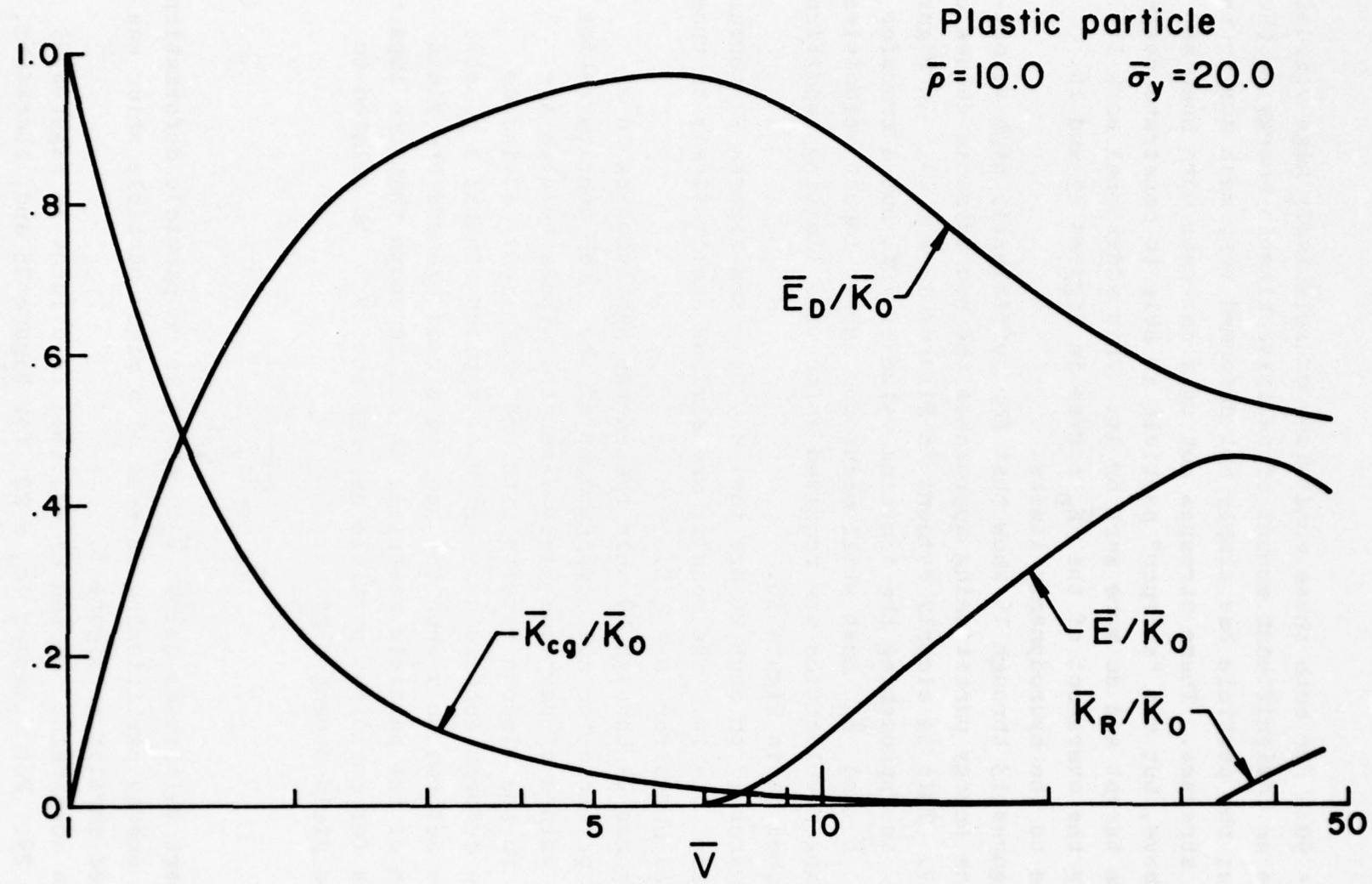

Figure 29. Energy partition vs. impact velocity

for $\bar{V} = 50$. For both these conditions of relatively high viscosity, there is an insignificant amount of relative kinetic energy in the particle; the particle has simply not deformed very much due to the viscous stresses. These stresses not only generate more heat as noted above, but the "sharper" particle is able to penetrate deeper into the target and do more work on it. This additional work is shown by the overshoot of the $\bar{E}_D$ curves in Figures 15 and 16 relative to the hydrodynamic limits.

Figures 13 through 16 show that for sufficiently high velocities, the energy partitioning approaches the hydrodynamic values of Figure 9. This is clearly evident in Figures 13 and 14. In Figure 15, $\bar{E}_D$ is approaching the limiting value of 70%, but a transfer between $\bar{E}$ and $\bar{K}_R$ must still occur for larger impact velocities. Still larger velocities are required before the limiting conditions are reached as in Figure 16.

Figures 17 through 20 are for $\bar{\rho} = 0.1$ and Figures 21 through 23 are for $\bar{\rho} = 10$. The results are similar qualitatively to those described above for $\bar{\rho} = 1.0$.

Figures 24 through 29 show the energy partitioning in a plastic particle for all combinations of the three density ratios and two values of particle yield strength. These results are similar to the viscous results with one exception. A viscous particle deforms continuously under an applied stress; a plastic particle deforms only when the applied stress exceeds the yield strength of the particle material. It can be shown that the impact velocity for incipient particle deformation ($\bar{V}_y$) is related to particle yield strength by

$$\bar{V}_y = \sqrt{2\bar{\sigma}_y} \tag{37}$$

For impact velocities below $\bar{V}_y$, there is no particle deformation, and the energy partitioning is that of a rigid particle which was described earlier in Figure 7.

The constraint imposed by Eq. (37) is evident in Figures 24 through 29. For example, $\bar{\sigma}_y = 20$ for Figure 25 and, therefore,

$\bar{V}_y = 6.3$. In the interval $1.0 \leq \bar{V} \leq 6.3$, Figure 25 is a replica of Figure 7. Due to its rigidity, the particle does more work on the target than a deforming particle as evidenced by the overshoot of the $\bar{E}_D$ curve. As the impact velocity increases above $\bar{V}_y$, the particle yields. It does less work on the target as larger percentages of the energy are expended laterally and dissipated internally. Eventually, for high enough impact velocities, the particle strength is insignificant, and the energy partitioning again approaches the hydrodynamic values.

B. Particle Shape

Figures 30, 31, and 32 show particle width at the end of impact as a function of impact velocity and particle viscosity for three values of density ratio. The most striking feature of these curves is the (apparent) transition of behavior between low and high velocity impacts. The transition, which is most apparent for $\bar{\rho} = 1$ and 10 and for small values of $\bar{\mu}$, corresponds to the stiffening of the particle which was discussed in Section III.A. It is also interesting that the sharpness of the transition is blunted by increasing viscosity.

With the exception of impact velocities below the transition velocity, the hydrodynamic solution provides an upper limit for the lateral growth of the particle. At large impact velocities (depending on the value of $\bar{\mu}$), the width of each particle approaches the hydrodynamic limit closely.

Figures 30 through 32 show that for a given particle density and impact velocity, viscosity has a larger effect on particle shape as the target density increases. For example, for $\bar{\mu} = 1$ and $\bar{V} = 10$, the width of the particle is within 15% of the hydrodynamic value when $\bar{\rho} = 0.1$, but the width is less than half the hydrodynamic value when $\bar{\rho} = 10$. The implications of the result as regards mass erosion are noted later.

Figures 33, 34, and 35 show an analogous set of particle width curves for plastic particles. These curves exhibit the same trends as do Figures 30 through 32 for viscous particles - with

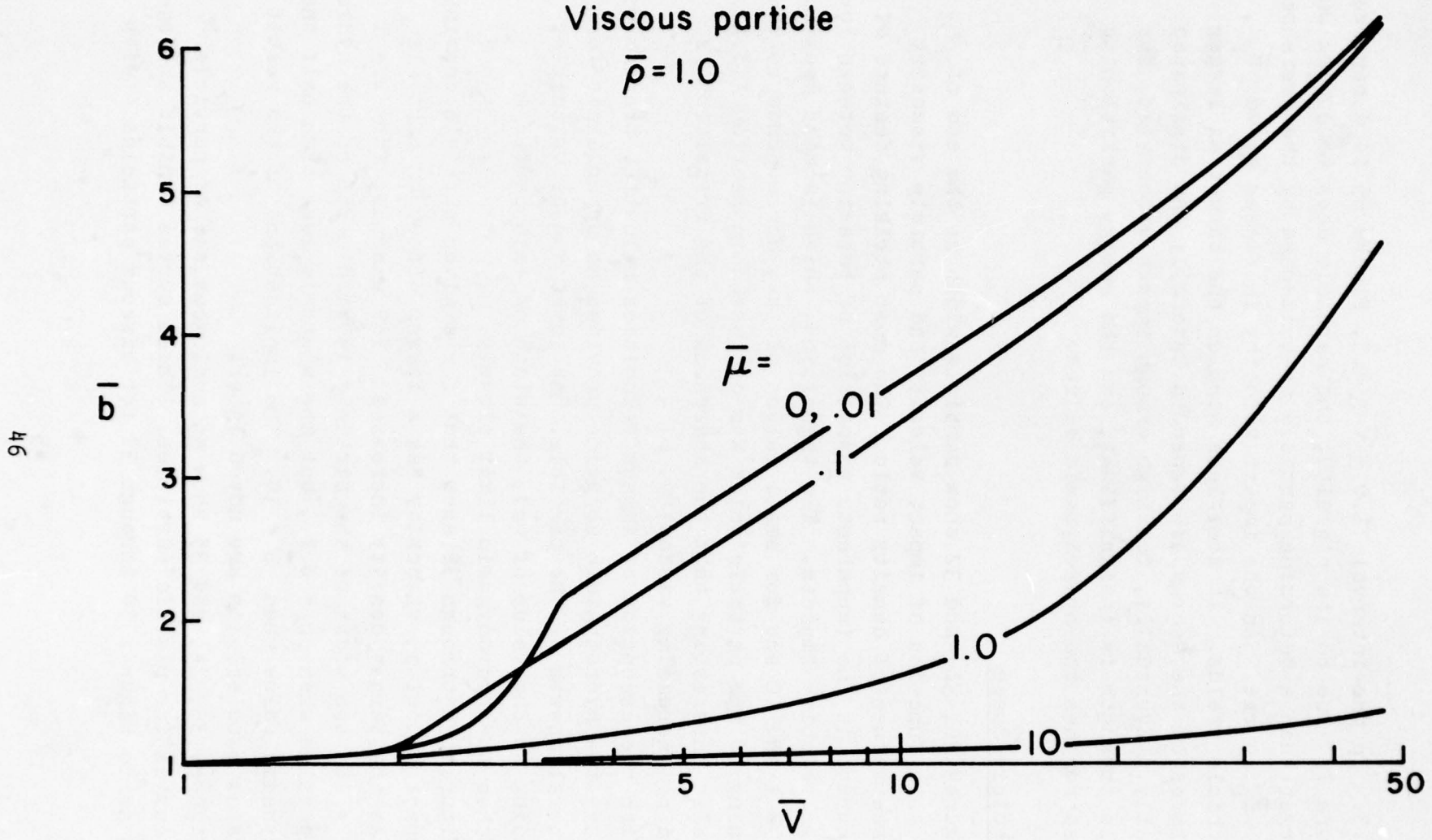

Figure 30. Particle width vs. impact velocity

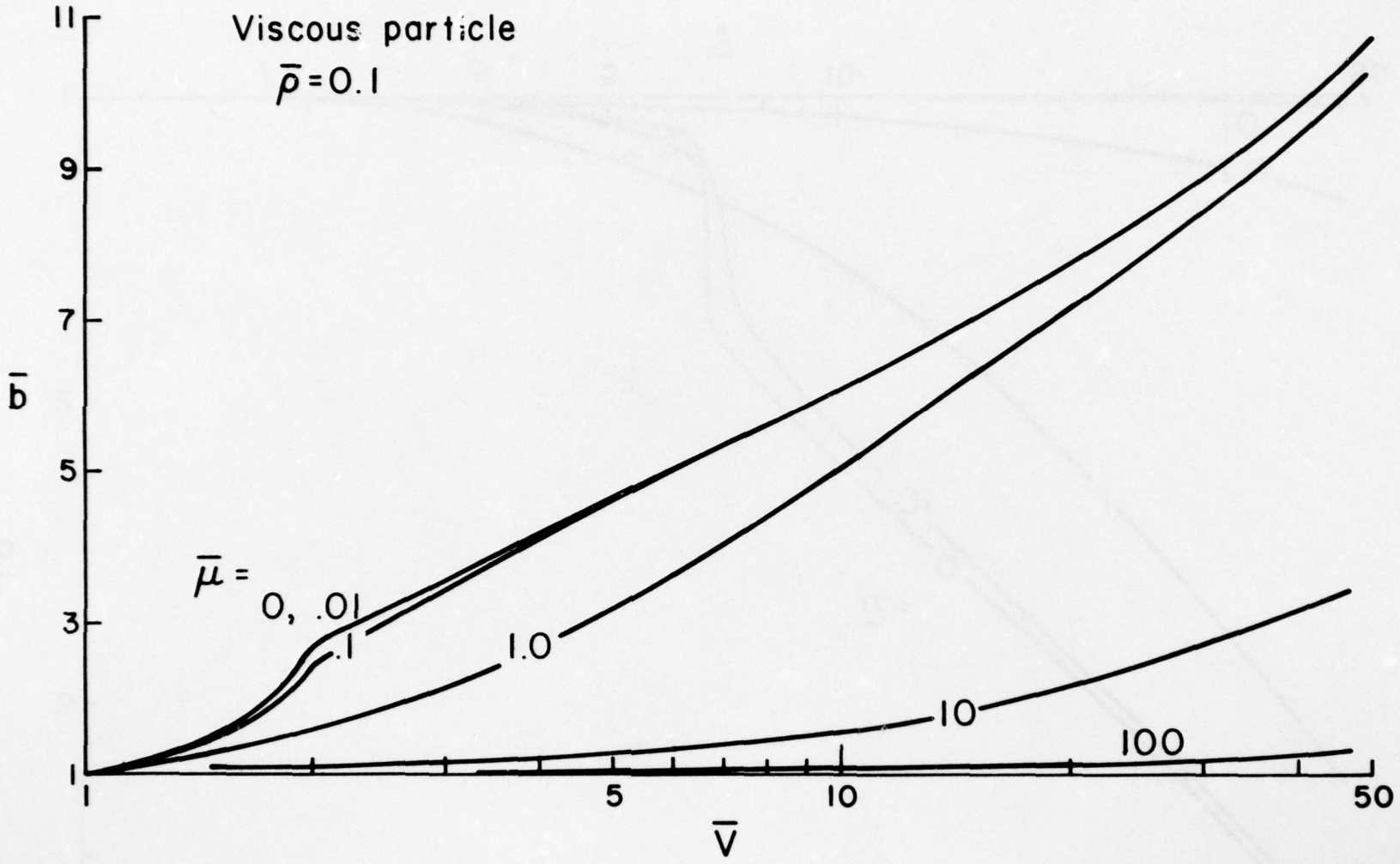

Figure 31. Particle width vs. impact velocity

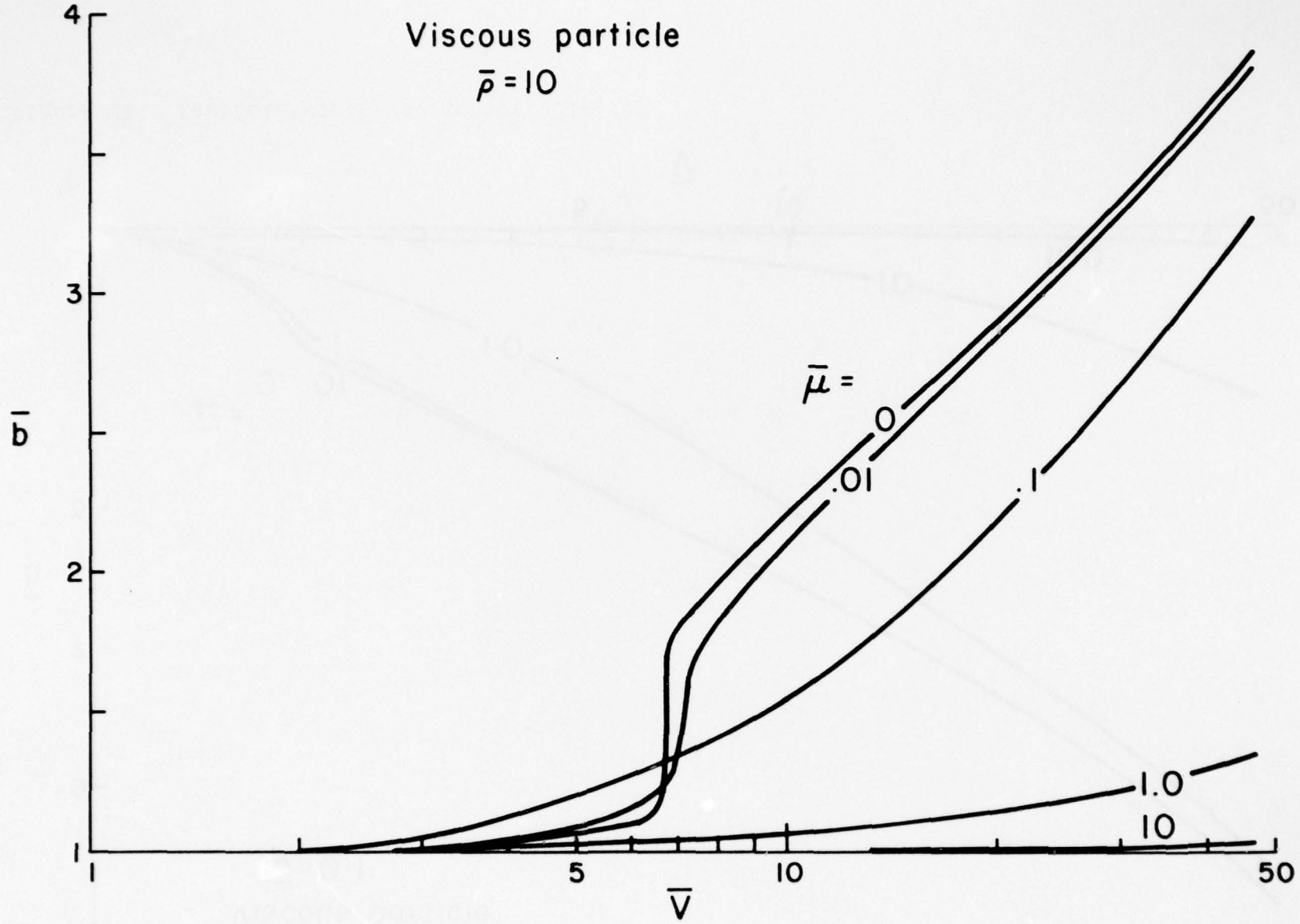

Figure 32. Particle width vs. impact velocity

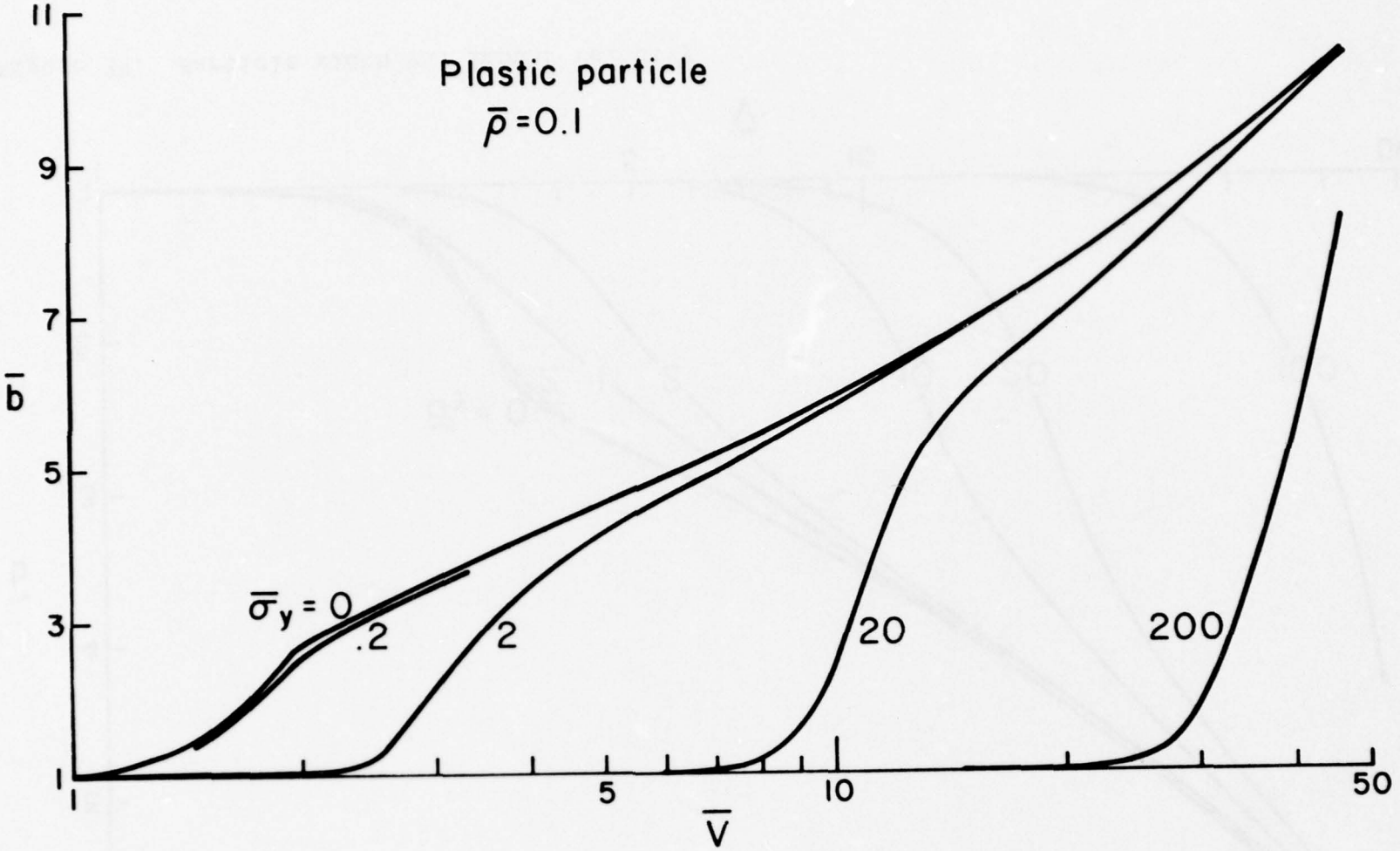

Figure 33. Particle width vs. impact velocity

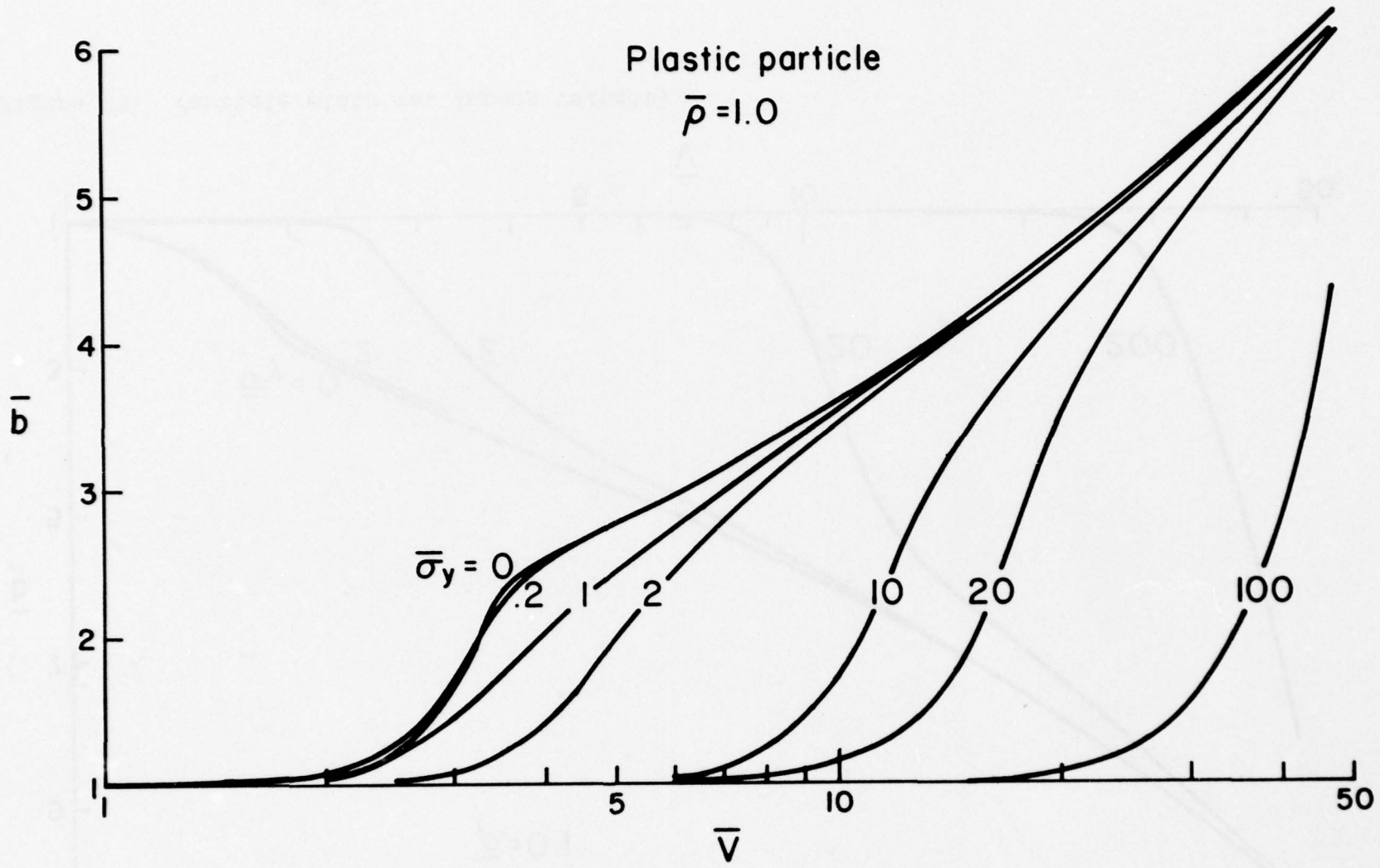

Figure 34. Particle width vs. impact velocity

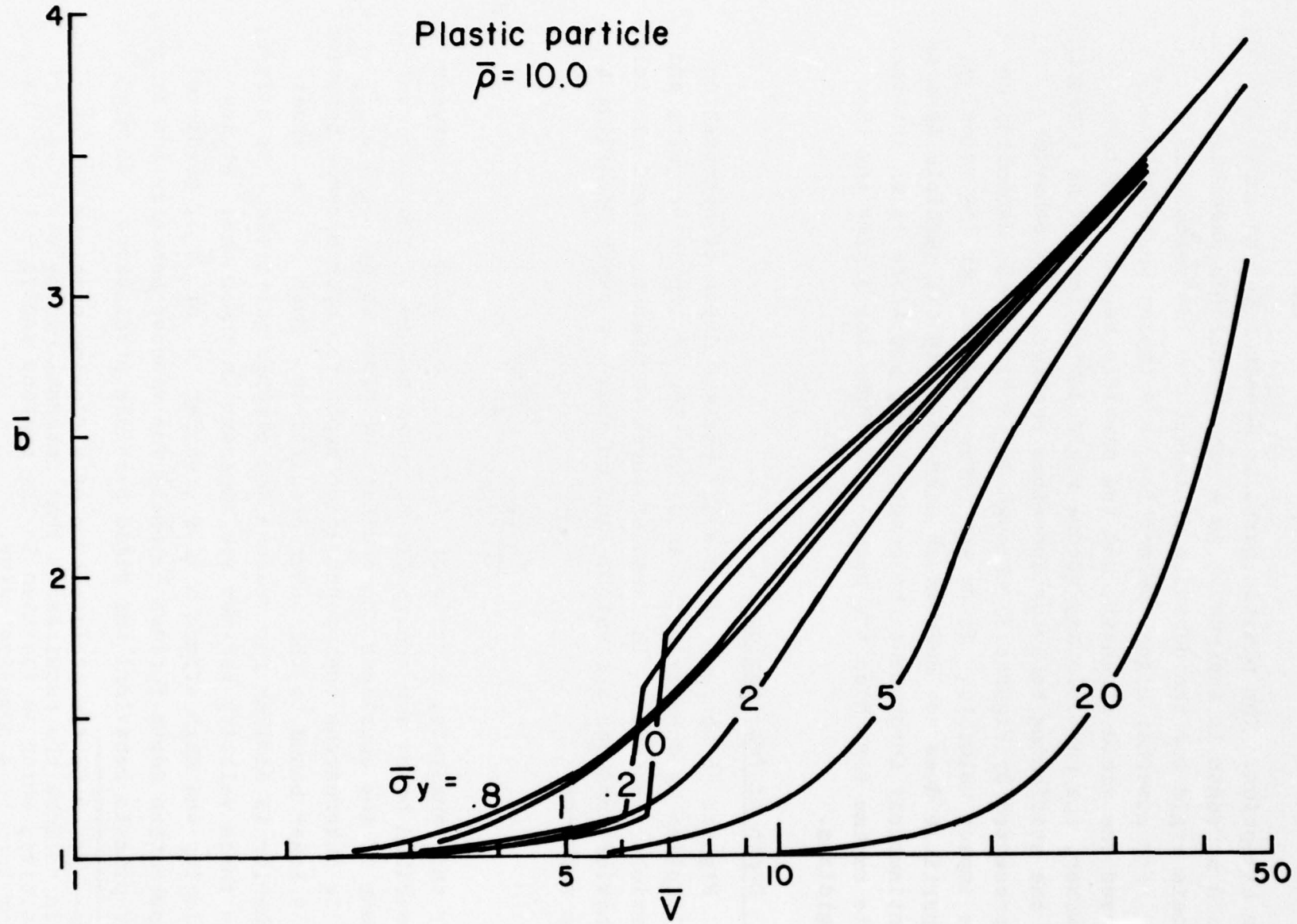

Figure 35. Particle width vs. impact velocity

one exception. The plastic particle does not deform until its yield strength is exceeded. As a result, plastic particles remain rigid for the duration of impact for low velocities.

For somewhat higher velocities, the impact pressure does exceed the yield strength, and the particle begins to deform. However, the particle may become rigid during impact* as a result of the stiffening behavior described earlier. The behavior represented by Figures 33 through 35 is different, depending on the impact velocity. There are three regimes. At low velocity, a particle does not deform; at high velocity the particle deforms continuously throughout the penetration; and there is an intermediate regime for which the particle deforms for a time and then rigidizes.

C. Depth of Penetration

Figures 36 through 41 show the maximum depth of penetration multiplied by density ratio as a function of impact velocity and particle viscosity. In terms of these parameters, rigid particle behavior produces a straight line on semi-log paper according to the relation

$$\frac{C_D}{2} \bar{\rho}\bar{y}_{max} = \ell n \, \bar{V} \qquad (38)$$

For this analysis, a value of $C_D/2 = 1$ was used. The results described below are applicable to other values of the drag coefficient if one considers the ordinate of plots to be $C_D/2 \; \bar{\rho}\bar{y}_{max}$. It is interesting that penetration depth for hydrodynamic behavior is a lower bound to the other predictions. Much of the impact behavior is similar for viscous and plastic particles. As before, the three velocity regimes are apparent in the plots. At low velocity and high strength (i.e., either $\bar{\mu}$ or $\bar{\sigma}_y$), predicted penetration depth follows (closely for viscous behavior and exactly for plastic behavior) the rigid particle predictions. At high

*The criterion for rigidization of a flowing particle is $(-\bar{\xi}) = 0$. This follows the requirement that internal energy production be positive, which is violated in the present analysis if $(-\bar{\xi})$ passes from zero to a negative value.

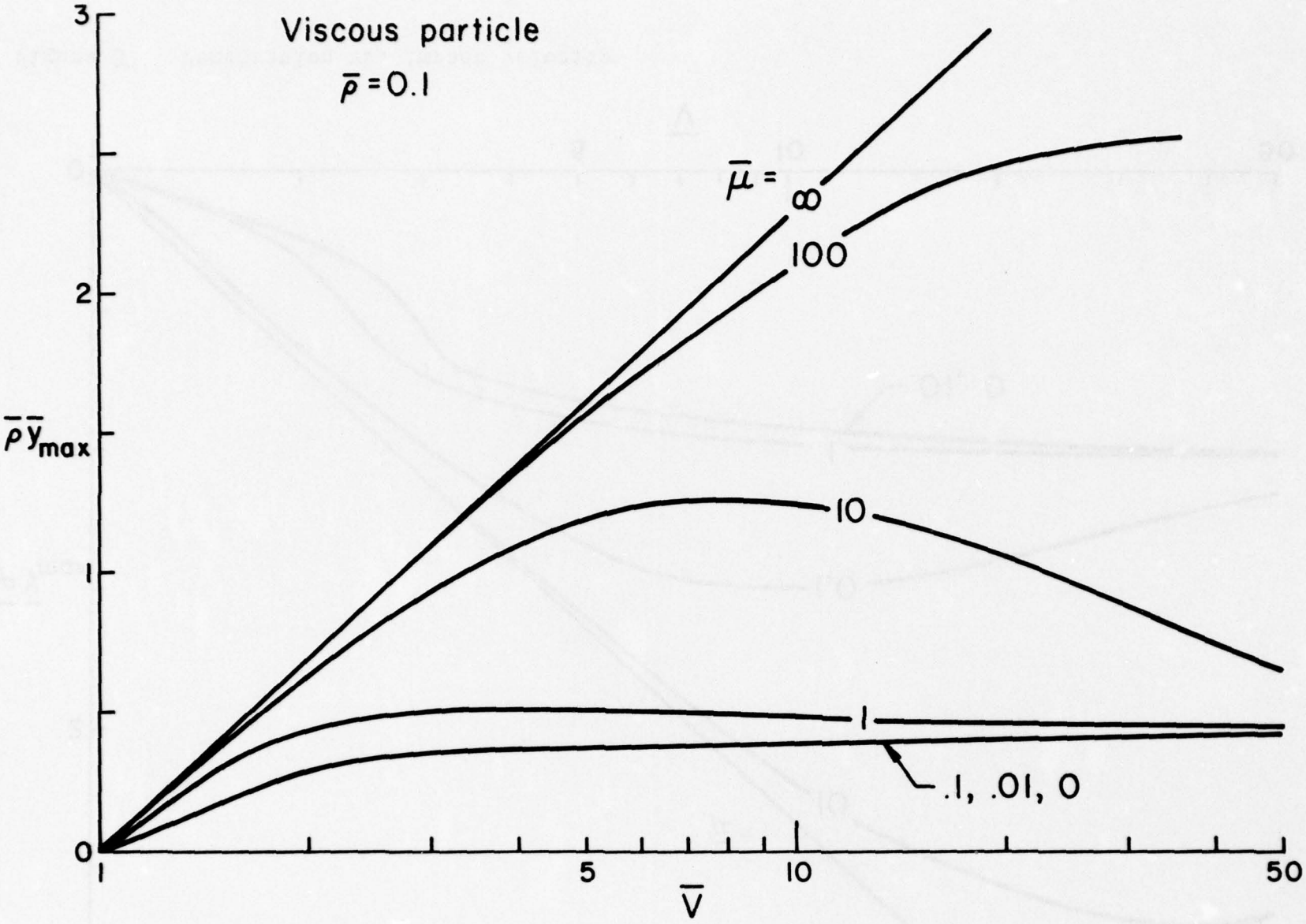

Figure 36. Penetration vs. impact velocity

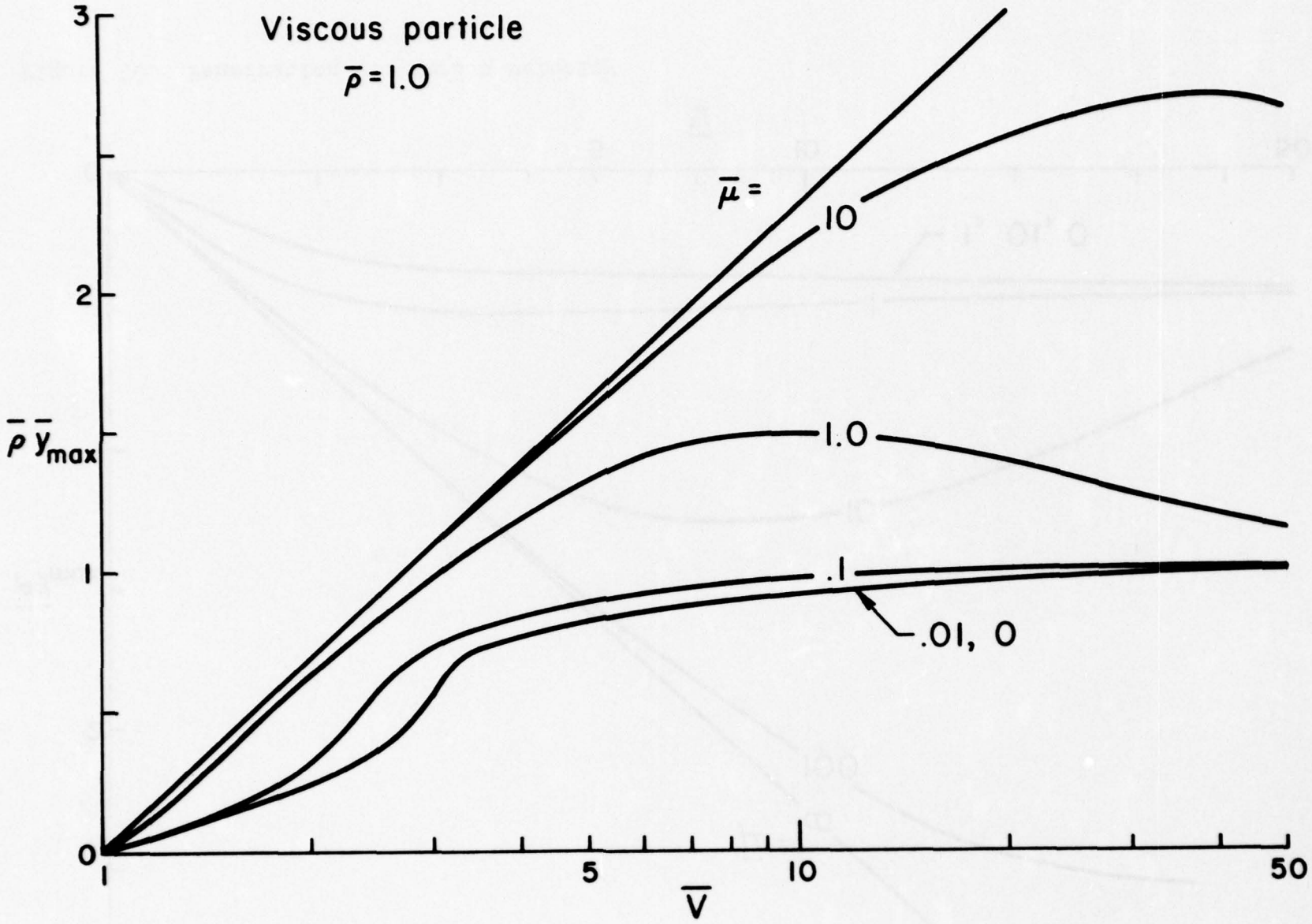

Figure 37. Penetration vs. impact velocity

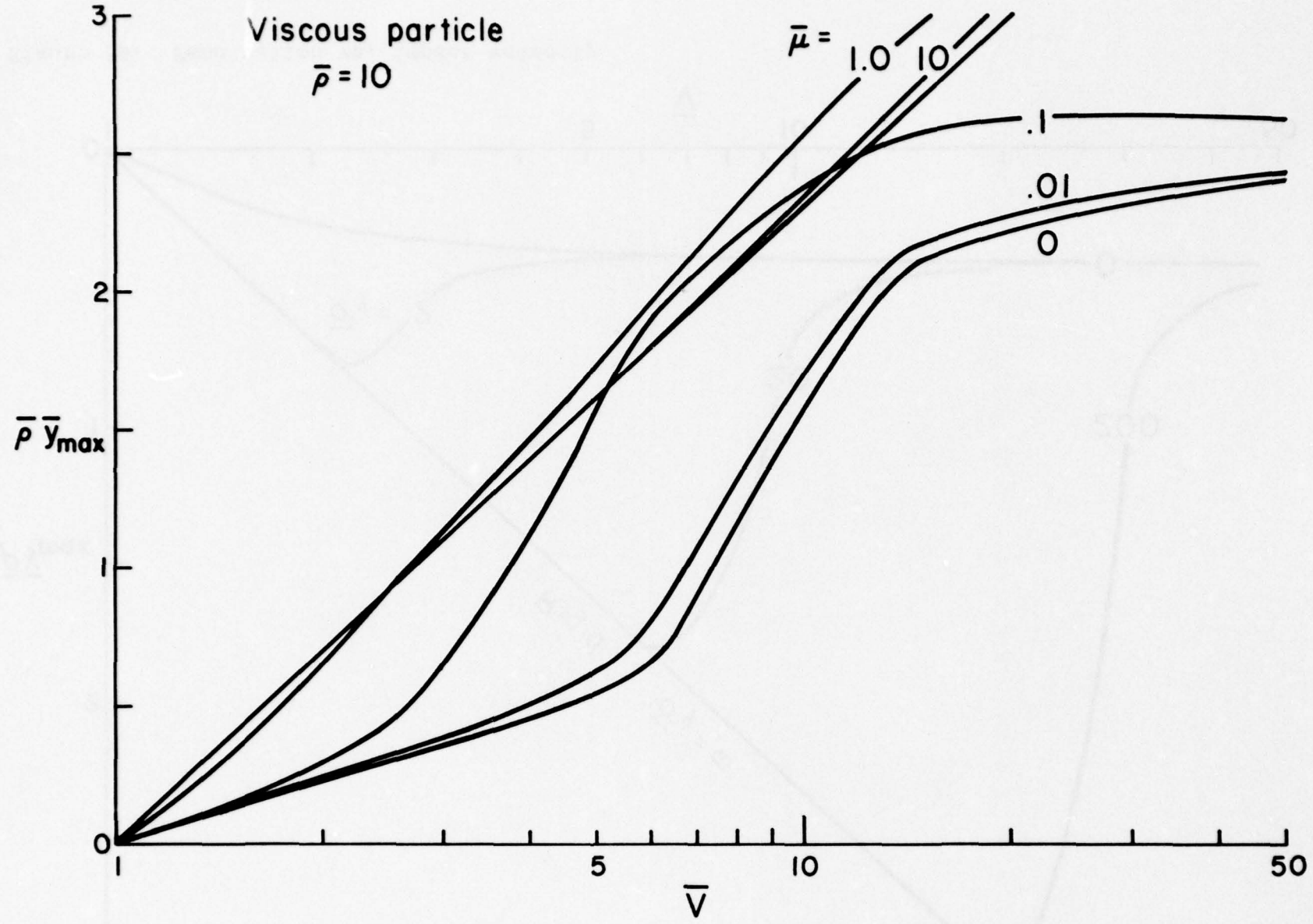

Figure 38. Penetration vs. impact velocity

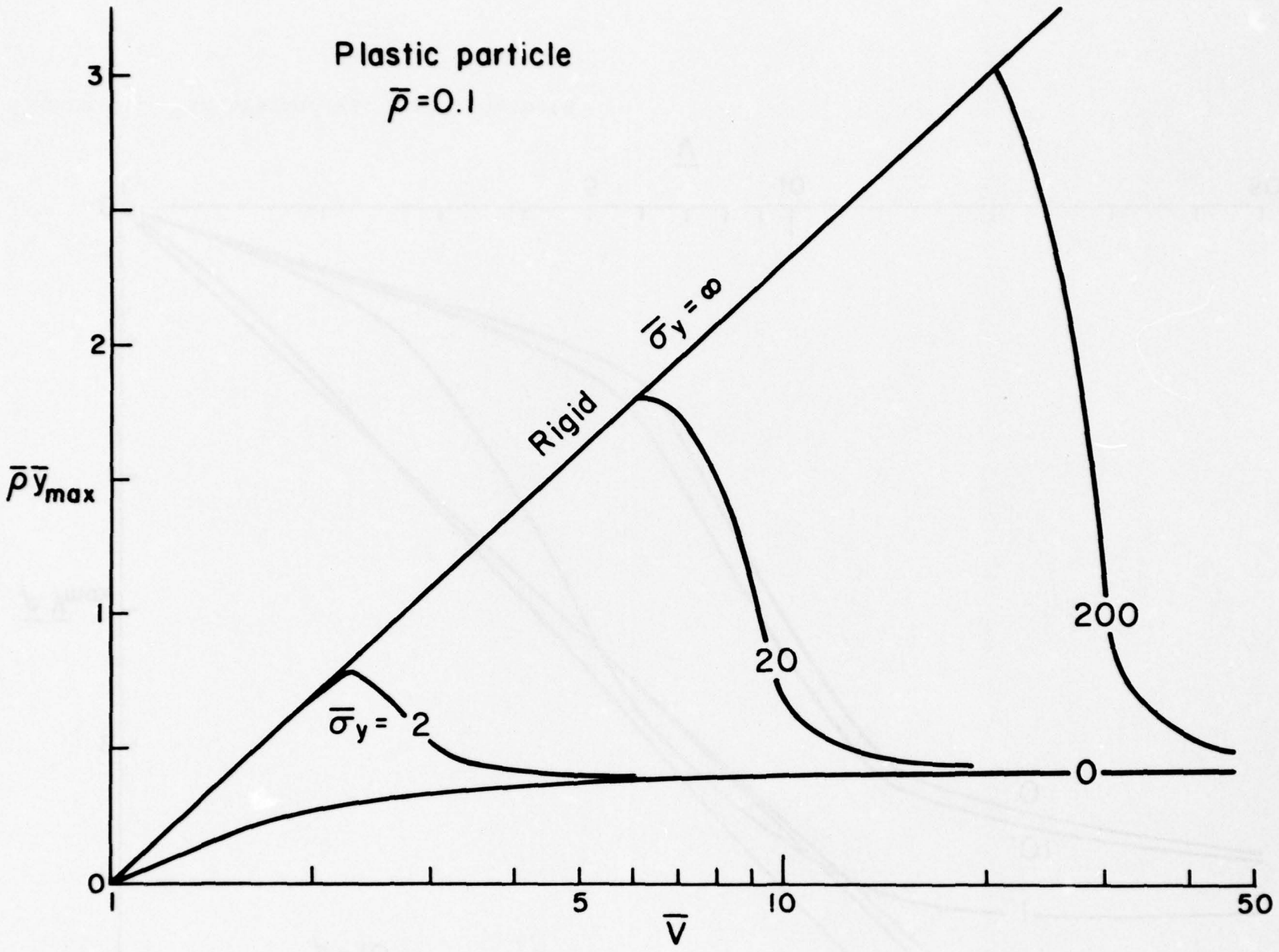

Figure 39. Penetration vs. impact velocity

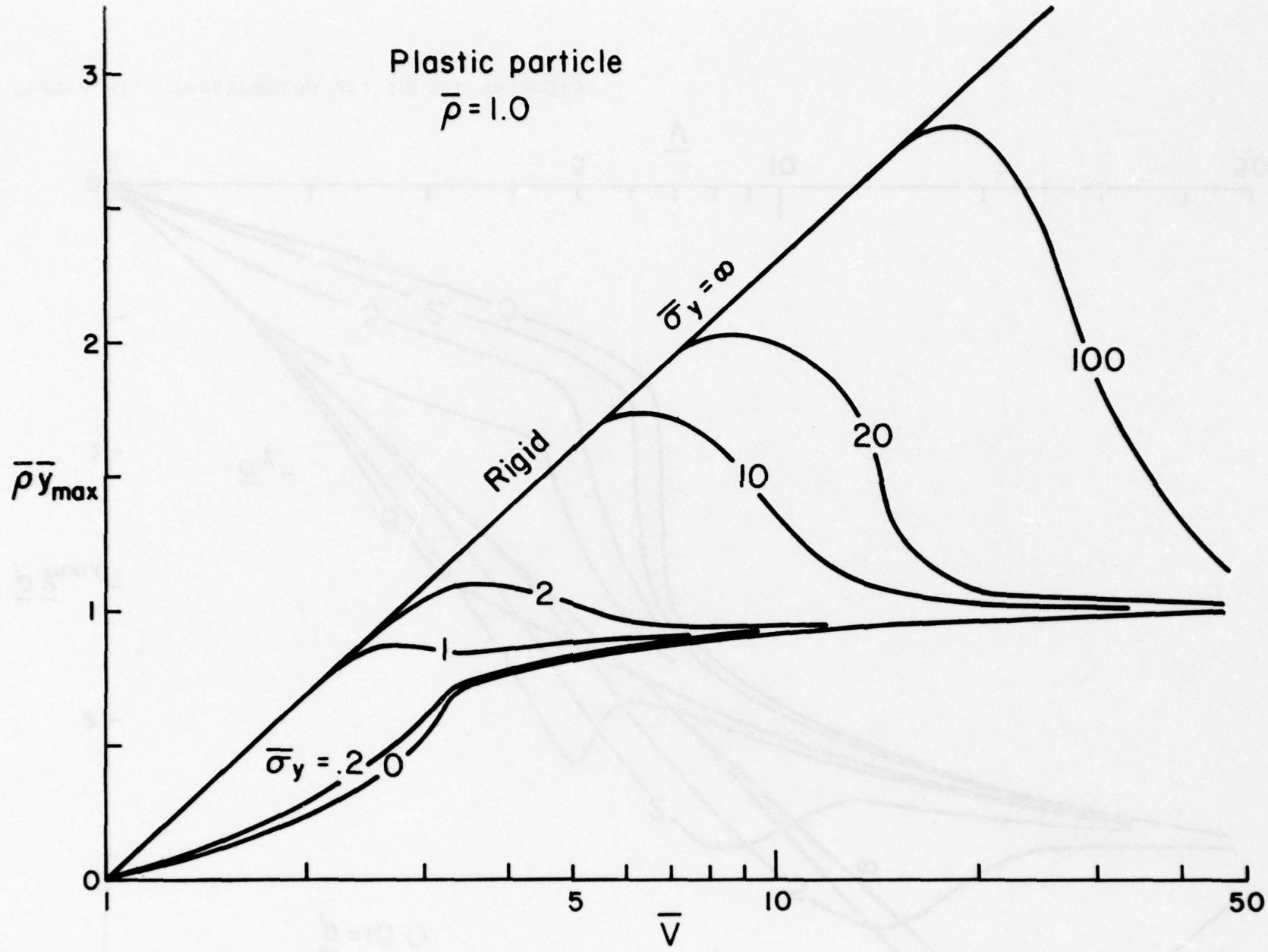

Figure 40. Penetration vs. impact velocity

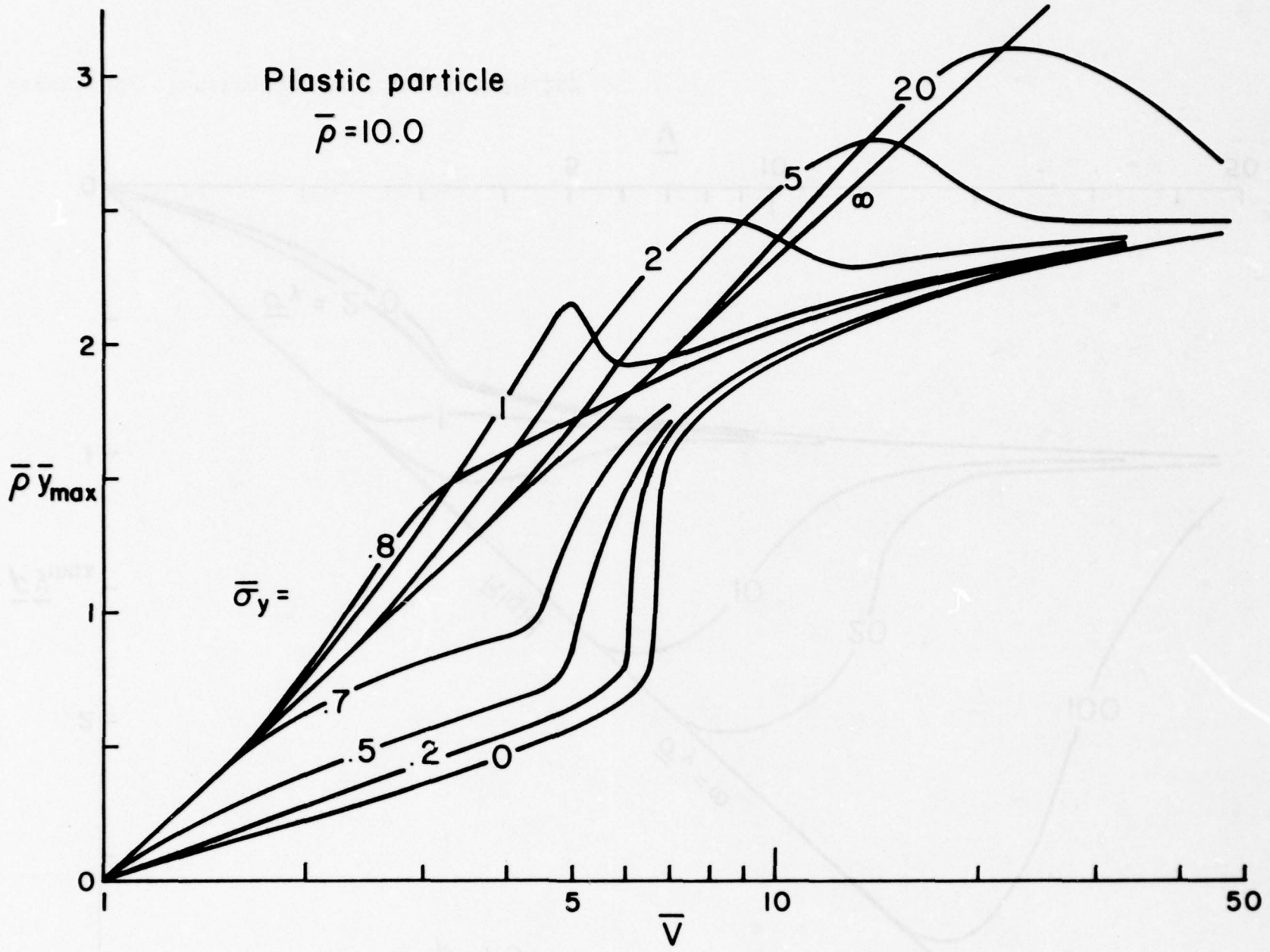

Figure 41. Penetration vs. impact velocity

velocity, predicted penetration depth approaches closely the hydrodynamic particle predictions. The transition from the rigid to the hydrodynamic limits occurs at intermediate impact velocity. The nature of viscosity is such that the abruptness of the transition exhibited by hydrodynamic behavior is blunted for larger $\bar{\mu}$. Higher $\bar{\sigma}_y$ for plastic behavior tends to blunt the same abruptness, but the nature of plasticity also introduces an abruptness of its own into the graphs.

A very interesting phenomenon is exposed by Figures 38 and 41. Depth of penetration for $\bar{\rho} \leq 1$ is bounded from above by rigid particle predictions. But this is not the situation when the particle is less dense than the target (i.e., $\bar{\rho} > 1$). Penetrations as much as 35% greater are predicted, and the impact velocity at which the peak occurs depends on the value of $\bar{\mu}$ or $\bar{\sigma}_y$. Also, a particle of greater strength may penetrate less than one of lesser strength. Furthermore, increasing the impact velocity of a given particle design may result in lower penetration. All of these characteristics are somewhat surprising and motivate further discussion of the underlying phenomenon.

In the context of the present theory, the depth of penetration is the time integral of the front face velocity. So if $\bar{V}_\perp$ is plotted as a function of τ for a given impact, then the area under the curve is numerically equal to the depth of penetration. Detailed studies of individual cases show that the $\bar{V}_\perp$ history, hence also the depth, is very sensitive to the particle deformation history which, in turn, is controlled by strength.

The abruptness of the transition for $\bar{\rho} = 10$ and hydrodynamic behavior may be viewed further in terms of the $\bar{V}_\perp - \tau$ traces. Traces for three values of impact velocity are shown by Figure 42. Note that for $\bar{V}_\perp < 6$, the front face velocity decreases rapidly to 1 and ceases penetration. But at $\bar{V}_\perp = 7$, the trace becomes flat at a value in excess of 1, and the penetration persists a longer time. The depth of penetration (i.e., the area under the trace) takes a sudden jump at $\bar{V}_\perp = 7$. That the front face deceleration ceases or even reverses seems at first inconsistent with

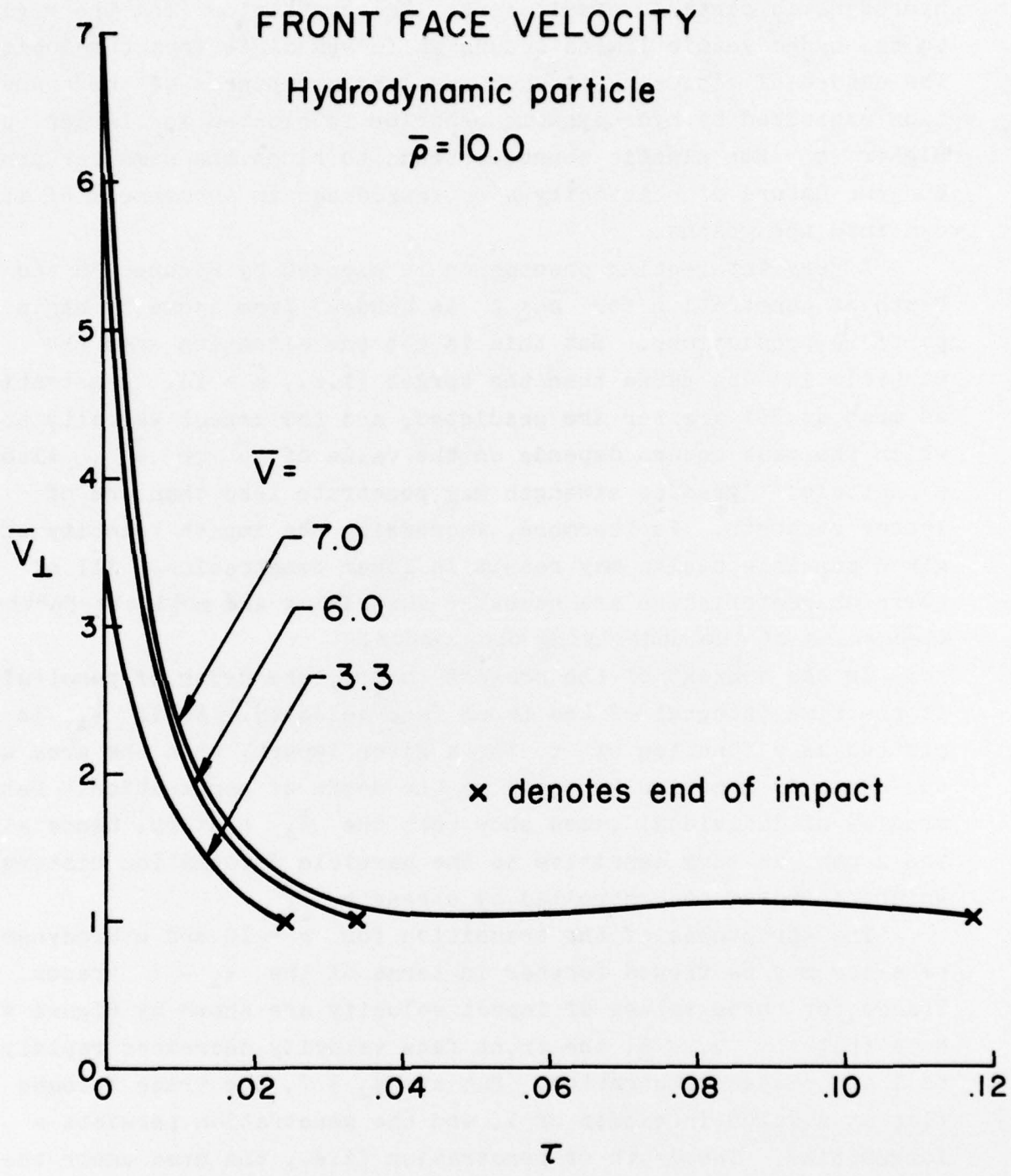
FRONT FACE VELOCITY
Hydrodynamic particle
$\bar{\rho} = 10.0$
$\bar{V}_\perp$
$\bar{V}$ =
7.0
6.0
3.3
× denotes end of impact
τ
0
1
2
3
4
5
6
7
.02
.04
.06
.08
.10
.12

Figure 42.

conservation principles. Several cases have been checked and no inconsistencies were found. For example, Figure 43 demonstrates that the mass center velocity decreases monotonically with time even though the front face may speed up.

D. Target Erosion

The coupled effects of energy partitioning, particle deformation, and depth of penetration yield the target-mass erosion curves shown in Figures 44, 45, and 46 for viscous particles and in Figures 47, 48, and 49 for plastic particles. The ordinate of each figure, which is denoted by $\bar{m}$, represents the ratio of target mass loss to particle mass. A cursory glance at these figures reveals the strong influence of particle viscosity (or yield strength) on target erosion.

Before examining these results in detail, it should be noted that the details of the erosion process are the weakest link in the integral theory at this time. In part this is due to a paucity of the type of detailed data needed to develop a general model. But just as important is the fact that most of the early effort in the development of this theory has been devoted to the prediction of penetration and particle deformation. The theory has now reached the stage where effort toward cavity predictions is warranted, and an improved theory of mass loss is under development at present. Mass loss predictions using the present theory are compared to experimental observations to gain insight into how to improve the theory.

A comparison of Figures 44 through 49 shows certain common trends. First, erosion varies inversely as the density ratio; the heavier particle produces the most damage, all other conditions unchanged. Second, erosion increases with viscosity (or yield strength) for low impact velocities although the amount of mass removed is extremely small. In contrast, erosion varies inversely as viscosity for high impact velocities; the hydrodynamic value is the upper limit for target erosion.

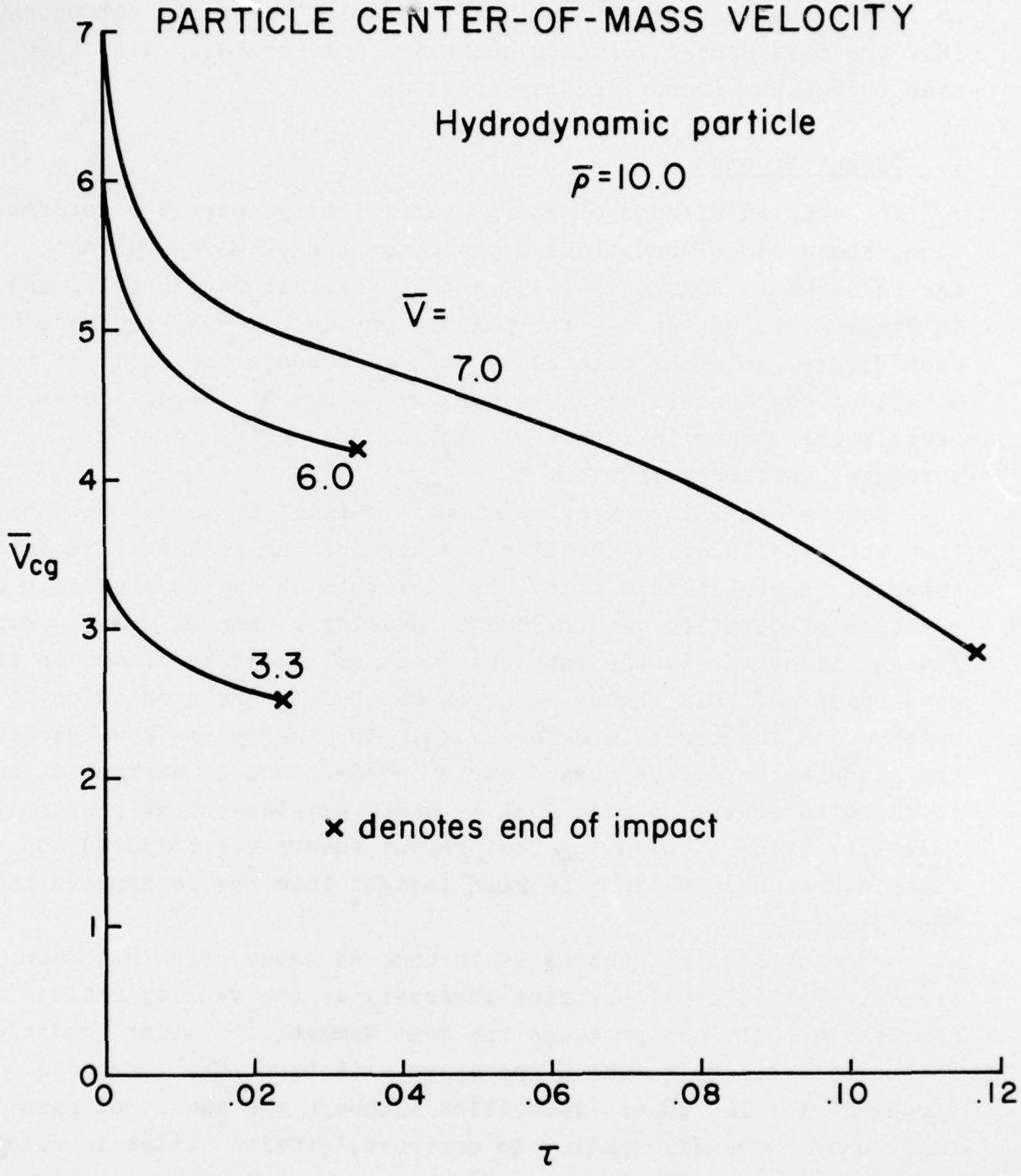
PARTICLE CENTER-OF-MASS VELOCITY
Hydrodynamic particle
$\bar{\rho}$=10.0
$\bar{V}$=
7.0
6.0
3.3
× denotes end of impact
$\bar{V}_{cg}$
τ
0
1
2
3
4
5
6
7
.02
.04
.06
.08
.10
.12

Figure 43.

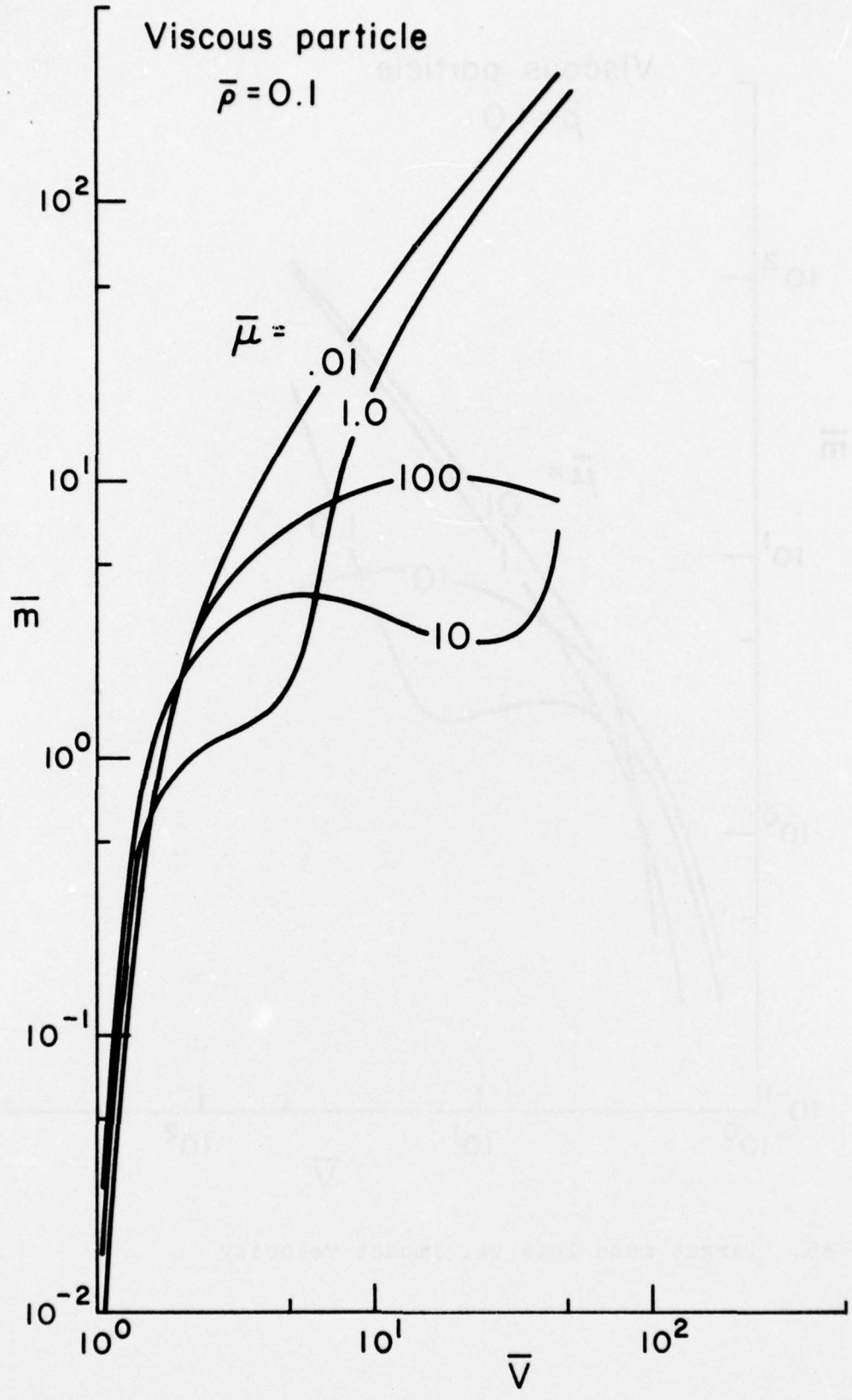

Figure 44. Target mass loss vs. impact velocity

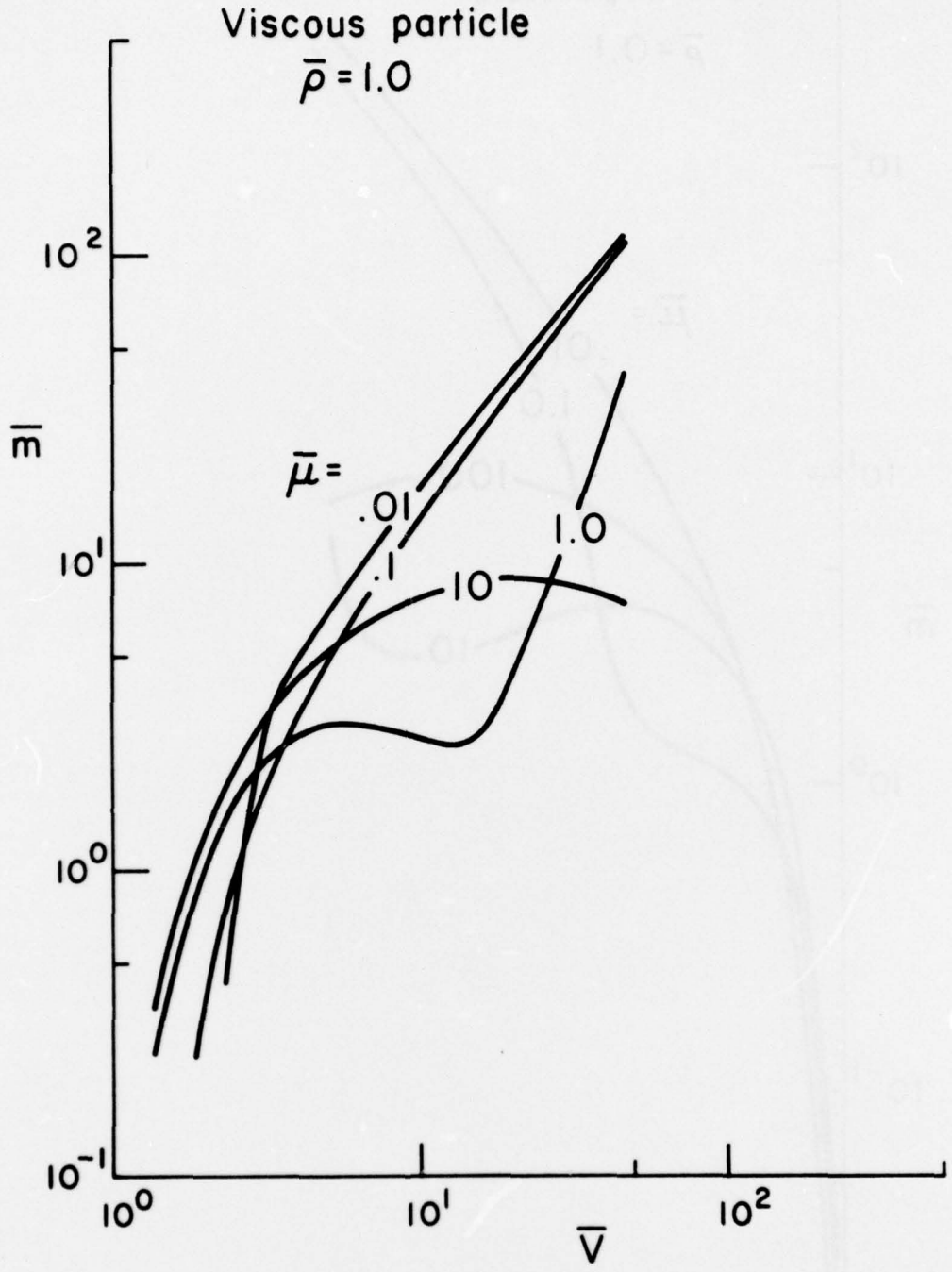

Figure 45. Target mass loss vs. impact velocity

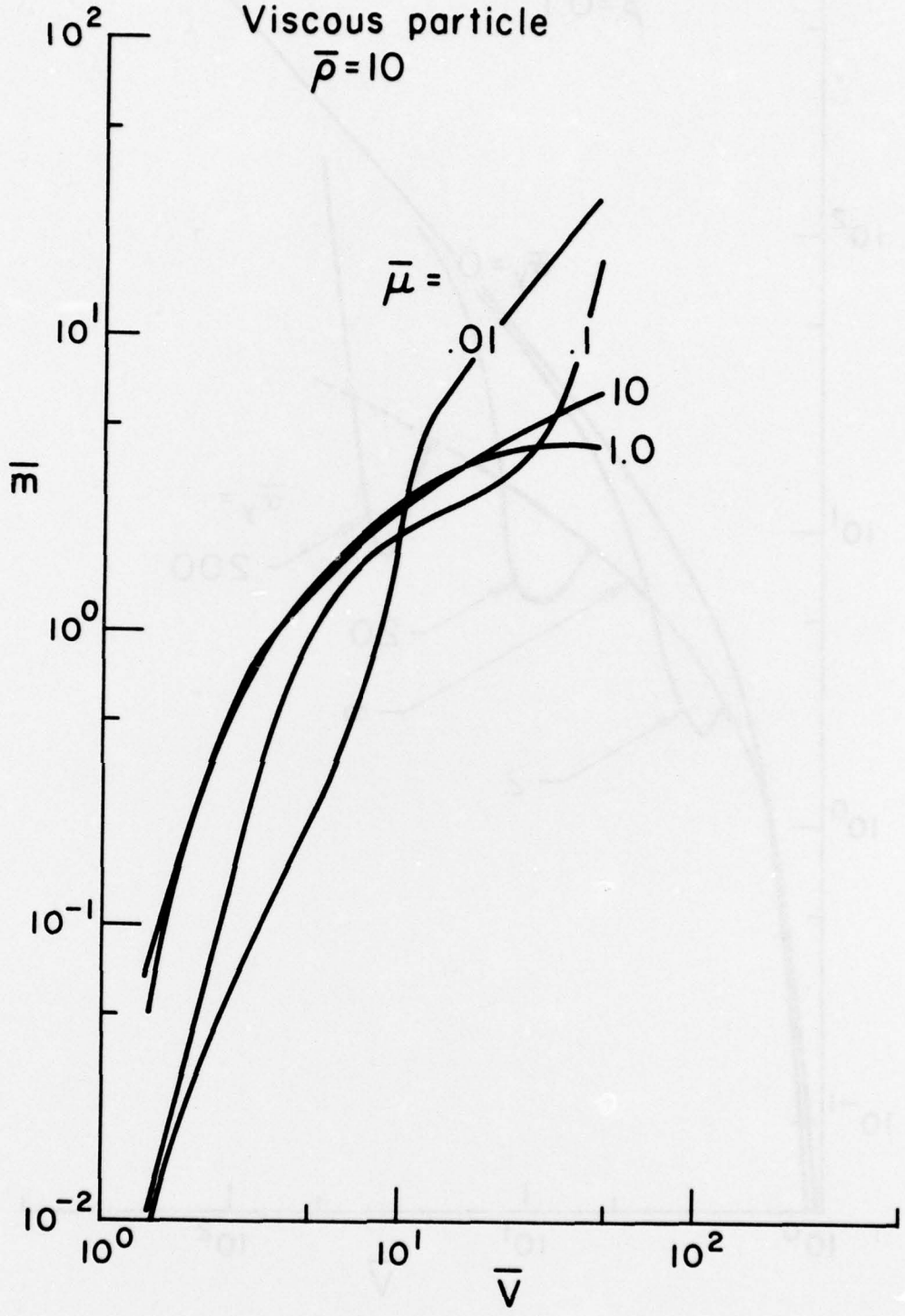

Figure 46. Target mass loss vs. impact velocity

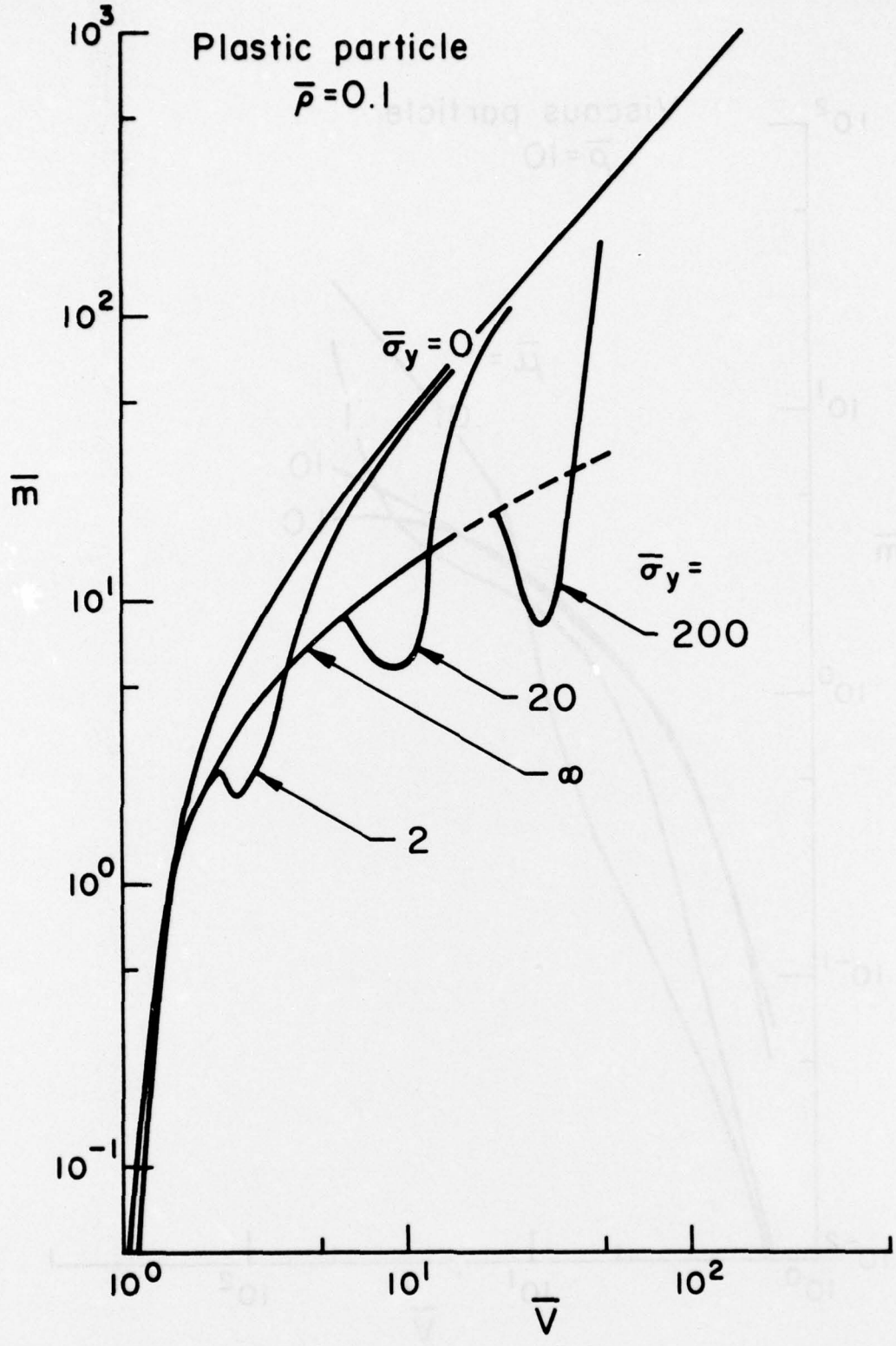

Figure 47. Target mass loss vs. impact velocity

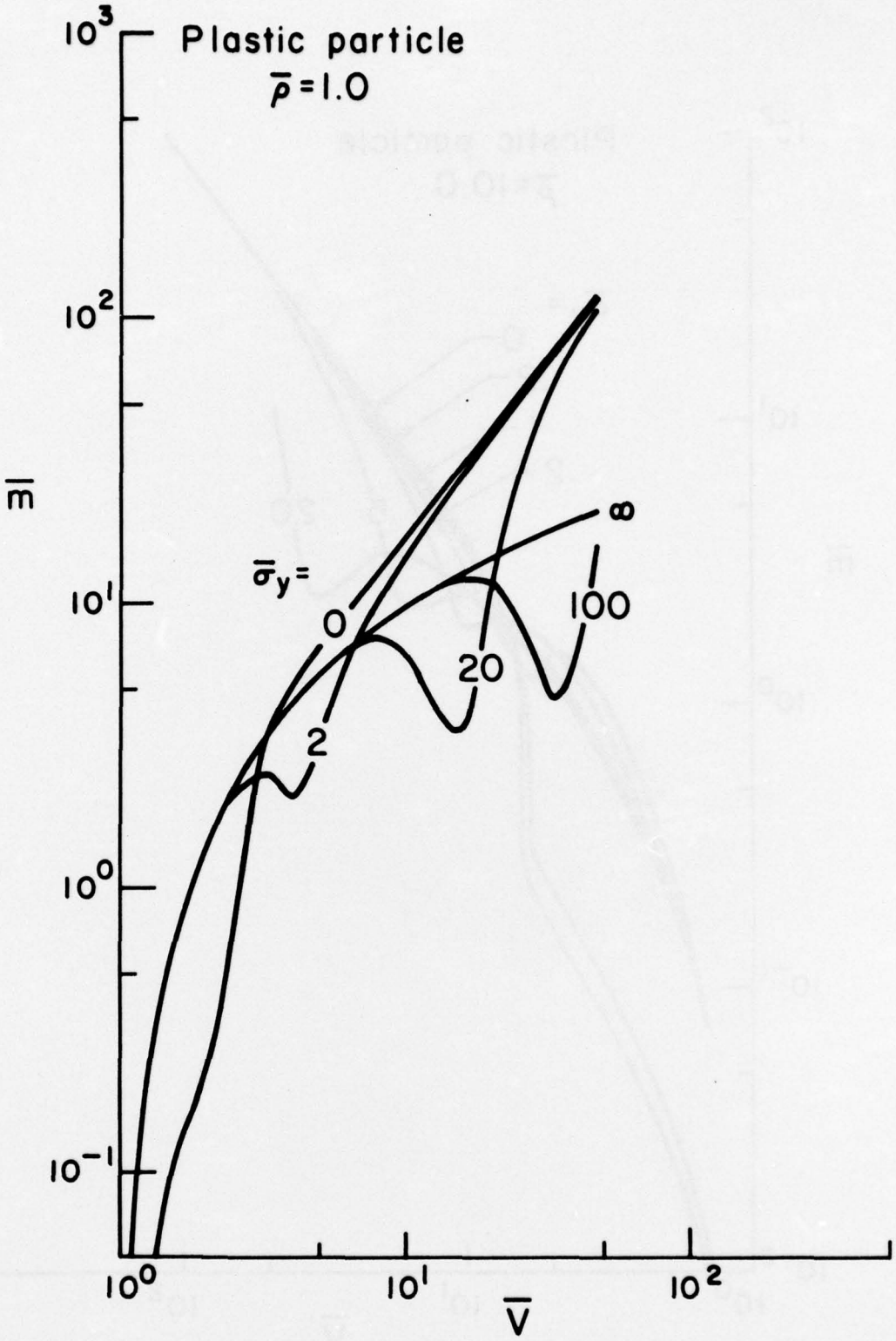

Figure 48. Target mass loss vs. impact velocity

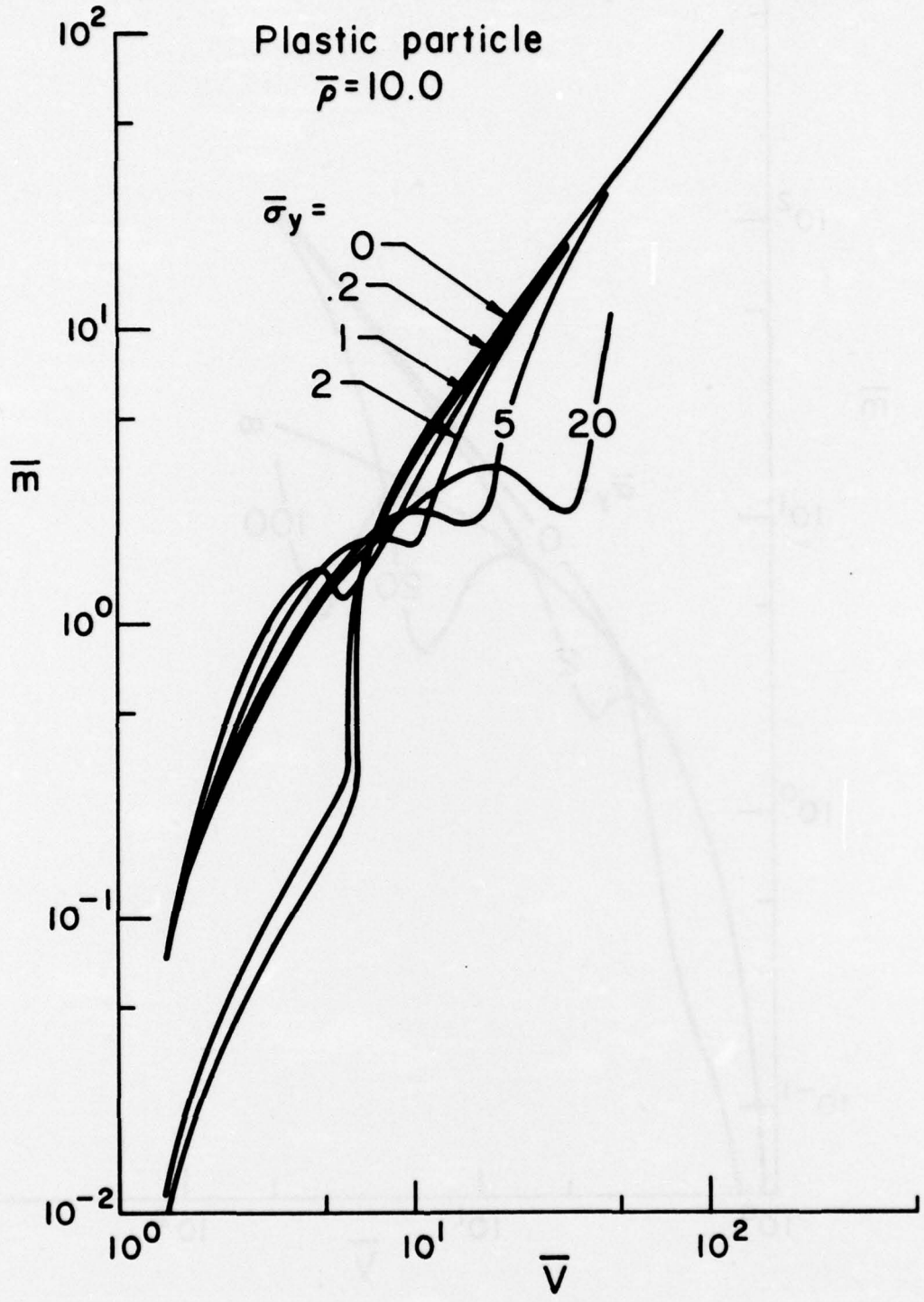

Figure 49. Target mass loss vs. impact velocity

These contrasting results reflect the complex coupling of the particle deformation and penetration and the amount of energy contained in each of the available modes. It was shown earlier that an increase in viscosity results in deeper penetration but a narrower particle and, for some velocities, less lateral kinetic energy. But greater lateral kinetic energy produces greater cavity width. It follows that cavity volume is a very complex function of particle strength and impact velocity.

The complexity of the phenomenon is illustrated well by the predicted mass loss behavior in the intermediate velocity regime. For example, in the interval $6 \leq \bar{V} \leq 15$, Figure 48 shows that it is possible to decrease erosion by increasing the impact velocity when $\bar{\sigma}_y = 20$. In this velocity interval, the width of the particle has increased by 80% (see Fig. 34) but the depth of the cavity has decreased by nearly 25% (see Fig. 40). In addition, the increase in particle kinetic energy associated with higher impact velocities does not produce proportionate increases in lateral kinetic energy of the particle or in work done by the particle on the target. Rather, most of the additional energy is used to heat the particle (Fig. 25). As a result, despite the fact that the width of the particle has increased, the width of the cavity has actually decreased. Figure 50 shows the final cavity shape for the two velocities which bound the regime. The reason for the dip in the erosion curve is evident from this figure.

As the velocity is increased beyond this regime, more of the kinetic energy shows up as relative kinetic energy and, as a result, the cavity becomes much wider. Hence, the erosion curve again increases with further increase of impact velocity.

In summation, perhaps the most important point of these results is the recognition of the uniqueness of each impact condition. Blanket statements such as, "The stronger the particle, the larger the erosion," or "Erosion increases with impact velocity" simply are not always true. Data extrapolation or test planning based on such statements may be faulty and, when the ultimate

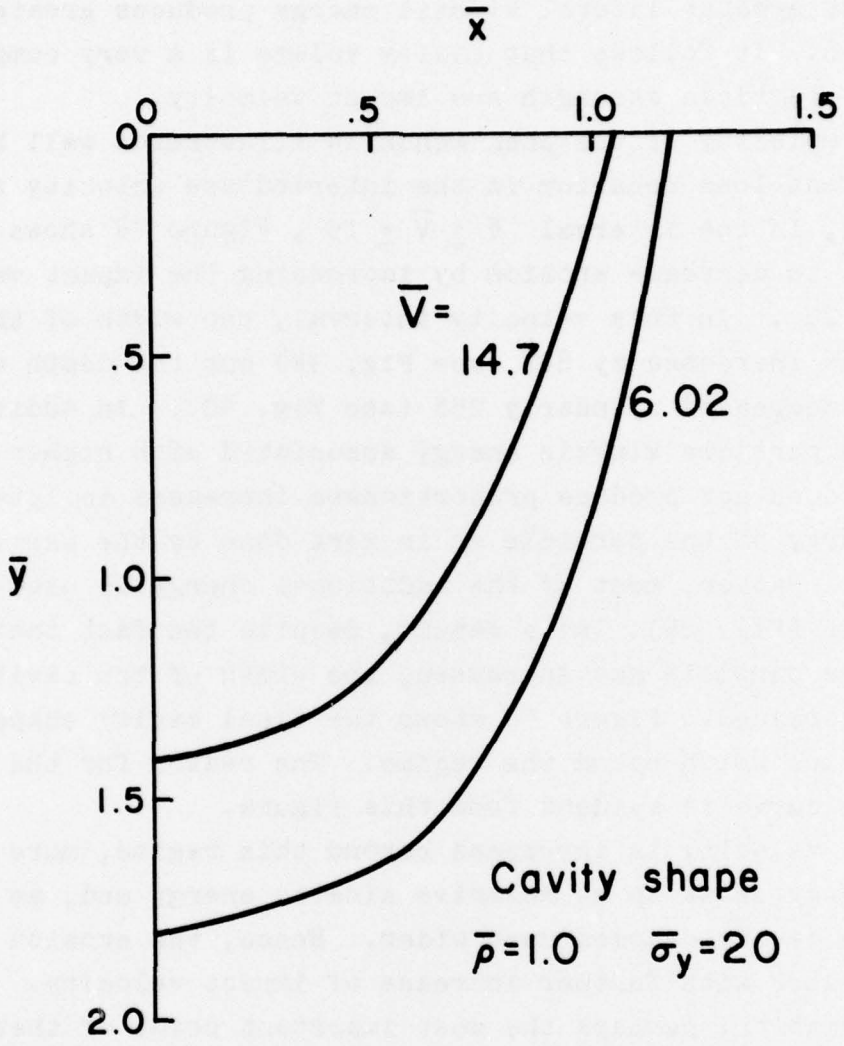

Figure 50. Cavity shape

objective is hardware design, even dangerous. Hopefully, analyses such as this will be able to bound the problem and eliminate the need for all-encompassing but unproven generalizations.

IV. CONCLUSIONS

The first steps in the creation of an integral theory for impact cratering by high-speed particles have been presented and used to perform a parametric investigation of single particle, normal impact. Density ratio, impact velocity, and dissipation parameter (particle viscosity or yield strength) were varied over a wide range of values. The effects of these variations on energy partitioning, particle shape, depth of penetration, and target erosion were determined. The predictions are presented by graphs which may be used for test data interpretation and extrapolation, test planning, hardware design, etc. The graphs should prove useful because one's intuitive abilities are easily overwhelmed by the complexity of the impact process.

REFERENCES

1. Donaldson, Coleman duP. and Thomas B. McDonough, "A Simple Integral Theory for Impact Cratering by High Speed Particles," Defense Nuclear Agency Report DNA 3234F, December 1973.